8-2019

Study of spin and charge dynamics in one-dimensional cuprates using resonant inelastic x-ray scattering

Umesh Kumar Kumar
University of Tennessee, ukumar2@vols.utk.edu

Recommended Citation

Kumar, Umesh Kumar, "Study of spin and charge dynamics in one-dimensional cuprates using resonant inelastic x-ray scattering. " PhD diss., University of Tennessee, 2019.
https://trace.tennessee.edu/utk_graddiss/5961

To the Graduate Council:

I am submitting herewith a dissertation written by Umesh Kumar Kumar entitled "Study of spin and charge dynamics in one-dimensional cuprates using resonant inelastic x-ray scattering." I have examined the final electronic copy of this dissertation for form and content and recommend that it be accepted in partial fulfillment of the requirements for the degree of Doctor of Philosophy, with a major in Physics.

Steven Johnston Prof., Major Professor

We have read this dissertation and recommend its acceptance:

Elbio Dagotto Prof., Norman Mannella Prof., David Mandrus

Accepted for the Council:

Dixie L. Thompson

Vice Provost and Dean of the Graduate School

(Original signatures are on file with official student records.)

Study of spin and charge dynamics in one-dimensional cuprates using resonant inelastic x-ray scattering

A Dissertation Presented for the
Doctor of Philosophy
Degree
The University of Tennessee, Knoxville

Umesh Kumar
August 2019

Dedicated to my late grandmother - Keshrani Rajput.

Acknowledgements

I would first like to express my deepest gratitude to Prof. Steven Johnston for his constant support and guidance over the past five years. He has been a wonderful and supportive supervisor. Additionally, he provided me opportunities to attend several conference and schools, where I could hone my skills and develop networks.

I would also like to thank the members of my committee, Dr. Elbio Dagotto, Dr. Norman Mannella, and Dr. David Mandrus, for their time and helpful suggestions.

A major part of this thesis is motivated by resonant inelastic x-ray scattering (RIXS) experiment conducted at ADDRESS Beamline at Paul Scherrer Institut, Villigen, Switzerland. I would like to express my gratitude to Dr. Justine Schlappa and Dr. Thorsten Schmidt for providing us with the high-quality RIXS data. I would also like to express a special thanks to Dr. Alberto Nocera. His experience, innovative ideas, and inputs played an important role in several projects presented in this dissertation. I want to thank my labmates Dr. Shaozhi Li, Dr. Ken Nakatsukasa, Dr. Yan Wang, and Phillip Dee. Additionally, I would like to thank my colleagues Nitin Kaushal, Dr. Niravkumar Patel, Dr. Guangkun Liu, and Dr. Anamitra Mukherjee from Prof. Dagotto's group. I am grateful to all of them for the stimulating discussions on Physics and Philosophy.

I have met a number of wonderful people who enriched my stay in Knoxville. I would like to thank Manasa Rath for her constant encouragement during graduate school. I would also like to acknowledge my friend Swarnav, for planning many exciting trips. A special shout out my friends Hasitha, Jeethu, Yadu, Rakesh, Gaurav and Vikram for enriching my stay here in the Knoxville. To my friends in cricket and tennis: I am thankful for all the efforts you put in to make all the experiences memorable and enjoyable.

Finally, I would like to express eternal thanks to my family, in particular, my brother, Pravesh, who has always been supportive of me pursuing my ambitions. I hope that I do justice to their tremendous belief in me.

Abstract

One-dimensional (1D) antiferromagnetic chains and ladders realized in strongly correlated materials have attracted significant interest as a platform for studying quasiparticle fractionalization, quantum criticality, and other emergent phenomena. In this thesis, we examine spin and charge dynamics of 1D antiferromagnets revealed by resonant inelastic x-ray scattering (RIXS) using numerical techniques, including exact diagonalization and density matrix renormalization group. One of the major findings of this thesis is the first direct observation of multi-spinon excitations at the oxygen K-edge of Sr_2CuO_3, a prototype 1D cuprate, establishing RIXS as a complementary probe to inelastic neutron scattering (INS) in search of quantum spin liquids. In another study on 1D doped antiferromagnets, the RIXS spectra are shown to be rich, containing distinct two- and four-spinon excitations, dispersive antiholon excitations, and combinations thereof, further establishing that RIXS can serve as a probe of spin-charge separation in these materials. Finally, a systematic theoretical investigation of the Cu L-edge RIXS spectra of undoped and doped cuprate two-leg spin-ladders in both the non-spin-conserving and spin-conserving channels is presented. The spectra host many exotic excitations, in particular, *singlet* two-triplon bound state excitations. Furthermore, direct signatures of charge quasiparticle excitations are revealed by RIXS in the doped ladders. This dissertation helps establish RIXS as an important tool for revealing the signatures of spin and charge fractionalization, and other collective excitations in strongly correlated materials

Table of Contents

List of Tables

List of Figures

Chapter 1

Introduction

Resonant inelastic x-ray scattering (RIXS) is a photon-in and photon-out x-ray spectroscopy that reveals the charge, orbital, lattice, and spin degree of freedom of the materials [1]. In the last decade, RIXS has been established as a prominent probe for studying strongly correlated materials such as cuprates [2, 3, 4, 5], iridates [6, 7, 8, 9], nickelates [10, 11, 12, 13], ruthenates [14, 15, 16, 17], etc. and contributed immensely to the understanding of these materials. Our work in this thesis is largely focused on models motived from cuprates.

Since the discovery of high-temperature superconductivity in the two-dimensional (2D) cuprates in 1986 [18], cuprates have been an exciting topic of research in condensed matter physics. These materials have been studied extensively both experimentally and theoretically, but their behavior is still full of surprises. Apart from 2D geometries exhibiting superconductivity [19], cuprates also exist in one-dimensional (1D) chain and ladder geometries. These 1D geometries exhibit exotic behaviors and are an important playground to study many-body physics. For example, 1D materials allow one to observe the richness of quantum mechanics. Fractionalization of a particle is one such phenomenon. In solid state physics, quasiparticle excitations of electrons are composite particles that can fractionalize into their spin, orbit, and charge degree of freedom namely; spinon, orbiton, and holon, respectively. The study of spin-charge separation dates back to the work of Tomonaga in 1950 [20], followed by Luttinger for 1D systems [21]. After a long wait, the phenomenon was observed using angle-resolved photoemission spectroscopy (ARPES) in the 1D cuprate $\mathrm{SrCuO_2}$ [22, 23]. Similarly, the phenomenon of spin-orbit separation was predicted in 1997 by van den Brink *et al.* [24, 25] and later confirmed by Schlappa *et al.* in 2012 using RIXS at the Cu L_3 edge of $\mathrm{Sr_2CuO_3}$ [5].

Understanding spin and charge dynamics is the key to understanding the superconductivity in cuprates. Local spin fluctuations are considered as one of the possible mechanisms for superconductivity in cuprates [26, 27]. Inelastic neutron scattering (INS) has been extensively used to study these materials and understand their spin dynamics.

With the improvement in instrumentation, RIXS has emerged as a powerful spectroscopic tool to study elementary excitations of quantum materials. The realization that RIXS can observe single spin-flip excitations [3, 29] has made it a probe of magnetic excitations complementary to INS. RIXS has indeed played a very important role in understanding the magnetic excitations in cuprates and at times overcome the limitations of INS. For example, INS studies on doped superconducting cuprates the could not observed any significant signatures of magnetic excitation due to poor statitics in INS and also the lack of large crystal sizes for some cuprates. In contrast, "paramagnons", signature of magnetic excitations shown in Fig. 1.1, were observed using RIXS in the recent past [4, 30, 31, 32, 33, 34]. Recently, an electron-hole asymmetry in the doping dependence of the spin excitations of 2D cuprates was reported, as well as an additional collective charge excitation in the electron-doped case that is absent in the hole-doped case [28]. These observations have been possible because RIXS provide much better statistics in comparison to INS probe and requires smaller sample volumes [1].

While it is now well accepted that RIXS is sensitive to spin and charge dynamics in materials, the interpretation of low energy charge/magnetic excitations in the RIXS spectra of 2D cuprates has been quite controversial. While some model calculations

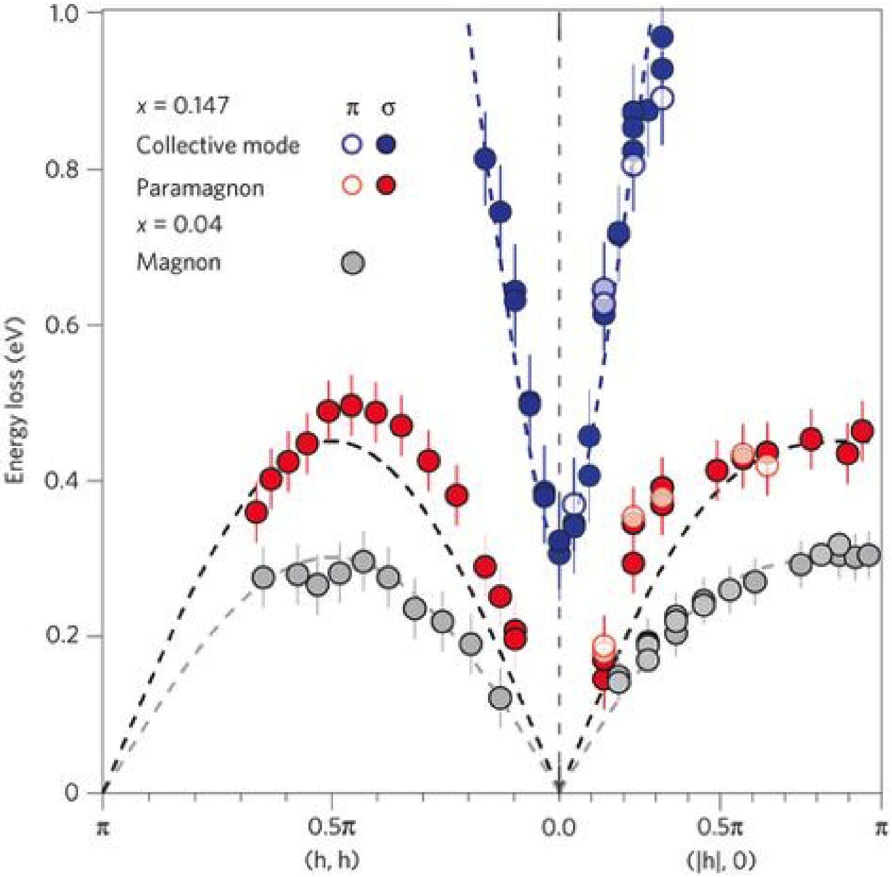

Figure 1.1: Paramagnon and collective mode dispersions in the RIXS spectra of the 2D cuprate $\mathrm{Nd}_{2-x}\mathrm{Ce}_x\mathrm{CuO}_4$ along the $(0,0)-(\pi,0)$ and $(0,0)-(\pi,\pi)$ directions, as indicated in the figure for doping $x = 0.147$. The paramagnon dispersion deviates from simple linear-spin-wave theory (as a guide-to-eye, black dashed curve). The plot also shows the magnon dispersion in an underdoped ($x = 0.04$) compound for comparison. The blue dashed line is a fit to the collective mode dispersion in the form of generic collective charge excitations. The diagram is reproduced from Ref. [28].

indicate that these low energy features arise from collective paramagnon modes induced by strong correlations [32, 33, 35], others attribute them to incoherent, non-generic particle-hole excitations that reflect the band structure of specific cuprate compounds [36, 37]. Other studies have tried resolving the excitations into spin and charge components [38, 39]. Most of the progress in the interpretation of RIXS experiments have been made with two assumptions: i) the quasiparticle nature of magnetic and charge excitations and ii) that the RIXS cross-section can be modeled in terms of simpler correlation function such as spin or charge dynamical structure factor or spin-exchange dynamical factor, which is at times compared against INS data. But a number of studies in recent past have cast aspersions on the quasiparticle nature of the excitations observed even in INS spectra. For example, the existence of deconfined fractional spin-1/2 quasiparticles in the 2D cuprates was reported [40]. Also, 1D cuprates are well known to host fractionalized excitation, but recently even higher modes in addition to the usual two-spinon excitation have been observed in INS studies [41].

Exact numerical methods such as exact diagonalization (ED) and density matrix renormalization group (DMRG) can overcome the problem of using a simplified quasiparticle description by directly employing many-body wavefunctions. However, ED is limited in cluster sizes and can do fairly long systems only in 1D. Also, DMRG can access much longer systems in 1D compared to ED but is again currently well suited for mostly quasi-1D systems only. This thesis, therefore, targets the problem of understanding RIXS spectra of 1D systems, which allows treating the full many-body physics and Kramers-Heisenberg formalism using numerical methods.

Cuprate materials allow for crystal structures simpler than 2D layers, namely, (a) 1D chain and (b) two-leg ladders. These geometries still host intriguing quantum mechanical many-body properties and studying them has proved to be a fruitful path for progress in the field [2, 5, 23, 42]. These simpler geometries are an ideal playground for theorists to perform model Hamiltonian calculations and understand the spin and charge dynamics revealed by RIXS spectroscopy. We discuss the crystal structures of 1D chain and two-leg ladder cuprates in the next section.

1.1 Overview of one-dimensional cuprates

Sr_2CuO_3 realizes a quasi-1D system and serves as an ideal playground to study 1D physics [5, 43, 44, 45]. It hosts corner-shared CuO_4 plaquettes in a chain, as shown in Fig. 1.2. The CuO_4 plaquettes have a Cu (d^9) configuration, which hosts an effective single spin in each plaquette with antiferromagnetic (AFM) correlation along the chain direction. Sr_2CuO_3 has passed some of the stringent tests confirming the 1D nature of the material. For example, an INS study on this compound has confirmed the presence of fractionalized two-spinon excitation, the signature of 1D antiferromagnets [46] (also in another related cuprate, $SrCuO_2$ [47]). Furthermore, ARPES studies on Sr_2CuO_3 reported the observation of spin-charge separation [48, 49]. Additionally, a more recent RIXS study at the Cu L_3-edge of Sr_2CuO_3 reported the observation of spin-orbit separation [5].

RIXS is element and edge sensitive; the x-ray resonant with the edges in Cu and O atoms can probe the dynamics of the chain, albeit through a different mechanism. Fig. 1.3(a) and Fig. 1.3(b) shows the RIXS spectra for Sr_2CuO_3 at oxygen K-edge and Cu L_3-edge, respectively. Since the oxygen K-edge ($1s \to 2p$ resonance) is resonant at 528.6 eV and Cu L_3-edge ($2p_{3/2} \to 3d$ resonance) at 931 eV, these incident energies allow for accessing half and all of the first Brillouin zone (BZ), respectively.

The spectra at the oxygen K-edge, shown in Fig. 1.3(a), is primarily sensitive to the charge excitations on the oxygen sites of the CuO_4 plaquettes. The brightest features are between $2-6$ eV and the excitations can be broadly understood as Zhang Rice Singlet (ZRS) and charge transfer (CT) excitations [50, 51, 52]. Both ZRS and other CT excitations are driven by local electronic interactions. A detailed analysis of these charge excitations is missing in the literature but is also well beyond the scope of this thesis.

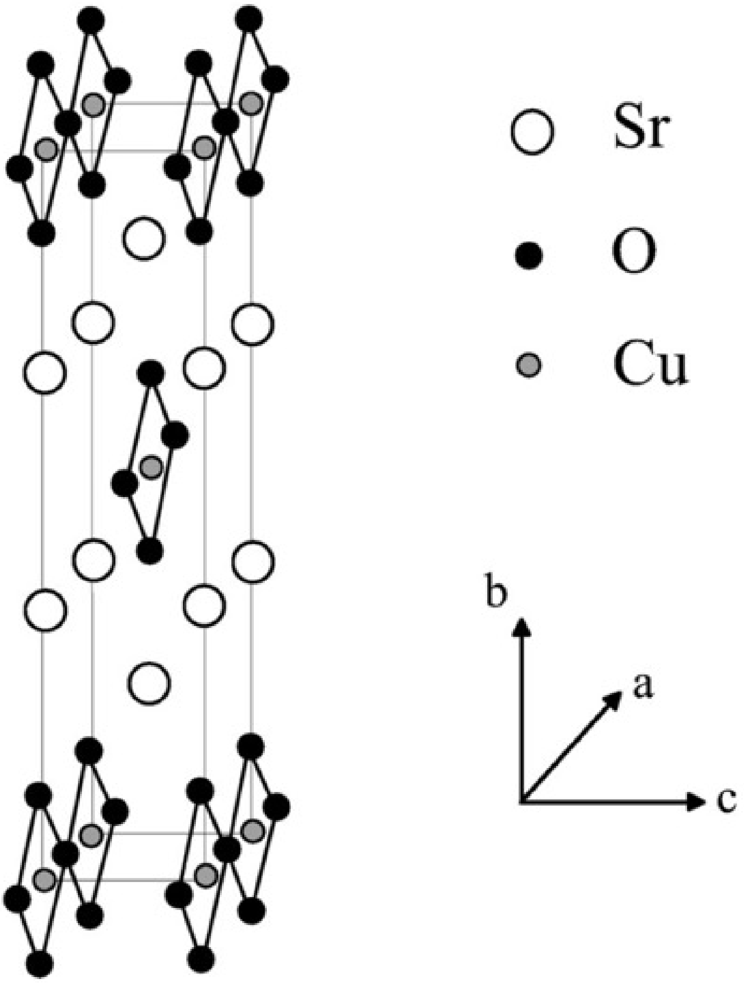

Figure 1.2: Crystal structure of Sr_2CuO_3, reproduced from Ref. [43]. The corner-shared single and double CuO_4 plaquettes run along the a-axis and form 1D chains.

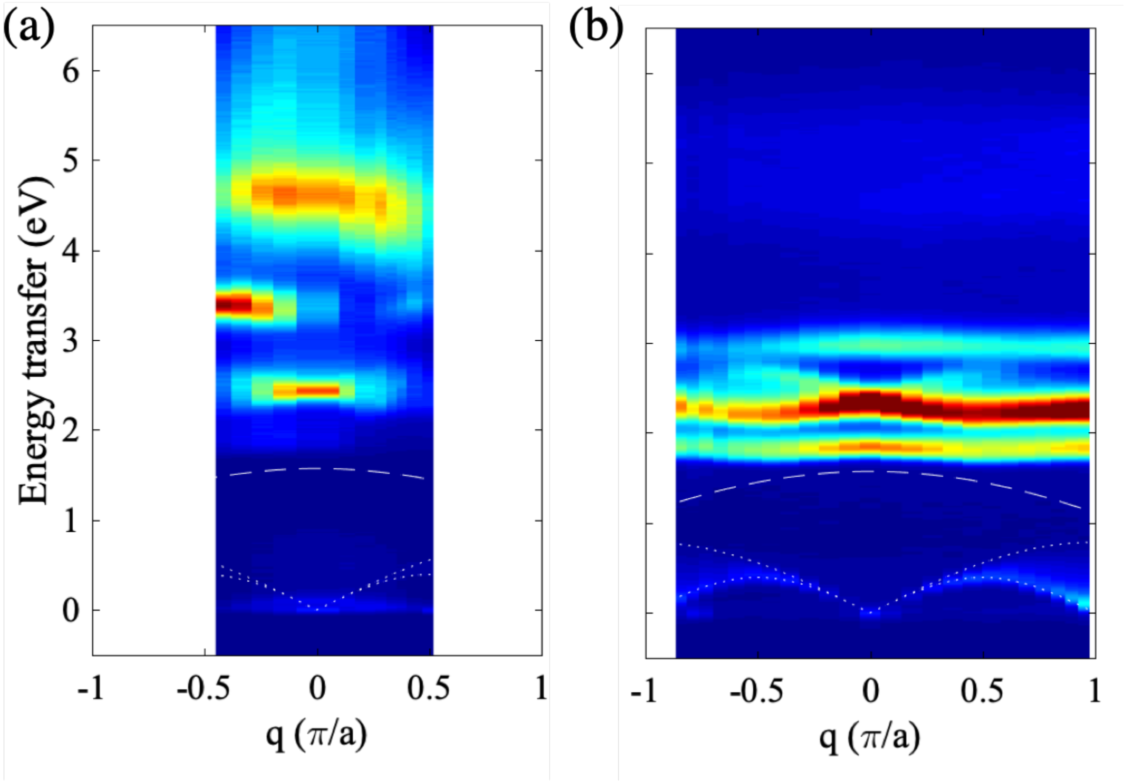

Figure 1.3: RIXS spectra at different edges of Sr_2CuO_3; (a) Oxygen (bridging) K-edge and (b) Cu L_3-edge . The O K-edge ($1s \rightarrow 2p$ resonance) can access half of the Brillouin-zone (BZ), whereas Cu L_3-edge ($2p_{3/2} \rightarrow 3d$ resonance) can access the entire first BZ. The white dotted/dashed lines are overlays for the magnetic excitation in the 1D antiferromagnets. The data in (a) was provided by our collaborators J. Schlappa and T. Schmitt, whereas (b) is reproduced from Ref. [5].

On the other hand, the RIXS at Cu L_3-edge shown in Fig. 1.3(b) is sensitive to the excitations on Cu and allow one to observed the separation of spin and orbital degrees of freedom. The exctations at around $1.5 - 3.0$ eV show a well defined dispersion with a bandwidth of around 0.2 eV. Usually understood as *dd*-excitations, Schlappa and coauthors showed that these dispersing excitations could be understood as a distinct quasi-particle, namely, orbitons, propagating through the lattice [5].

In both panels (a) and (b) of Fig. 1.3, the excitations below 1.5 eV are weak compared to the charge and orbital excitations, and are understood as magnetic excitations. Mechanism for the magnetic excitations at the oxygen K-edge and Cu L_3 are very different. The details of these magnetic excitations will be discussed in chapter 3.

Sr_2CuO_3 can be doped with Zn, Ni, or Co [49, 53, 54], and so this material can help one realize a doped 1D system. Since RIXS is also sensitive to charge, it provides an opportunity to observe charge dynamics in the 1D doped system. A theoretical study to reveal charge along with the spin dynamics at the oxygen K-edge of doped Sr_2CuO_3 is presented in chapter 4.

1.2 Ladder cuprates

$(Sr,Ca)_{14}Cu_{24}O_{41}$, shown in Fig. 1.4, is a prototype ladder cuprate that consists of two sets of plaquettes, chain unit CuO_2 and ladder unit Cu_2O_3 running along the c-axis direction. The Cu sites have $3d^9$ configurations, which host a spin at each plaquette. The CuO_2 plaquettes form ferromagnetic chain whereas the Cu_2O_3 plaquettes form antiferromagnet spin-ladder. $(Sr,Ca)_{14}Cu_{24}O_{41}$, also known as a 'telephone number compound' has passed stringent tests of its classification as a quantum spin ladder. For example, a spin gap, a signature of the spin ladder was reported in the INS study of $Sr_{14}Cu_{24}O_{41}$ in 1998 [42]. Later, in 2007, triplet two-triplon excitations were reported in the INS study of $La_4Sr_{10}Cu_{24}O_{41}$ [56] further confirming the predictions

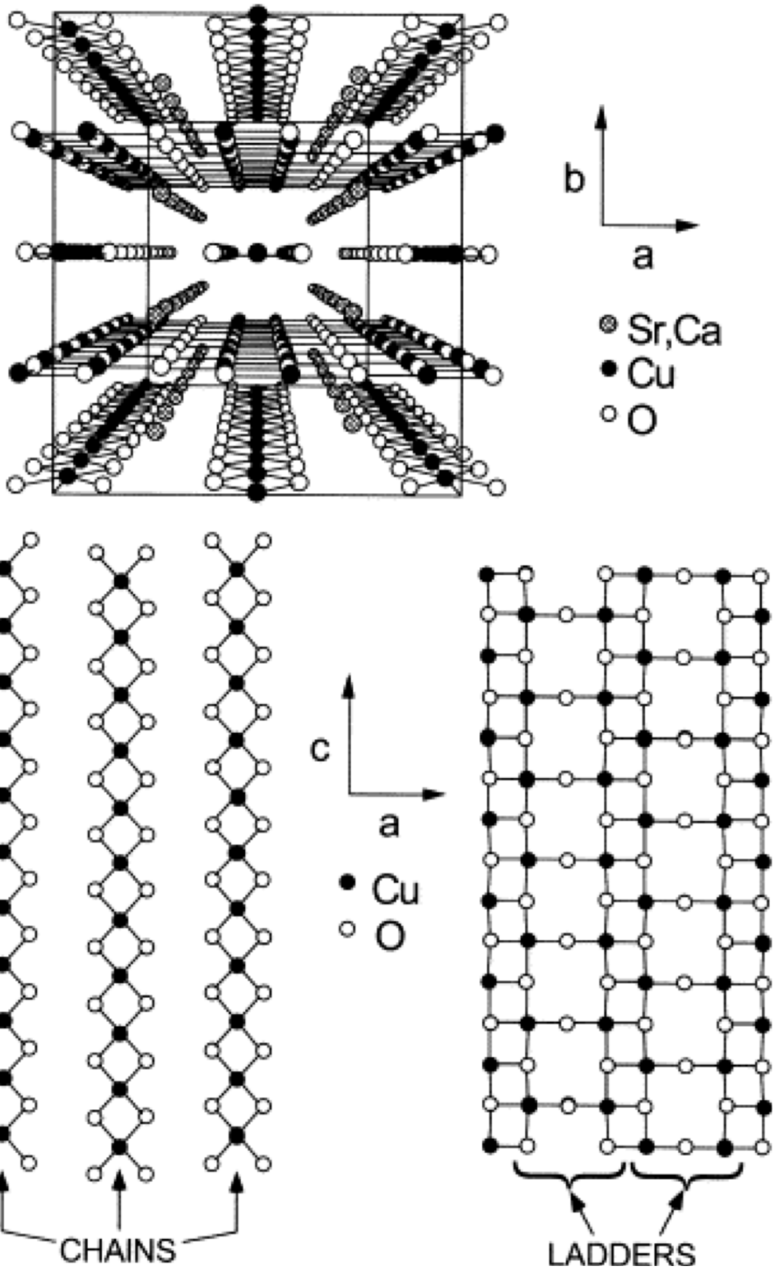

Figure 1.4: Crystal structure of $(Sr,Ca)_{14}Cu_{24}O_{41}$ reproduced from Ref. [55]. $(Sr,Ca)_{14}Cu_{24}O_{41}$ consists of chain unit CuO_2 and the ladder unit Cu_2O_3 running along the c-axis direction. The CuO_2 plaquettes form ferromagnetic chains whereas the Cu_2O_3 plaquettes form antiferromagnet spin-ladders.

of ladder physics in these cuprates. Another RIXS study on $Sr_{14}Cu_{24}O_{41}$ reported the observation of two-triplon collective excitations [2].

Cuprate ladders are important systems for several reasons: they are quasi-one dimensional, which is an ideal setting for the application of accurate numerical and analytical techniques; more importantly, cuprate ladders share many similarities with their 2D counterparts including unconventional superconductivity when doped with hole carriers [2, 5, 41, 42, 57, 58, 59, 60, 61, 62, 63, 64, 65, 66, 67, 68, 69, 70, 71]. The discovery of superconductivity in the ladder compound $Sr_{0.4}Ca_{13.6}Cu_{24}O_{41.84}$ [19], which had been theoretically predicted [72], created new opportunities to study the relationships between lattice, orbital, charge, and magnetic degrees of freedom and unconventional superconductivity in copper-oxide materials. Apart from studying high critical temperature (high-T_c) superconductivity, strongly correlated spin ladders are another excellent platform for studying quantum many-body phenomena, such as spinon confinement [70].

From a RIXS perspective, it is very surprising that only a few theoretical and experimental RIXS studies have been conducted on cuprate ladders in contrast to a large number of RIXS studies on two-dimensional cuprates. RIXS experiments on $Sr_{14}Cu_{24}O_{41}$ and $CaCu_2O_3$ have been reported, but with limited analysis. The studies on $CaCu_2O_3$ did not report any analysis of ladder physics [73, 74], but the studies on $Sr_{14}Cu_{24}O_{41}$ reported the observation of magnetic excitations in spin ladders [2]. But the versatility of RIXS experiments can reveal further spin and charge dynamics in these compounds. In chapter 5, we show how RIXS can further reveal rich spin and charge dynamics feature in the spin ladders.

1.3 Scope and Organization

The goal of this thesis is to examine the spin and charge dynamics in quasi-1D strongly correlated materials using numerical methods, and to understand and make predictions for the RIXS experiments studying these dynamics. The overall organization is as follows:

Chapter 1 (this chapter) motivates the need to study one-dimensional cuprates. The crystal structures of the relevant cuprates is discussed. Chapter 2 presents the microscopic details of RIXS theory. Numerical methods employed for simulating the RIXS cross-section are also discussed. Chapter 3 presents the recent observation of four-spinon excitations in a 1D Heisenberg antiferromagnet material using resonant inelastic x-ray scattering study. Chapter 4 presents the spin and charge dynamics of doped 1D antiferromagnets. Through numerical calculations, it is shown that RIXS can access spin-charge separation in doped 1D antiferromagnets. Chapter 5 presents a systematic study of spin and charge dynamics in spin-ladder antiferromagnets. Resonant inelastic x-ray scattering (RIXS) spectra allow us to explore these directly in the materials exhibiting spin-ladder antiferromagnetic structures. Chapter 6 presents the conclusions of the thesis and a discussion on the possible extensions of this work in the future.

Chapter 2

Methods

In this chapter, we explore the microscopic details of the theory of RIXS. The numerical methods used in this thesis for simulating the RIXS cross-section are also discussed.

RIXS is a photon-in and photon-out spectroscopy. RIXS uses X-ray photons that have large momentum that can partly be transferred to the crystal, and hence, allow one to observe the dispersion of quasiparticle excitations in the material. This is in contrast to another photon based spectroscopy, Raman scattering, which uses photon at lower energies such as visible/infrared and does not have momentum transfer to the crystal.

In the RIXS process, an incoming photon with momentum $\hbar\mathbf{k}_{\text{in}}$ and energy $\hbar\omega_{\text{in}}$ excites an electron from a core-level of an atom into the unoccupied valence band, as shown in 2.1(a). The system then relaxes in the presence of core-hole, and excitations in the valence band are created. Finally, when an electron from the valence band recombines with core-hole, a photon with momentum $\hbar\mathbf{k}_{\text{out}}$ and energy $\hbar\omega_{\text{out}}$ is emitted from the system with a transfer of finite energy and momentum to the crystal, as shown in 2.1(b). In this process, an energy $\hbar\Omega = \hbar\omega_{\text{in}} - \hbar\omega_{\text{out}}$ and momentum $\hbar\mathbf{q} = \hbar\mathbf{k}_{\text{in}} - \hbar\mathbf{k}_{\text{out}}$ is transferred to the crystal. As the name suggests, RIXS uses x-rays to excite the electron and can be made to resonate with any of the

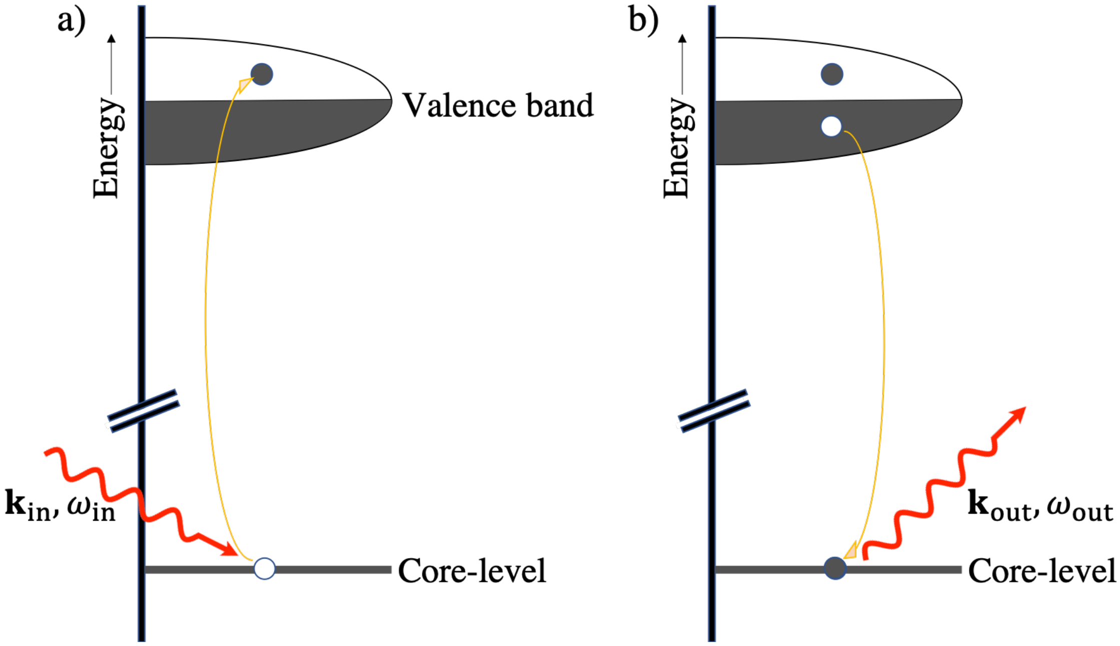

Figure 2.1: A sketch of the excitation pathway in the RIXS. a) A photon with momentum $\hbar\mathbf{k}_{\text{in}}$ and energy $\hbar\omega_{\text{in}}$ excites an electron from a core-level to an empty state. b) A photon with momentum $\hbar\mathbf{k}_{\text{out}}$ and energy $\hbar\omega_{\text{out}}$ is emitted out. The empty core level is filled by an electron from the occupied band leaving behind an excitation in the valence band.

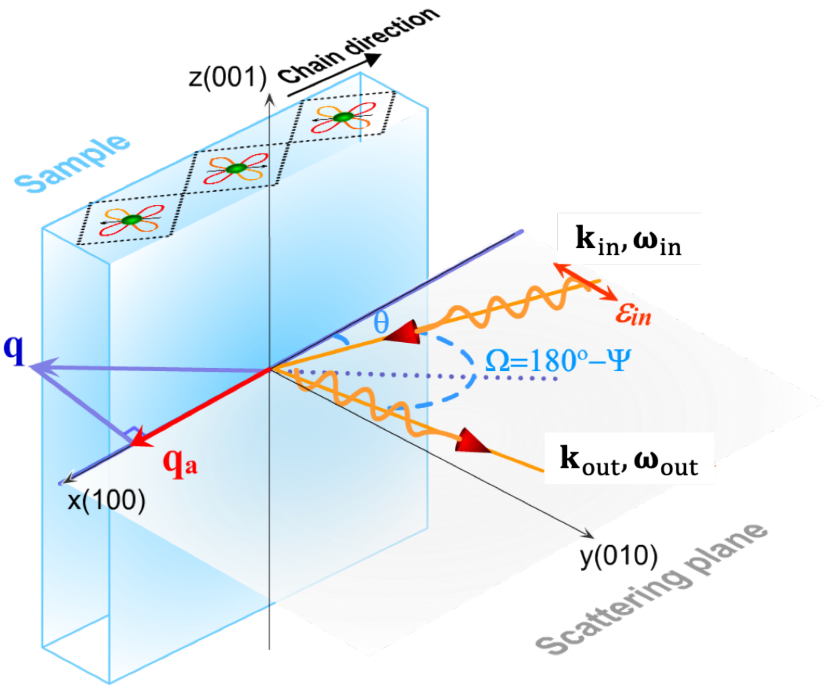

Figure 2.2: A schematic of the experimental geometry. In this example, CuO_4 plaquettes in the 1D chain (shown here) lie in the scattering plane. The incidence angle, θ, is varied during the experiment to change the projection of the momentum transfer along the chain direction, whereas the scattering angle ψ is kept constant. A photon with momentum $\hbar\mathbf{k}_{\text{in}}$ and energy $\hbar\omega_{\text{in}}$ enters with the crystal and another photon with momentum $\hbar\mathbf{k}_{\text{out}}$ and energy $\hbar\omega_{\text{out}}$ is emitted out. This schematic diagram is reproduced from Ref. [57].

core-levels like K, L, M absorption edge of metals or ligand oxygens in the transition metals oxides.

In RIXS experiments, the incoming and outgoing photons form a scattering plane. In this plane, the incident photon with momentum $\hbar\mathbf{k}_{\text{in}}$ and energy $\hbar\omega_{\text{in}}$ enters with the crystal at an angle θ and another photon with momentum $\hbar\mathbf{k}_{\text{out}}$ and energy $\hbar\omega_{\text{out}}$ is emitted out. The angle between the incoming and the outgoing light, the scattering angle, ψ is usually kept fixed in the RIXS experiments. As shown in Fig. 2.2, the momentum transferred to the crystal can be controlled by changing the incident angle θ of the photon with respect to the orientation of the crystal.

Since the RIXS spectroscopy involves the light-matter interaction, we will discuss it to understand the theory of the RIXS process.

2.1 Light-Matter Interaction and the Kramers-Heisenberg Formalism

The physics of light-matter interaction is described by the theory of quantum electrodynamics (QED); however, derivation of the RIXS cross-section in terms of QED would be a cumbersome task and is unnecessary. In our case, the electrons are non-relativistic. Also, the photons have relatively low energy compared to the mass of an electron, and the total energy of the system is far below the electron-positron pair creation energy ($\hbar\omega_{in} \ll 1.022$ MeV), and thus these high-energy process can be neglected. This allows for the charge conservation of electrons in our system and hence, we can study RIXS using an effective low energy approximation of QED.

We consider a system consisting of a photon interacting with an electron in the presence of its atomic potential. The X-ray scatters the electron resulting in a transition in the system. The transition rate w is given by Fermi's Golden rule, which to second order is

$$w = \frac{2\pi}{\hbar} \sum_{\mathrm{f}} \left| \langle \mathrm{f}|H_1|\mathrm{g}\rangle + \sum_{n} \frac{\langle \mathrm{f}|H_1|n\rangle\langle n|H_1|\mathrm{g}\rangle}{E_{\mathrm{g}} - E_n} \right|^2 \delta(E_{\mathrm{f}} - E_{\mathrm{g}}). \tag{2.1}$$

Here, the states, $|\mathrm{g}\rangle$, $|\mathrm{f}\rangle$, and $|n\rangle$ are the initial, final, and intermediate states for the system with energies E_{g}, E_{f}, and E_n, respectively. Also, $E_{\mathrm{g}} = E_g + \hbar\omega_{\mathrm{in}}$, $E_{\mathrm{f}} = E_f + \hbar\omega_{\mathrm{out}}$ and the terms E_g and E_f are initial and final states of the material, respectively. H_1 is the perturbation in the system due to the electron-photon interaction. In general, the first order term dominates in the transition rate, but if the incident photon is in resonance with a specific edge in the material ($E_{\mathrm{g}} \approx E_n$), then the second order term dominates and the first order term can be neglected [75].

Let us discuss the origin of the perturbation term H_1 responsible for the transition in the system. The vector potential $\mathbf{A}$ for a photon with wave vector $\mathbf{k}$ and the polarization along $\boldsymbol{\varepsilon}$ is given by,

$$\mathbf{A} = A_0[\boldsymbol{\varepsilon} a_{k\epsilon} e^{i\mathbf{k}\cdot\mathbf{r}} + \boldsymbol{\varepsilon}^* a_{k\epsilon}^{\dagger} e^{-i\mathbf{k}\cdot\mathbf{r}}]. \tag{2.2}$$

Here, $a_{k\epsilon}^{\dagger}$ ($a_{k\epsilon}$) creates (annihilates) a photon. The interaction between a photon with vector potential $\mathbf{A}$ and an electron in an atomic orbital at site-i, momentum operator $\mathbf{p}_i$, mass m_e, and in the presence of central potential $\phi(x_i)$ as discussed in Sakurai [76] is considered. The Hamiltonian for a fixed gauge $\nabla \cdot \mathbf{A} = 0$ is given by

$$\begin{aligned} H &= \frac{(\mathbf{p}_i - e\mathbf{A}(r_i)/c)^2}{2m_e} + e\phi(x) \\ &= \frac{p_i^2}{2m_e} + e\phi(x) + \frac{e^2 A^2(r_i)}{2m_e c^2} - \frac{e}{m_e c}\mathbf{A}(r_i) \cdot \mathbf{p}_i, \\ &= H_0 + H_1 \end{aligned} \tag{2.3}$$

where,

$$H_0 = \frac{p_i^2}{2m_e} + e\phi(x), \qquad H_1 = -\frac{e}{m_e c}\mathbf{A}(r_i) \cdot \mathbf{p}_i. \tag{2.4}$$

In the above equation, we have partitioned the total Hamiltonian H into its contribution from the material H_0 and the electron-photon coupling H_1, and the Thomson scattering term proportional to $A^2(r_i)$ has been neglected. $A^2(r_i)$ dominates only when the incident energy $\hbar\omega_{\text{in}}$ of the photon is much larger than resonance, *i.e.* non-resonant inelastic scattering. It also contributes to Bragg peaks but is weak in RIXS and hence omitted.

The perturbation term is responsible for the transition in the system. Also, it is important to note that the term corresponding to $a_{k\varepsilon}$ in $\mathbf{A}$ annihilates a photon and survives for the case of absorption. Motivated by it, we define a transition operator for absorption given by

$$\mathcal{D} = \frac{1}{i m_e \omega_k} \sum_{i=1}^{N} e^{i\mathbf{k}\cdot\mathbf{r}_i} \boldsymbol{\varepsilon} \cdot \mathbf{p}_i. \tag{2.5}$$

Here, $\hbar\omega_k$ is the energy of the absorbed photon. In the **dipole limit**, it is assumed that the wavelength of radiation is very long compared to atomic size ($\lambda_{\text{photon}} >> R_{\text{atom}}$). Hence, $e^{i\mathbf{k}\cdot\mathbf{r}_i}$ is constant on the length scale of atom such that $e^{i\mathbf{k}\cdot\mathbf{r}_i} = e^{i\mathbf{k}\cdot(\mathbf{R}_i+\mathbf{r})} \approx e^{i\mathbf{k}\cdot\mathbf{R}_i}$. Here, $\mathbf{R}_i$ and $\mathbf{r}_i$ are the position of nucleus and electron of i^{th} atom in the lattice, and $\mathbf{r}$ is the position vector connecting $\mathbf{R}_i$ and $\mathbf{r}_i$. The dipole limit is valid because for the photon to excite an electron from the core-level of an atom, its energy must be of the order of atomic energy level spacing, $E_{\text{photon}} = \frac{\hbar c}{\lambda_{\text{photon}}} \simeq \frac{Ze^2}{R_{\text{atom}}}$. Thus $\frac{R_{\text{atom}}}{\lambda_{\text{photon}}} \simeq \frac{Ze^2}{\hbar c} = \frac{Z}{137} \ll 1$ for lighter atoms. The magnitude of $\mathbf{r}$ is on the order of the atomic radius, so the leading term is usually sufficient as $\mathbf{k}\cdot\mathbf{r} \ll 1$. Thus, one can approximate the dipole operator as

$$\mathcal{D} = \frac{1}{im_e\omega_k}\sum_{i=1}^{N} e^{i\mathbf{k}\cdot\mathbf{r}_i}\boldsymbol{\varepsilon}\cdot\mathbf{p}_i = \frac{1}{im_e\omega_k}\sum_{i=1}^{N} e^{i\mathbf{k}\cdot\mathbf{R}_i}\boldsymbol{\varepsilon}\cdot\mathbf{p}_i. \tag{2.6}$$

It helps to express the transition operator in real space as one often writes the basis in real space for crystals.

$$\begin{aligned}\langle n|\mathcal{D}|g\rangle =& \frac{1}{im_e\omega_k}\boldsymbol{\varepsilon}\cdot\sum_{i=1}^{N} e^{i\mathbf{k}\cdot\mathbf{R}_i}\langle n|\mathbf{p}_i|g\rangle = \frac{1}{im_e\omega_k}\boldsymbol{\varepsilon}\cdot\sum_{i=1}^{N} e^{i\mathbf{k}\cdot\mathbf{R}_i}\frac{m_e}{i\hbar}\langle n|[\mathbf{r}_i, H_0]|g\rangle \\ =& \frac{1}{\hbar\omega_k}(E_n - E_g)\boldsymbol{\varepsilon}\cdot\sum_{i=1}^{N} e^{i\mathbf{k}\cdot\mathbf{R}_i}\langle n|\mathbf{r}_i|g\rangle \approx \boldsymbol{\varepsilon}\cdot\sum_{i=1}^{N} e^{i\mathbf{k}\cdot\mathbf{R}_i}\langle n|\mathbf{r}_i|g\rangle.\end{aligned} \tag{2.7}$$

In the above equations, we have used the relation $[\mathbf{r}_i, H_0] = \frac{i\hbar\mathbf{p}_i}{m_e}$ and the fact that energy of the photon is in resonance with excitations in the material $\hbar\omega_k \approx E_n - E_g$. The reader is reminded that $\mathbf{r}_i$ is position of the electron at i^{th}-site of the crystal. For simplicity, we transform the position operator $\mathbf{r}_i$ to its second quantized form, which is given by,

$$\langle n|\mathbf{r}_i|g\rangle = \sum_{\alpha,\beta}\langle\phi_\beta(\mathbf{r})|\mathbf{r}|\phi_\alpha(\mathbf{r})\rangle c^\dagger_{i,\beta,\sigma}c_{i,\alpha,\sigma} \tag{2.8}$$

Here, $c^\dagger_{i,\beta,\sigma}(c_{i,\alpha,\sigma})$ are creation (annihilation) operators that cause a transition between the $\phi_\alpha(\mathbf{r})$ and $\phi_\beta(\mathbf{r})$ orbitals in the $\sigma-$spin channel. Also, the index on $\mathbf{r}$ has been dropped as the excitation is an on-site process as the core-level orbitals are localized. The transition operator in the second quantized form can, therefore, be written as

$$\mathcal{D} = \sum_{\alpha,\beta,\sigma} \langle \phi_\beta(\mathbf{r}) | \boldsymbol{\varepsilon} \cdot \mathbf{r} | \phi_\alpha(\mathbf{r}) \rangle \sum_{i=1}^{N} e^{i\mathbf{k}\cdot\mathbf{R}_i} c^\dagger_{i,\beta,\sigma} c_{i,\alpha,\sigma}. \tag{2.9}$$

Similarly, the transition operator for the emission of photon with polarization $\boldsymbol{\varepsilon}'$ can be written as

$$\mathcal{D}'^\dagger = \sum_{\alpha',\beta',\sigma'} \langle \phi_{\alpha'}(\mathbf{r}) | \boldsymbol{\varepsilon}' \cdot \mathbf{r} | \phi_{\beta'}(\mathbf{r}) \rangle \sum_{i=1}^{N} e^{-i\mathbf{k}'\cdot\mathbf{R}_i} c^\dagger_{i,\alpha',\sigma'} c_{i,\beta',\sigma'}. \tag{2.10}$$

Combining these results gives the Kramers-Heisenberg for the RIXS intensity

$$\mathcal{I}_{RIXS} = |\mathcal{F}_{fg}|^2 \delta(E_f + \hbar\omega_{\text{out}} - E_g - \hbar\omega_{\text{in}}), \tag{2.11}$$

where the scattering amplitude $\mathcal{F}_{fg}$ for RIXS is given by

$$\begin{aligned} \mathcal{F}_{fg}(\mathbf{k}_{\text{in}}, \mathbf{k}_{\text{out}}, \omega_{\text{in}}, \omega_{\text{out}}, \boldsymbol{\varepsilon}, \boldsymbol{\varepsilon}') &= \sum_n \frac{\langle f | \mathcal{D}'^\dagger | n \rangle \langle n | \mathcal{D} | g \rangle}{E_g + \hbar\omega_{\text{in}} - E_n + i\Gamma_n} \\ &= T_{\alpha',\beta',\beta,\alpha}(\boldsymbol{\varepsilon}', \boldsymbol{\varepsilon}) \sum_{n,i} e^{i\mathbf{q}\cdot\mathbf{R}_i} \frac{\langle f | c^\dagger_{i,\alpha',\sigma'} c_{i,\beta',\sigma'} | n \rangle \langle n | c^\dagger_{i,\beta,\sigma} c_{i,\alpha,\sigma} | g \rangle}{E_g + \hbar\omega_{\text{in}} - E_n + i\Gamma_n}. \end{aligned} \tag{2.12}$$

The term Γ_n is the inverse core-hole lifetime of intermediate state and $\hbar\mathbf{q} = \hbar\mathbf{k}_{\text{in}} - \hbar\mathbf{k}_{\text{out}}$ is the momentum transfer to the crystal.

In the above expression, the polarization factor has been separated from the rest of the scattering and is given by

$$T_{\alpha',\beta',\beta,\alpha}(\boldsymbol{\varepsilon}', \boldsymbol{\varepsilon}) = \langle \phi_{\beta'}(\mathbf{r}) | \boldsymbol{\varepsilon}'^* \cdot \mathbf{r} | \phi_{\alpha'}(\mathbf{r}) \rangle \langle \phi_\beta(\mathbf{r}) | \boldsymbol{\varepsilon} \cdot \mathbf{r} | \phi_\alpha(\mathbf{r}) \rangle. \tag{2.13}$$

$T_{\alpha',\beta',\beta,\alpha}(\boldsymbol{\varepsilon}', \boldsymbol{\varepsilon})$ is called the "atomic scattering factor" and does not contain any correlation effects of the material. The information from polarization is of central importance to RIXS calculations. Using appropriate polarization one can choose the excitations created in the system [77, 78, 79, 80]. Polarization in the system is accounted using atomic scattering operator, $T_{\alpha',\beta',\beta,\alpha}(\boldsymbol{\varepsilon}',\boldsymbol{\varepsilon})$, which looks simple. In the presence of spin-orbit coupling, it has to be treated carefully. In general, the core-hole orbitals in RIXS with finite orbital angular momentum ($l > 0$) have significant spin-orbit coupling. This is due to the large unscreened potential they experience in core-level compared to the screened potential in the valence band. Thus one has to shift from the $|l, l_z, s, s_z\rangle$-basis to the total angular momentum $|J, J_z\rangle$-basis as the spin and orbital angular momentum are no longer good quantum numbers. Smith *et al.* [81] evaluated the the dipole matrix elements for optical transitions using circularly polarized light for L_2 and L_3 edges. de Groot *et al.* [82] used these polarization dependencies to study local spin flip ecitations in Cu^{+2} and Ni^{+2} using RIXS. Since in recent times, RIXS experiments are largely carried out using lineraly polarized light, we present the dipole matrix elements for the L_2 ($2p_{3/2} \rightarrow 3d$), L_3 ($3p_{1/2} \rightarrow 3d$), M_2 ($3p_{1/2} \rightarrow 3d$) and M_3 ($3p_{3/2} \rightarrow 3d$) edges transitions for a linearly polarized light in the Appendix A.

Oxygen K-edge:— In the case of the oxygen K-edge of $\mathrm{Sr_2CuO_3}$ relevant for Chapter 3 and 4, the transition is between $1s \rightarrow 2p$ orbitals. Since one is usually interested in the low energy spin and charge dynamics in 1D cuprates, only the p_x-orbital of the bridging oxygen of $\mathrm{Sr_2CuO_3}$ is relvant. In the atomic scattering factor

$$T_{2p_x,1s,2p_x,1s}(\boldsymbol{\varepsilon}',\boldsymbol{\varepsilon}) = \langle\phi_{1s}(\mathbf{r})|\boldsymbol{\varepsilon}'^{*}\cdot\mathbf{r}|\phi_{2p_x}(\mathbf{r})\rangle\langle\phi_{2p_x}(\mathbf{r})|\boldsymbol{\varepsilon}\cdot\mathbf{r}|\phi_{1s}(\mathbf{r})\rangle, \tag{2.14}$$

one can see that only x-polarized light can cause excitation and dexcitations. Therefore, the atomic scattering factor $T_{2p_x,1s,2p_x,1s}(\boldsymbol{\varepsilon}',\boldsymbol{\varepsilon}) \propto \sin(\theta)\sin(\psi-\theta)$. Here, θ and ψ are the incidence and scattering angles shown in Fig. 2.2.

2.2 Numerical methods

In general, RIXS experiments are used to study materials that display strong local Coulomb interactions. Therefore, these materials are modeled using the Hubbard model Hamiltonian, as the picture of independent particles is no longer accurate. While evaluating the RIXS cross-section, one writes two sets of Hamiltonian: a) H_0 for the material, and b) H_{ch} for the material with the absorbed photon. The RIXS response is usually simulated using Kramers-Heisenberg formalism which is given by

$$\mathcal{I}_{RIXS} = |\mathcal{F}_{fg}|^2 \delta(E_f + \hbar\omega_{\text{out}} - E_g - \hbar\omega_{\text{in}}). \tag{2.15}$$

where the scattering amplitude $\mathcal{F}_{fg}$ is given by

$$\mathcal{F}_{fg} = \langle f| \sum_i e^{i\mathbf{q}\cdot\mathbf{R}_i} D'^{\dagger}_{i,\sigma'} \frac{1}{\hbar\omega_{\text{in}} + E_g - H_{\text{ch},i} + i\Gamma_n} D_{i,\sigma}|g\rangle. \tag{2.16}$$

We now discuss the numerical techniques used in the later chapters to evaluate the RIXS cross-section.

2.2.1 Exact Diagonalization

Exact diagonalization (ED) can be used to solve model Hamiltonians with electron-electron interactions for simulating strongly correlated materials such as cuprates. The hilbert space for these Hamiltonians grows exponentially with the increase in cluster size for the model. To partially overcome this challenge, one can make use of the sparseness of Hamiltonian and performs the diagonalization using the Lanczos method or ARPACK library [83]. We briefly outline the steps to evaluate the x-ray absorption spectroscopy (XAS) and RIXS cross-section.

Procedure for computing XAS spectra:

1. Set up a cluster model to simulate the material. The Hamiltonian H_0 considers all interactions in the material and is written in the Fock space; H_{ch} considers all interactions in the material along with a core-hole in the system.

2. $|g\rangle$, E_g, and $|n\rangle$, E_n are evaluated by solving H_0 and H_{ch} respectively for a fixed number of particles using an eigen-solver, which in turn is used to evaluate the XAS intensity.

$$\mathcal{I}_{XAS} = \sum_{n,i} \left|\langle n, i|D_i|g\rangle\right|^2 \delta(E_n - E_g - \hbar\omega_{\text{in}}). \tag{2.17}$$

The energy $\hbar\omega_k \rightarrow \hbar\omega_{\text{in}}$ for which XAS has the maximum absorption corresponds to resonance and is used as an incident energy in the RIXS calculation.

Procedure for computing RIXS spectra using Lanczos method:

1. Evaluate the ground state $|g\rangle$ of the Hamiltonian H_0 using the standard Lanczos algorithm.

2. Apply the dipole operator D, for the incoming photon to the initial state as $|v\rangle = D|i\rangle$.

3. Perform a tridiagonalization of the new Hamiltonian with the core-hole H_{ch} in the Krylov basis starting with vector $|v\rangle$ and subsequent diagonalization is carried out and a new vector $|c\rangle = \sum_n \frac{1}{E_n - E_g - \hbar\omega_{\text{in}} + i\Gamma_c}|v\rangle$ is evaluated. The vector $|c\rangle$ is then in the original basis. Here, $\hbar\omega_{\text{in}}$ is the incident energy obtained from the XAS calculation, which is a constant value in our calculation.

4. Apply the outgoing photon transition operator $D'^{\dagger}$ on the vector as $|x\rangle = \sum_i e^{i\mathbf{q}\cdot\mathbf{R}_i} D_i'^{\dagger}|c\rangle$

5. Perform a tridiagonalization of the original Hamiltonian H_0 starting with the vector $|x\rangle$. A subsequent diagonalization is then carried out, which produces

the final states $|f\rangle$ and associated final energies E_f. The overlap of final states, $\langle f|f\rangle$ associated with different final energies is then evaluated.

6. Finally, the RIXS spectra are computed using $\mathcal{I}_{RIXS}(q,\Omega) = |\langle f|f\rangle|^2\delta(E_f - E_g - \Omega)$.

The ED algorithm described above can be easily modified to evaluate other responses such as dynamical spin and charge structure factors.

2.2.2 Dynamical Matrix Renormalization Group

This section is modified version of A. Nocera, U. Kumar, *et al.*, Sci. Rep. **8**, 11080 (2018) [84].

After the development of Dynamical Matrix Renormalization Group (DMRG) in 1992 by White [85, 86], major efforts have been focused on extending it to study real-time dynamics [87]. The development of a RIXS-DMRG formalism is a further stride in this direction. In the existing literature, RIXS studies have been limited to exact diagonalization (ED) methods [57, 88, 89, 90, 91, 92, 93, 94, 95, 96, 97]. It is well known that ED calculations suffer from memory requirements due to growth in the Hilbert space, and hence one is limited to relatively small cluster sizes. Our work with Nocera, A. *et al.* [84] developed a RIXS-DMRG formalism and allows one to shift the bottleneck from memory requirements to computational time.

We can formulate an efficient DMRG algorithm by expanding the square in Eq. (2.15), yielding a real space version of the Kramer-Heisenberg formula. To compact the notation, we define vectors $|\alpha_{j,\sigma}\rangle \equiv [\omega_{\rm in} - H_{{\rm ch},j} + E_g + {\rm i}\Gamma]^{-1} D_{j,\sigma}|g\rangle$. Using this definition, Eq. (2.15) can be written as

$$I(\mathbf{q},\Omega) \propto -{\rm Im}\left[\sum_{i,j=0}^{L-1}\sum_{\substack{\gamma,\gamma'\\ \sigma,\sigma'}} e^{i\mathbf{q}\cdot(\mathbf{R}_i-\mathbf{R}_j)}\langle\alpha_{i,\gamma}|D_{i,\gamma'}\frac{1}{\Omega - H_0 + E_g + {\rm i}\eta}D^{\dagger}_{j,\sigma'}|\alpha_{j,\sigma}\rangle\right]. \quad (2.18)$$

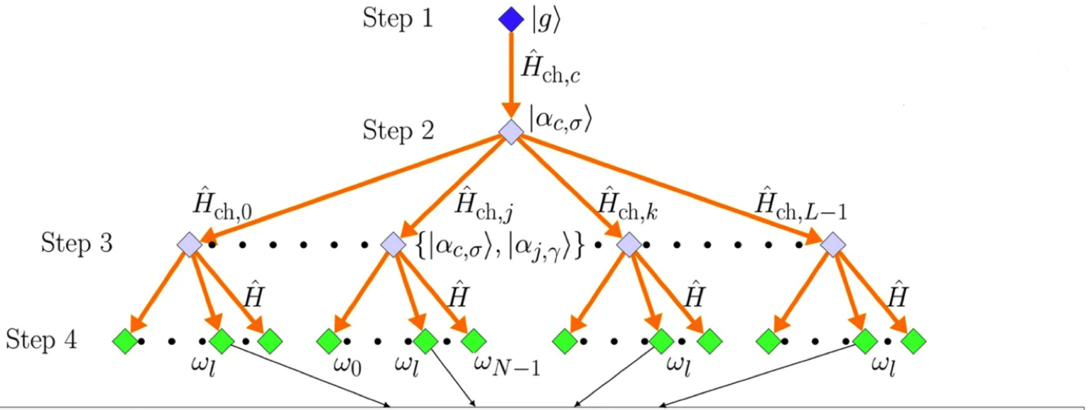

$$I(\mathbf{q},\omega_l) \propto -\text{Im}\left[\sum_{j,\gamma,\gamma',\sigma,\sigma'} e^{\text{i}\mathbf{q}\cdot(\mathbf{R}_j-\mathbf{R}_c)}\langle\alpha_{j,\gamma}|\hat{D}_{j,\gamma'}|x_{c,\sigma',\sigma}\rangle\right] \quad ; \quad |x_{c,\sigma',\sigma}\rangle = \frac{1}{\omega_l-\hat{H}+E_g+\text{i}\eta}\hat{D}^{\dagger}_{c,\sigma'}|\alpha_{c,\sigma}\rangle$$

Figure 2.3: A sketch of the algorithm for computing the real space Kramers-Heisenberg formula [Eq. (2.18)] using the DMRG method at a fixed value of the energy loss $\Omega = \omega_l$.

Here, η is the Lorentian broadening in the RIXS spetra and $\sigma, \sigma', \gamma, \gamma'$ are spin indicies. The L-edge RIXS spectra of cuprates have $\Delta S = 0$ and $\Delta S = 0$ channels. In the DMRG-RIXS algorithm, the $\Delta S = 0$ contribution corresponds to the $\sigma = \sigma'$ and $\gamma = \gamma'$ terms, whereas the $\Delta S = 1$ contribution corresponds to the $\sigma \neq \sigma'$ and $\gamma \neq \gamma'$ terms.

Procedure for computing RIXS spectra using the DMRG method: The algorithm to compute the RIXS spectra using Eq. (2.18) is as follows (see also Fig. 2.3):

1. Compute the ground state $|g\rangle$ of H_0 using the standard ground state DMRG method. The vector $|g\rangle$ must be stored for later use.

2. Target the ground state vector calculated earlier using a different Hamiltonian $H_{\text{ch,c}} = H_0 + H_c^C$, where $j = c$ is the center site of the chain. Construct the vector $|\alpha_{c,\sigma}\rangle$ at the *center* of the chain using the Krylov-space correction vector

approach [98]

$$|\alpha_{c,\sigma}\rangle \simeq \tilde{T}_c^\dagger \tilde{S}_c^\dagger \frac{1}{\omega_{\text{in}} - D_{\text{ch},c} + E_g + \mathrm{i}\Gamma} \tilde{S}_c \tilde{T}_c D_{c,\sigma} |g\rangle, \tag{2.19}$$

where we have performed a Lanczos tridiagonalization $\tilde{T}_c$ with starting vector $D_{c,\sigma}|g\rangle$, and a subsequent diagonalization $\tilde{S}_c$ of the Hamiltonian $H_{\text{ch},c}$, represented in its diagonal form $D_{\text{ch},c}$ in the Krylov basis. The vector $|\alpha_{c,\sigma}\rangle$ should also be stored for later use. Because the cluster is not periodic, the use of a central site here represents an approximation that will become exact in the thermodynamic limit. This central site "trick" was used for the first time in the application of time-dependent DMRG [87].

3. *Restart* from the previous run, now using a different Hamiltonian $H_{\text{ch},j} = H_0 + H_j^C$. Read and then target (in the DMRG sense) the ground state vector calculated in Step 1, as well as the vector $|\alpha_{c,\sigma}\rangle$ constructed in Step 2. For each site j, except for the center site considered in Step 2, construct the vector

$$|\alpha_{j,\gamma}\rangle \simeq \tilde{T}_j^\dagger \tilde{S}_j^\dagger \frac{1}{\omega_{\text{in}} - D_{\text{ch},j} + E_g + \mathrm{i}\Gamma} \tilde{S}_j \tilde{T}_j D_{j,\gamma} |g\rangle, \tag{2.20}$$

with a Lanczos tridiagonalization $\tilde{T}_j$ with starting vector $D_{j,\gamma}|g\rangle$, and a subsequent diagonalization of $H_{\text{ch},j}$. This step of the algorithm requires a number of runs equal to the number of sites minus 1, *i.e.*, $L-1$. These can be run in parallel on a standard cluster machine, restarting from Step 2. Performing Step 2 and Step 3 in this sequence is crucial for having the vectors $|\alpha_{c,\sigma}\rangle$ and $|\alpha_{j,\gamma}\rangle$ in the *same* DMRG basis. The vector $|\alpha_{j,\gamma}\rangle$ should also be stored for later use.

4. *Restart* using the original Hamiltonian H. Read and then target the ground state produced in Step 1, $|\alpha_{c,\sigma}\rangle$ produced in Step 2, and the vector $|\alpha_{j,\gamma}\rangle$ constructed in Step 3. For a fixed $\Omega = \omega_l$, compute the correction vector of

$|\alpha_{c,\sigma}\rangle$ using again the Krylov-space correction vector approach as

$$\begin{aligned}|x_{c,\sigma',\sigma}\rangle &\equiv \frac{1}{\Omega - H_0 + E_g + \mathrm{i}\eta} D^{\dagger}_{c,\sigma'}|\alpha_{c,\sigma}\rangle \\ &= \tilde{T}^{\dagger}\tilde{S}^{\dagger}\frac{1}{\Omega - D_0 + E_g + \mathrm{i}\eta}\tilde{S}\tilde{T}D^{\dagger}_{c,\sigma'}|\alpha_{c,\sigma}\rangle, \end{aligned} \tag{2.21}$$

with a Lanczos tridiagonalization $\tilde{T}$ (using $D^{\dagger}_{j,\sigma'}|\alpha_{c,\sigma}\rangle$ as the seed) and a subsequent diagonalization $\tilde{S}$ of the Hamiltonian H_0, with D_0 being the diagonal form of H_0 in the Krylov basis. This is a crucial part of the algorithm, which amounts to computing the correction vector $|x_{c,\sigma',\sigma}\rangle$ of a previously calculated correction vector $|\alpha_{c,\sigma}\rangle$. Execute this computation N_Ω times for $\Omega \in [\omega_0, \omega_{N-1}]$.

5. Finally, compute the RIXS spectrum in real space $I_{j,c}(\Omega) \propto \langle \alpha_{j,\gamma}|D_{j,\gamma'}|x_{c,\sigma',\sigma}\rangle$ (in $I_{j,c}(\Omega)$ we omit the spin indices $\gamma, \gamma', \sigma, \sigma'$ in order to lighten the notation) and then Fourier transform the imaginary part to obtain the RIXS intensity

$$I(\mathbf{q}, \Omega) \propto -\mathrm{Im} \sum_{\substack{j,\gamma,\gamma' \\ \sigma,\sigma'}} e^{i\mathbf{q}\cdot(\mathbf{R}_j - \mathbf{R}_c)} I_{j,c}(\Omega). \tag{2.22}$$

Computational complexity — The computational cost required for DMRG to compute the RIXS spectrum can be easily estimated, assuming that the ground state of the Hamiltonian has already been calculated. Let C_{2-3} be the computational cost (*i.e.,* the number of hours) for a single run in Step 2 (1 run only) or Step 3 ($L-1$ runs in total). Let C_4 be the computational cost for a single run in Step 4. The total computational time needed to compute the RIXS spectrum is then $\mathrm{CPU}_{\mathrm{cost}} = C_{2-3}L + C_4 L N_\Omega$, where N_Ω is the number of frequencies needed in a given interval of energy losses. As explained in the previous section, we use a center site "trick" to reduce the computational cost by a factor of the order of L [Eq. (2.18) to Eq. (2.22)]. The computational cost C_4 for Step 4 follows the typical performance profile of the Krylov-space approach found in Ref. [98], where less CPU time is needed to compute the spectra at lower energy-losses. We also note that the calculation of each energy loss is trivially parallelizable.

Chapter 3

Observation of two-spinon and four-spinon excitations in corner-shared Sr_2CuO_3 using oxygen K-edge resonant inelastic x-ray scattering study

This chapter is a modified version of J. Schlappa, U. Kumar, *et al.*, Nat. Commun. **9**, 5394 (2018) [57].

3.1 Introduction

In this chapter, we present the recent observation of four-spinon excitations in a one-dimensional (1D) Heisenberg antiferromagnet material using resonant inelastic x-ray scattering (RIXS).

When confined to 1D, systems of interacting electrons host an assortment of macroscopic many-body phenomena, including quantum critical magnetic states with collective excitations carrying fractional quantum numbers. For this reason, quasi-1D magnetic insulators have attracted wide experimental and theoretical interest as an ideal playground for studying quantum many-body phenomena. Owing to numerous experimental realizations of such models in real materials, some of the most stringent tests of quantum many-body theory have been conducted in 1D [2, 5, 41, 46, 70, 94, 96, 99, 100, 101, 102, 103, 104, 105, 106, 107, 108, 109].

The 1D Heisenberg antiferromagnet (HAFM), where localized spins S interact with their nearest-neighbors via an exchange interaction J, is perhaps the simplest and best understood of these systems; the spin-1/2 case is an important reference system that can be solved exactly using the Bethe ansatz. The ground state is a macroscopic $SU(2)$-symmetric singlet, in which quantum fluctuations suppress long-range order, leading to a spin liquid ground state even in the limit of zero temperature. The elementary excitations are collective spin density fluctuations called spinons, which are fractional excitations carrying spin-1/2 but no charge. Spinons generated experimentally in 1D HAFM through an elementary spin-flip process, e.g. during inelastic neutron scattering (INS) or RIXS are created in pairs. As such, the low-energy magnetic excitations are spanned by states involving an even number of spinons forming manifolds of two-, four-, six-spinon continua and so forth.

The magnetic excitation spectrum has been observed for different realizations of the 1D HAFM by INS [41, 46, 70, 99, 100] and by RIXS [1, 5, 88, 90, 102]. The spectral weight captured by these studies, assigned to the triplet manifold, is located entirely within the boundaries of the two-spinon continuum. The reason for this is now well understood through applications of analytical theory [110, 111] or numerical approaches like density matrix renormalization group [104, 105]. While the allowed phase space for four-spinon excitations (and greater) is much larger than for two-spinon excitations [88, 111], kinematic constraints on the matrix elements between the spinon manifolds lead a situation where the multi-spinon states only contribute significantly for momentum and energy transfers within the boundaries of the two-spinon continuum. This picture has been confirmed by detailed comparisons between

INS experiments [41, 104] and exact calculations of the dynamical structure factor (DSF) [41, 110, 111], which find the two-spinon excitations account only for 73-74% of the total detected spectral weight, while four-spinon excitations exhaust the majority of the remaining sum rule.

While the exact solution of the pure HAFM model predicts that the DSF does have a small amount of spectral weight located between the upper boundary of the two-spinon continuum and the upper boundary of the four-spinon continuum [111], such a small signal has yet to be detected. Four-spinon excitations have been reported outside of the two-spinon continuum in the metallic 4f electron material Yb_2Pb_2Pb [112] and the 1D ferromagnet $LiCuVO_4$ [106, 107, 108]. Both materials, however, have physics beyond the simple HAFM such as long-range hopping in Yb_2Pb_2Pb or frustration in $LiCuVO_4$. A direct observation of higher-order spinon excitations separated from the two-spinon continuum in the prototypical case of a 1D HAFM with nearest-neighbor interactions only is still lacking. Here, we show that RIXS at the O K-edge allows for such an observation, a capability that results from the fundamentally different correlation function that it probes compared to e.g. the spin density pair correlation function of the DSF [88, 113].

RIXS is a photon-in photon-out spectroscopy technique where photons inelastically scatter from a sample [1]. In a RIXS experiment, the photon energy $\hbar\omega_{\text{in}}$ of the incident X-rays is tuned close to an absorption edge of an atomic species in the material of interest, thereby initiating an electron transition between a core level and an unoccupied valence band state. This process creates an intermediate state with an additional electron either in the valence or conduction band and a hole in the core level. This core-hole excited state will decay on a femtosecond time scale, leaving the system in a long-lived valence-band excited state. Since x-ray photons carry substantial momentum (in contrast to the light of optical or VUV wavelengths), the triggered valence-band excitations can be studied both in the energy and the momentum domain. Thus, RIXS can be viewed as momentum-resolved resonant Raman spectroscopy, suitable for mapping dispersions of excitations in quantum materials. The RIXS selection rules allow studies of magnetic excitations with $\Delta S_{\text{tot}} = 0$ (where S_{tot} is the total spin of the system) and, in case of a strong spin-orbit coupling in the initial, intermediate or final state, $\Delta S_{\text{tot}} = 1$.

RIXS has been used to probe electronic excitations involving charge [1, 5, 109], orbital [5, 102, 109], spin [2, 5, 28, 30, 102, 114, 115], and lattice [94, 116] degrees of freedom in a wide range of materials. Studies on the dynamic magnetism have largely focused on cuprates, where $\Delta S_{\text{tot}} = 1$ direct spin-flip excitations can be investigated at the Cu L_3-edge [29]. Indeed, in Cu L_3 RIXS measurements of the quasi-1D spin chain cuprate Sr_2CuO_3, two-spinon continuum excitations could be probed (with indications of also four-spinon excitations) [5]. Studies in other cuprate materials revealed two-triplon excitations in the spin-ladder system $\text{Sr}_{14}\text{Cu}_{24}\text{O}_{41}$ [2] and magnon excitations in many quasi-two-dimensional superconducting cuprates [28, 29, 30, 116].

In this chapter, we report momentum-resolved oxygen K-edge RIXS studies of the quasi-1D spin-chain cuprate Sr_2CuO_3, one of the best realizations of the 1D HAFM. We observe magnetic excitations that exist in two non-overlapping regions of phase space. Through detailed modeling within the $t - J$ model, we show that one set of these excitations is quite similar to triplet excitations generally associated with the DSF while the other set corresponds to predominantly four-spinon excitations. Specifically, four-spinon excitations centered at 500 meV energy transfer give a strong and broad response around the Γ-point ($q = 0$, where q is the momentum transfer along the chain) that is well separated from the boundaries of the two-spinon continuum. Our results constitute the discovery of a new channel for the creation of magnetic excitations in 1D materials, beyond those resulting from elementary spin-flip excitations. We argue that this capability stems from the charge dynamics of the intermediate state, which grants access to fundamentally different correlation functions, not captured by a simple two-site correlation function.

3.2 Methods

3.2.1 Experiment

Our collaborators performed experiments at the ADRESS beamline of the Swiss Light Source at the Paul Scherrer Institut [117, 118] and provided us the experimental data. Single-crystal samples of Sr_2CuO_3 were grown by the floating-zone method and freshly cleaved before the RIXS experiment. The technique of high-resolution resonant inelastic x-ray scattering (RIXS) with the incident photon energy tuned to the O K-edge ($1s \rightarrow 2p$) (around 528.6 eV) was used to probe the material. During experiment, the surface normal to the sample, [010], and the propagation direction of the chains, [100], were oriented parallel to the scattering plane, which was horizontal. The sample was cooled with a helium-flow cryostat to 14 K during the measurements. Incident photons were linearly polarized either in the scattering plane (π-polarization), which was the case for most of the data, or perpendicular to the scattering plane (σ-polarization). The XAS data was measured in total fluorescence yield. The beamline (BL) energy resolution was set to 70 meV or better, with the BL exit slit open to 30 μm (the BL energy resolution for the Cu L_3 data [5] was 100 meV or better, with the BL exit slit open to 10 μm.) The RIXS spectrometer was located at a fixed scattering angle of $\psi = 130^\circ \pm 1^\circ$, whereas the incidence angle on the sample varied between $10^\circ \pm 1^\circ$ and $110^\circ \pm 1^\circ$ grazing (see Fig. 2.2 in chapter 2). The angular horizontal acceptance of the spectrometer was approximately 5 mrad [119]. The total experimental energy resolution was 80 meV and the simultaneously recorded energy window was 22.2 eV (the total experimental resolution for the Cu L_3 data [5] was 140 meV and the simultaneously recorded energy window was 59.2 eV).

3.2.2 Cluster Calculations

The RIXS intensity $I(q, \Omega)$ was evaluated using the Kramers-Heisenberg formalism where ($\hbar = 1$)

$$I(q,\Omega)=\sum_{f}\Big|\sum_{n,R_m} e^{-iqR_m}\frac{\langle f|D_m^{\dagger}|n\rangle\langle n|D_m|i\rangle}{E_g+\omega_{\text{in}}-E_n+i\Gamma}\Big|^2\delta(E_f-E_i+\Omega). \tag{3.1}$$

Here, $q=\mathbf{e_x}\cdot(\mathbf{k}_{\text{out}}-\mathbf{k}_{\text{in}})$ is the momentum transfer along the x-axis and $\Omega=\omega_{\text{out}}-\omega_{\text{in}}$ is the energy loss, D is the dipole operator, and $|i\rangle$, $|n\rangle$, and $|f\rangle$ are the initial, intermediate, and final states of the RIXS process with energies E_i, E_n, and E_f, respectively, $R_m=am$ is the position of m^{th} Cu atom, a is the Cu-Cu distance, and Γ is the core-hole lifetime. We compute the eigenstates by diagonalizing $t-J$ Hamiltonian defined on a twenty-two site cluster. The use of this low-energy effective model is justified since all of the *dd* and charge-transfer excitations appear well above 1.5 eV in energy loss [see Fig. 3.1(c)]. Moreover, recent DMRG calculations have explicitly shown that the magnetic excitations probed by Cu *L*-edge RIXS obtained from a four orbital *pd*-model for Sr_2CuO_3 can be accurately reproduced using an effective $t-J$ Hamiltonian [84] up to an overall rescaling of the intensity. This result gives us confidence that the downfolded $t-J$ Hamiltonian can capture the magnetic excitations of Sr_2CuO_3. At the oxygen K-edge, dipole operator in the effective model is given by $D_m=\sum_{\sigma}(d_{m,\sigma}-d_{m+1,\sigma})s^{\dagger}_{m,\sigma}$ where $d_{m,\sigma}$ annihilates a spin σ hole on Cu site m and $s^{\dagger}_{m,\sigma}$ creates a hole in the oxygen $1s$ orbital on the site between the m and $m+1$ Cu sites. Here, the relative phases reflect the phases of the original Cu-O overlap integrals. The model parameters are $t=300$ meV and $J=250$ meV, which is appropriate for Sr_2CuO_3 [5, 96], and $\Gamma=150$ meV for the oxygen K-edge [94, 109].

3.3 Results

3.3.1 Experimental results

The low-energy electronic degrees of freedom in the charge transfer insulator Sr_2CuO_3 are formed from the CuO_4 plaquettes, which are arranged into 1D corner-shared chains [5, 120], as shown in Fig. 3.1(a). In the atomic limit, the Cu ion is

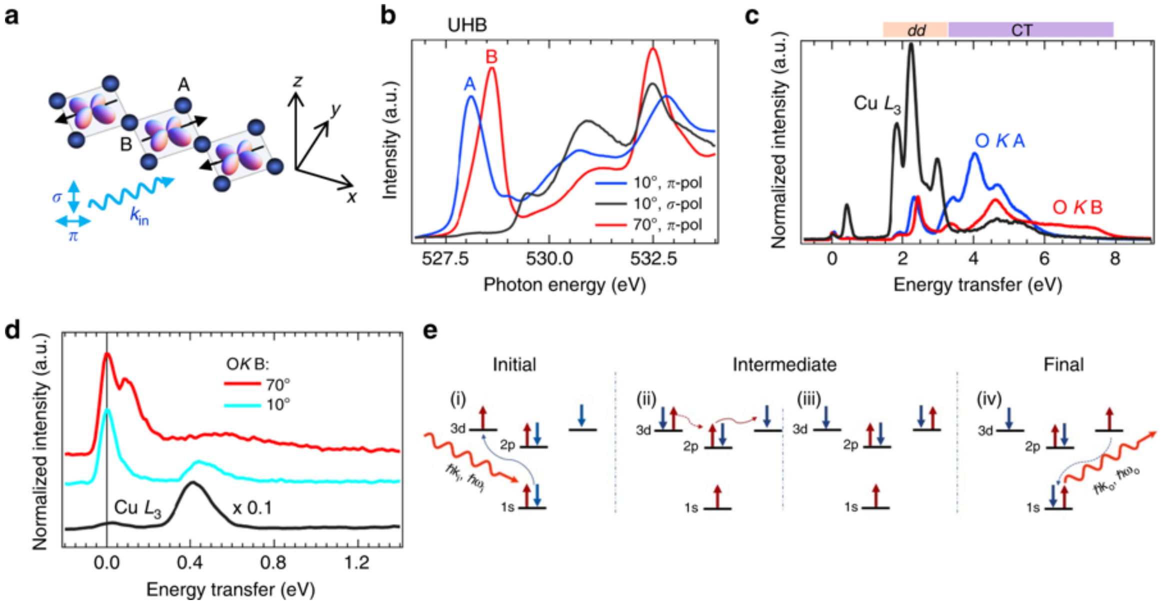

Figure 3.1: Summary of the experimental data at the oxygen K-edge. (a) A cartoon sketch of the Cu-O-Cu corner-shared chains forming the active low-energy degrees of freedom in Sr_2CuO_3, and of the incident-light geometry. The Cu atoms are primarily in a d^9 valence state, where a single hole occupies each of the Cu $3d_{x^2-y^2}$ orbitals and interacts antiferromagnetically with its in-chain neighbors. (b) The polarization dependence of the XAS spectra. σ-polarized light (black solid line) probes unoccupied states perpendicular to the CuO_4-plaquettes, having no spectral weight at the UHB (there are no apical oxygens). Data obtained with π-polarized light at incidence angles of 10° (grazing incidence geometry, blue line) and 70° (close to normal incidence and $q \approx 0$, red line) and 10° (grazing incidence geometry and $q \approx \pi/2a$) primarily probes the out-of-chain (A) and in-chain (B) oxygen sites, respectively. The difference in the pre-peak resonance corresponds to the differences in the chemical environments of these two oxygen sites (chemical shifts), where the B site hosts the plaquette-connecting oxygen orbital [120]. (c) Polarization dependence for π-polarized O K-edge RIXS data for incident energies tuned to the A (blue) and B (red line) peaks in the XAS shown in panel (b) [Incident angles as in (b): 70° (10°) corresponds to $q \approx 0$ ($q \approx \pi/2a$)]. The π-polarized Cu L_3-edge RIXS data at 20° incidence angle ($q \approx \pi/2a$) is also shown for comparison (black line). The RIXS spectra are normalized to acquisition time. The peaks above 1.8 eV energy transfer are associated to dd (orbiton) and charge transfer (CT) excitations, as indicated. The peak below 0.6 eV in the Cu L_3 data corresponds to multi-spinon excitations [5]. (d) The Cu L_3 and O K B-resonance RIXS data from panel (c) and B-resonance for 10° incidence angle ($q \approx \pi/2a$, turquoise line), now focusing on the first 1.3 eV energy loss, where several low-energy spin excitations are found. The RIXS data are reported in arbitrary units (a. u.). (e) A sketch of the double spin-flip process across two Cu sites at the oxygen K-edge.

in a d^9 valence state, with a single hole occupying the Cu $3d_{x^2-y^2}$ orbital. There is, however, significant hybridization between the Cu 3d and 2p orbitals of the surrounding oxygen, resulting in a substantial isotropic superexchange interaction $J \sim 250$ meV [5, 96, 46] between the Cu spins. In the real material, the individual -Cu-O-Cu- chains are weakly coupled such that the system has a bulk Néel temperature of $T_N \approx 5$ K [101]. Above this temperature, however, the chains decouple and become nearly ideal realizations of the 1D HAFM, as evidenced by the observation of the two-spinon continuum in INS [46] and Cu L_3 RIXS [5]. The latter RIXS study also found evidence for novel spinon-orbiton separation effects in Sr_2CuO_3, further underscoring the importance of the 1D physics.

Fig. 3.1(b) shows the x-ray absorption (XAS) data of Sr_2CuO_3 measured at the O K-edge (a $1s \rightarrow 2p$ resonance). The intensity reflects the partial density of the unoccupied valence and conduction band states, here projected onto the oxygen orbitals. We observe a sharp excitonic structure in the pre-edge region and broad continuum states at energies above 529 eV. The excitonic peak corresponds to excitations of the O $1s$ core electron into the upper Hubbard band (UHB), creating a Cu $3d^{10}$ state [120]. This excitation is allowed by the sizable hybridization between the O $2p$ and Cu $3d$ orbitals. The UHB XAS peak depends strongly on the polarization of the incident photons reflecting the strong structural and electronic anisotropy of the system [120]. In particular, the suppression of intensity for $\sigma-$polarized light indicates that the unoccupied states are oriented in the plane of the CuO_4 plaquettes, whereas the energy shift upon changing the incidence angle of $\pi-$polarized light reflects differences in coordination between the out-of-chain and the in-chain oxygens (indicated in Fig. 3.1(a) as sites A and B, respectively), in agreement with previous findings [121]. For the remainder of this work, we focus on RIXS spectra recorded with the incident photon energies tuned to the UHB B (or A) peak, where an in-chain (or out-of-chain) O $1s$ core electron is promoted into a neighboring Cu $3d$ orbital. This final state of the XAS process dictates the intermediate state of RIXS and is important in determining the scattering cross-section.

Fig. 3.1(c) shows RIXS spectra measured with the incident photon energy tuned to the resonance of the A and B peak at the O K-edge in comparison with Cu L_3-edge data at $q = \pi/2a$. There are two energy regions with pronounced excitations: one below 1 eV and one above 1.5 eV, separated by a region of very weak spectral weight. The excitations at higher energies are dominated by inter-orbital dd and charge transfer (CT) excitations [5, 96]; the dd excitations are dominant at the Cu L_3-edge, whereas the CT excitations are dominant at the O K-edge.

Fig. 3.1(d) zooms in on the low-energy excitation region, well below the dd and CT excitations, which is our focus. O K RIXS for photon energies tuned to B with different incident angles are compared to low-energy Cu L_3 RIXS data. Below 1 eV we see several excitations. In addition to the elastic line at zero energy loss, we observe a weakly dispersing excitation at $\approx$ 90 meV with varying cross section for the different configurations. This behavior is typical of an optical phonon excitation and the energy scale agrees well with that of a Cu-O bond-stretching lattice vibration [94]. We, therefore, assign this feature to such a phonon. The A line spectrum at $q = \pi/2a$ [see Fig. 3.1(d), turquoise solid line Fig. 3.1(d)] reveals a sharp structure coinciding with the very strong spinon excitations at the same $q-$point in Cu L_3-edge data (black line, note that the Cu L_3 spectrum is divided by a factor 10). In addition, the line spectrum cut taken close to the Γ-point [red line in Fig. 3.1(d) Fig. 3.2(e)] is dominated by a broad structure, centered at around 0.5 eV and extending to about 1 eV in energy transfer. The energy of this structure is well separated from the dd and CT excitations, suggesting that they are magnetic in origin. A possible path for creating magnetic excitations during RIXS at the O K-edge is sketched in Fig. 3.1(e). This process will be discussed in more detail in the Discussion section.

To probe the dynamic character of these low-energy magnetic excitations visible in the O K-edge RIXS spectra, we have studied their momentum dependence for momentum transfer along the chain direction, as shown in Fig. 3.2(a). O K-edge RIXS can access about 25% of the first Brillouin zone along [100] on each side of

$q = 0$. The experimental geometry is described in Fig. 2.2 of Chapter 2. Additional comparisons of the data with the Cu L_3-edge are provided in Sec. 3.3.2.

In addition to the strong phonon excitation in O K-edge data, there are two distinct sets of continua in the magnetic region between 0.2 eV and 1.0 eV. Sr_2CuO_3 is known to host 1D HAFM physics, and the manetic excitations for this system are spinons. The upper and lower boundaries of the two-spinon continuum are given by $\omega_{2s}^{u} = \pi J|\sin(qa/2)|$ and $\omega_{2s}^{l} = \pi J|\sin(qa)|/2$, respectively. The upper and lower boundary of the four-spinon continuum are given by $\omega_{4s}^{u} = \pi J\sqrt{2[1 + |\cos(qa/2)|]}$ and $\omega_{4s}^{l}(q) = \pi J|\sin(qa)|/2$, respectively [111].

One set of excitations is dispersing towards zero energy for $q = 0$ and lies well within the boundaries of the two-spinon continuum (indicated by the white dotted lines). The second region is centered at q =0 and 500 meV energy transfer and is clearly situated outside of the two-spinon continuum. The boundaries in Fig. 3.2 correspond to the two-spinon continuum expected for the 1D HAFM model obtained from purely kinematic constraints assuming a superexchange value of $J = 250$ meV, as inferred from prior scattering experiments [5, 46]. Comparison to Cu L_3 data displayed in Fig. 3.2(b) and 3.2(c), where the two-spinon continuum dominates the spectrum, illustrates that O K-edge and Cu L_3-edge RIXS have quite different responses in terms of the magnetic excitations. However, the line cuts of O K-edge and Cu L_3-edge RIXS spectra in Fig. 3.2(f) 3.2(c) show that there is also a finite weight in Cu L_3-edge RIXS spectra at $q = 0$. Note that the O K-edge data reveal much stronger polarization dependence due to the difference in connectivity of the in-chain and out-of-chain O $2p$ orbitals.

The fact that the Γ-point excitations appear outside of the boundaries of the two-spinon continuum, and well below the energy losses where dd and CT-excitations occur suggests that they are multi-spinon in nature. This interpretation is further supported by the fact that they lie completely within the boundaries expected for the four-spinon continuum (indicated by dashed lines, as obtained from pure kinematic arguments of four-spinons).

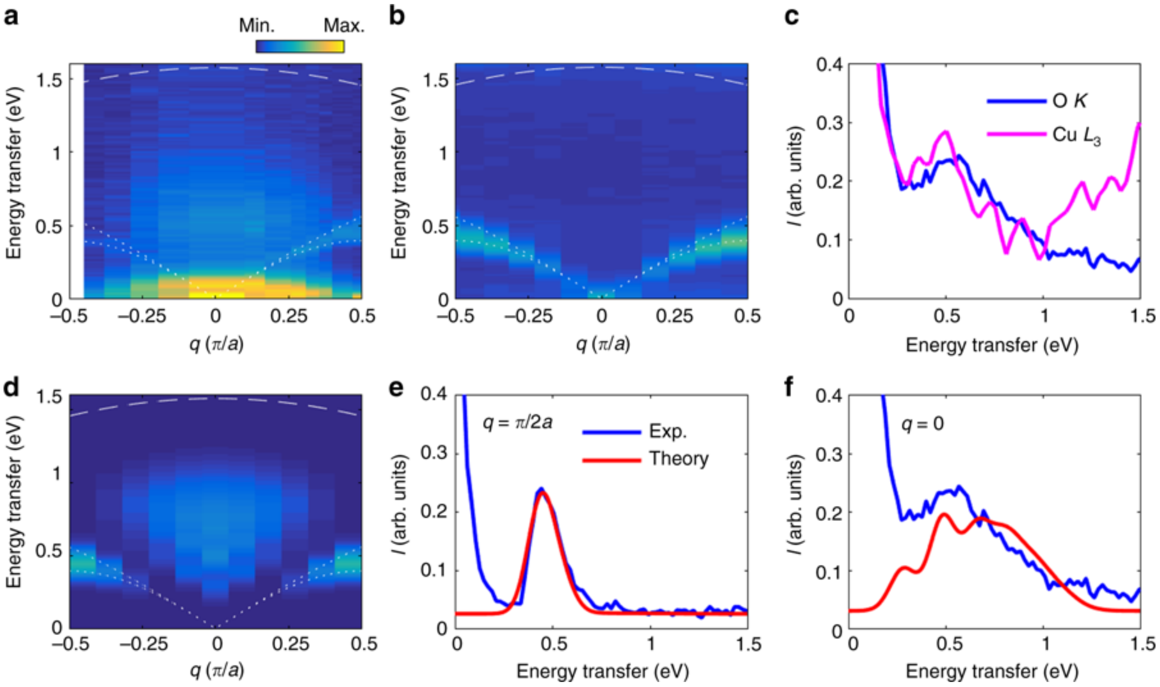

Figure 3.2: Comparison between the experimental and calculated RIXS spectra at the oxygen K-edge. (a),(b) The experimental RIXS spectra as a function of momentum transfer and energy transfer measured at: (a) the oxygen K-edge with an incident photon energy of $\hbar\omega_{\text{in}}$=528.6 eV (resonance B) and (b) the copper L_3-edge from Ref. [5]. (c) compares the O K-edge (blue) and Cu L_3-edge (magenta line) RIXS line cuts at $q = 0$. In the case of Cu L_3 data, there is a tailing contribution from higher energy dd excitations, which extends down to low energy loss [see Fig. 3.1(c)]. (d) displays the calculated oxygen K-edge spectra are for $\hbar\omega_{\text{in}} = 500$ meV. (This value optimizes the intensity of the four-spinon features, see Sec. 3.3.2.) The excitation at ∼90 meV in the oxygen K-edge data is a phonon excitation not included in our model calculations. The modeled RIXS intensity was obtained from exactly diagonalizing a 22-site $t - J$ chain with periodic boundary conditions and the elastic line has been removed from the data for clarity. (e), (f) show line cuts of the RIXS spectra at $q = \pi/2a$ and $q = 0$, respectively. The experimental (theoretical) data are represented by the blue (red) solid lines. The dotted and dashed white lines in (a), (b) and (d) indicate the boundaries of the two- and four-spinon continua, respectively.

3.3.2 Theoretical results

The phase space considerations given above identify the Γ-point excitations belonging to multi-spinon excitations involving at least four or more spinons. However, to understand the spectral weight of these excitations it is necessary to compute the RIXS intensity within the Kramers-Heisenberg formalism, due to the prominent role played by the core-hole lifetime at the O K-edge. To this end we performed small cluster exact diagonalization (ED) calculations to further elucidate the nature of these excitations. Since we are interested in the energy region well below the dd- and CT-excitations, we used the $t-J$ model, where these multiorbital processes have been integrated out [84]. In this case, we adopt values of the hopping integral $t = 300$ meV and superexchange interaction $J = 250$ meV, which are consistent with existing literature (see Sec. 5.2). The computed spectra (with elastic peak removed) are compared against the experimental data in Fig. 3.2(d). Line cuts of the data superimposed over the calculations are shown in Figs. 3.2(e) ($q \approx q/2a$) and 3.2(f) ($q = 0$).

The overall agreement between the calculated magnetic response and the experimental data is excellent: our model captures both the dispersing magnetic excitations and the broad continuum centered at the Γ-point. Even the quantitative agreement is very good. Note that the phonon excitation is not included in the theory; therefore, we do not capture this low-energy excitation. If the spin-lattice coupling is weak, we expect that the inclusion of the lattice vibrations would superimpose a phonon excitation on the RIXS spectrum. In this case, the level of agreement between the model and the data in the magnetic region indicates that any spin-lattice coupling is small and that the final states of the O K-edge RIXS process can be well described solely by excitations of the half-filled $t-J$ model, whose final states are the same as those in the Heisenberg model. This observation justifies our neglecting of the lattice excitations and allows us to identify the upward dispersing branch as two- and four-spinon excitations, commonly associated with the DSF, while the continuum

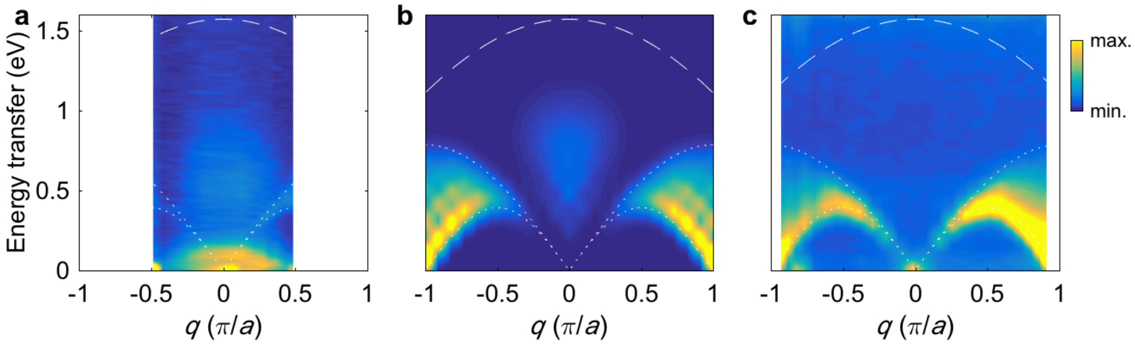

Figure 3.3: RIXS spectra plotted over the full first Brillouin zone. (a) The experimental spectra at the O K-edge shown in the momentum range accessible to the experiment. (b) The calculated RIXS spectra at O K-edge over the entire 1st BZ. (c) the experimental data at Cu L_3-edge. The dotted and dashed lines overlaid over the data shows the boundaries for the two- and four-spinon continuua respectively.

of excitations centered at $q = 0$ corresponds to four-spinon excitations that require a more complex correlation function. This assignment is further supported by the dependence of these excitations on the core-hole lifetime, which will be discussed shortly.

RIXS spectra in the full Brillouin zone

Due to the relative low energy of x-ray photons used for the excitations at the oxygen K-edge, the technique can only access about half of the first Brillouin zone (BZ). On can, however, measure out to the Brillouin zone boundary at other elemental edges such as the Cu $L_{2,3}$-edge. Similarly, we can also compute the RIXS spectra throughout the entire BZ. By examining the magnetic excitations throughout the 1st BZ, we can gain further insight into their identities. Fig. 3.3 compares the measured and calculated RIXS spectra over the available momentum-transfer range: O K-edge data [Fig. 3.3(a)], theory [Fig. 3.3(b)], Cu L_3-edge data [Fig. 3.3(c)]. One can see that the calculated weight of the dispersing branch agrees well with the continuum observed at the Cu L_3-edge (primarily due to two-spinon excitations) out to the zone boundary.

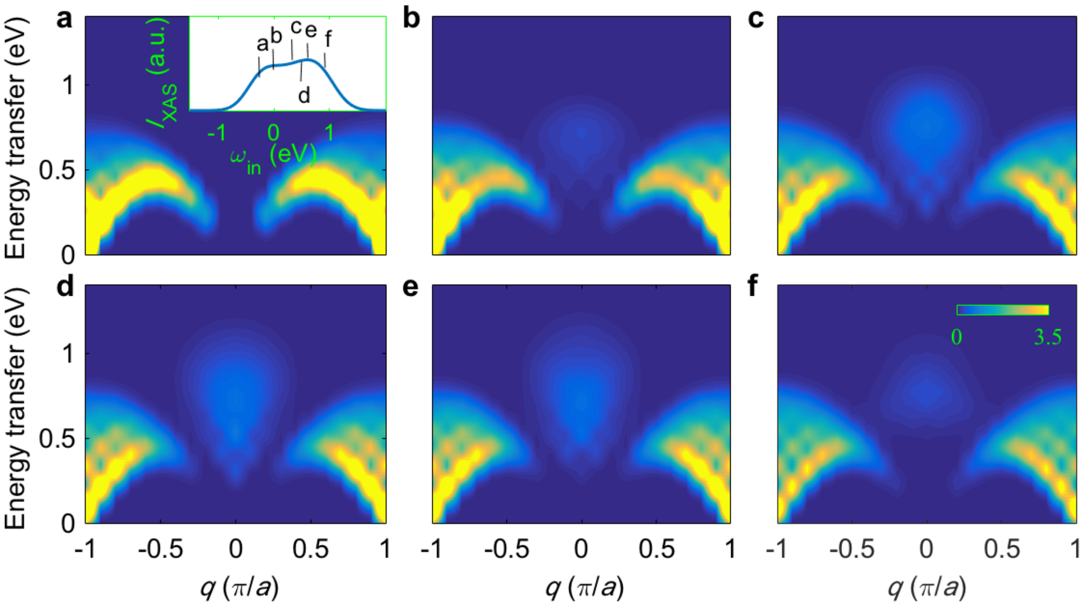

Figure 3.4: RIXS spectra dependence on the incidence energy. Panels (a)-(f) show the RIXS spectra evaluated at various incident energies as indicated in XAS spectra shown in the inset of panel (a).

Incidence energy dependence

Fig. 3.4 shows how the various magnetic excitations depend on the incident photon energy in our model. The multi-spinon excitations that are prominent at $q = 0$ are very sensitive to the incident energies compared to the dispersing two-spinon excitations, and the multi-spinon excitations have the largest spectral weight for ω_{in} in the range of 0.3 eV to 0.6 eV. This sensitivity to the incident photon energy indicates that the multi-spinon excitations found outside of the two-spinon continuum are more effectively reached via particular intermediate states of the RIXS process.

3.4 Discussion

How can we understand the magnetic excitations in RIXS captured by the $t - J$ model, and why do we see magnetic excitations that are absent in INS? In Fig. 3.5, we illustrate schematically the magnetic excitation mechanisms in a spin chain with the different scattering techniques: INS [Fig. 3.5(a)], Cu $L_{2,3}$- [Fig. 3.5(b)], and O K-edge RIXS [Fig. 3.5(c) & 3.5(d)]. The ground state of the HAFM is an $SU(2)$ symmetric singlet with $S_{\text{tot}} = 0$. INS measurements connect this ground state to the triplet manifold with $S_{\text{tot}} = 1$ at low temperatures, such that $\Delta S_{\text{tot}} = 1$. In a simplified picture (shown here for $\Delta S_z = \pm 1$), such excitation creates two domain walls in the spin chain [Fig. 3.5(a)], which decay predominantly into two-spinons carrying parallel spins of 1/2 (due to conservation of angular momentum). Exact calculations [111] show that these excitations also have overlap with four-spinon excitations, but the majority of the four-spinon weight remains within the boundaries of the two-spinon continuum due to kinematic constraints in the matrix elements.

Unlike INS (and RIXS at the Cu $L_{2,3}$ edges), excitations with $\Delta S_{\text{tot}} = 1$ are generally forbidden for K-edge RIXS. (This statement holds only for materials with small spin-orbit coupling in the valence band; single-flips are allowed in O K-edge RIXS on iridates, see Ref. [123].) Instead, $\Delta S_{\text{tot}} = 0$ processes like the one sketched in Fig. 3.1(e) must be used to create magnetic excitations. Here, the incident photon creates a Cu $3d^{10}$ UHB excitation in the intermediate state, resulting in a Cu site with an additional “spin-down” electron in direct vicinity to an O $1s$ core hole (represented in the sketch as blue arrow (spin down) on the left-hand Cu-side). The 180° Cu-O-Cu bonding angle in Sr_2CuO_3 enables efficient double inter-site hopping of $3d$ electrons between two adjacent Cu sites via the bridging in-chain oxygen site [B in Fig. 3.1(a)], transferring the Cu $3d^{10}$ to the neighboring Cu site [right-hand Cu-side in Fig. 3.1(e)]. Since this Cu atom is also hybridized with the oxygen where the core hole is localized, the “spin-down” electron can then decay and fill the core level [see Fig. 3.1(e)], leaving the system with a net double inter-site spin flip. This process, sketched in Fig. 3.5(c), is analogous to an indirect double spin flip process predicted for Cu K-edge RIXS [122, 124] giving rise to a double domain wall that decays predominantly into two-spinons carrying antiparallel spins (due to momentum conservation) [88]. The cross section, in this case, can be related to a dynamic exchange correlation function, whose spectral weight is similar to that of DSF near the zone center [122]. This excitation pathway

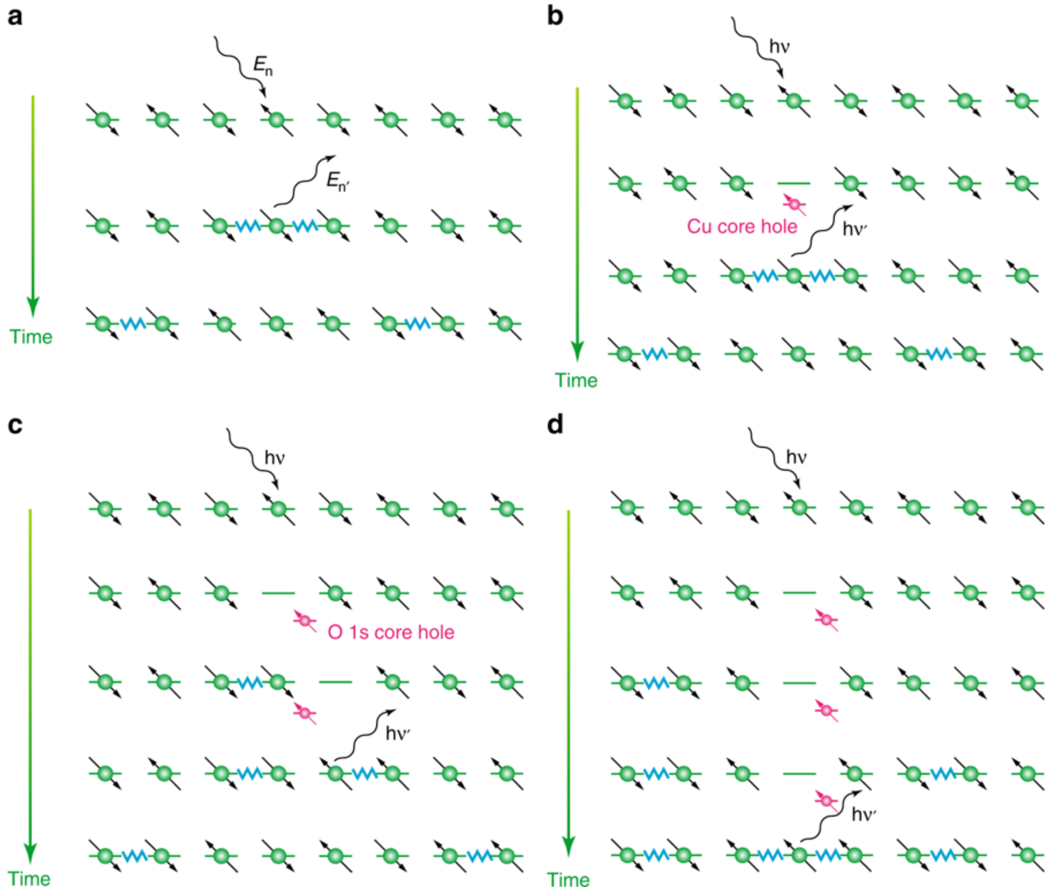

Figure 3.5: An illustration of various spin excitation processes through the creation of spin-flips. (a) The $\Delta S_{\mathrm{tot}} = 1$ direct spin flip process that can occur in an inelastic neutron scattering experiment, which primarily decays into two-spinon excitations that are visualized as domain walls in the antiferromagnetic (AFM) background [41]. (b) The same $\Delta S_{\mathrm{tot}} = 1$ spin flip process in RIXS, which is accessible in materials with strong spin-orbit coupling in the core level [29]. (c) The indirect double spin-flip process at the oxygen K-edge, which occurs via the multi-orbital hopping processes sketched in Fig. 3.1(e). This process generates a nearest-neighbor double spin flip, which predominantly decays into a two-spinon excitation [88, 122]. (d) A second order process at the oxygen K-edge that produces four-spinon excitations. Here, the absence of the spin in the AFM chain allows double spin flips to occur on the sites adjacent to the missing spin. These double spin flips generate spinon excitations away from the site where the core hole is created. The subsequent decay of the core hole then produces two additional spinons in its vicinity. This process requires a long-lived core-hole to allow for sufficient time to generate the two double spin-flips before the core-hole decay occurs.

explains the presence of the sharper dispersing magnetic excitations in O K-edge RIXS spectra. (Note that in two dimensions a $\Delta S_{\text{tot}} = 0$ excitation can only create bi-magnon excitations, as each magnon carries a spin of 1). To visualize the scattering process responsible for the creation of four-spinon excitations around the Γ-point the lifetime of the intermediate state plays a critical role.

As we mentioned previously, in Cu $L_{2,3}$-edge RIXS $\Delta S_{\text{tot}} = 1$ spin-flip excitations that are similar to INS are allowed [32]. This is possible, since for a Cu $2p$ core-hole the spin-orbit coupling is strong and therefore the change of spin momentum can be compensated by the change of orbital angular momentum. In contrast to INS, however, RIXS involves a doublon in the intermediate state, which decays on a timescale set by the corehole lifetime ($\sim$ several fs) [119]. During this time, the additional charge in the intermediate state can interact with the system, creating excitations that are inaccessible through either a single or double spin-flip process. For the O $1s$ core hole there is no appreciable angular momentum available; therefore, the spin momentum must be conserved and only $\Delta S_{\text{tot}} = 0$ excitations are possible (as described above) [Fig. 3.5(c)]. In a 1D system, the result of this $\Delta S_{\text{tot}} = 0$ excitation looks very similar to the result of a single spin flip $\Delta S_{\text{tot}} = 1$ in that both excitations lead to the creation of two domain walls, but at the O K-edge they are separated by at least one atomic site and have opposite spins. The lifetime of O $1s$ core-hole states is somewhat longer than the lifetime of Cu $2p$ core-hole states, however. During this time, the doublon in the $3d$ band can also generate double spin flips on the surrounding sites, as sketched in [Fig. 3.5(d)], creating two additional double spin flips separated by larger lattice distances. The subsequent decay of the core hole results in the creation of two additional domain walls, and a total of four spinons in the final state. This scattering channel is the direct result of fluctuations that take place in the intermediate state. Its intensity, therefore, depends on the lifetime of the core-hole, as a longer-lived doublon will have sufficient time to generate the longer-range double spin-flips, separated by large lattice distances. This new excitation

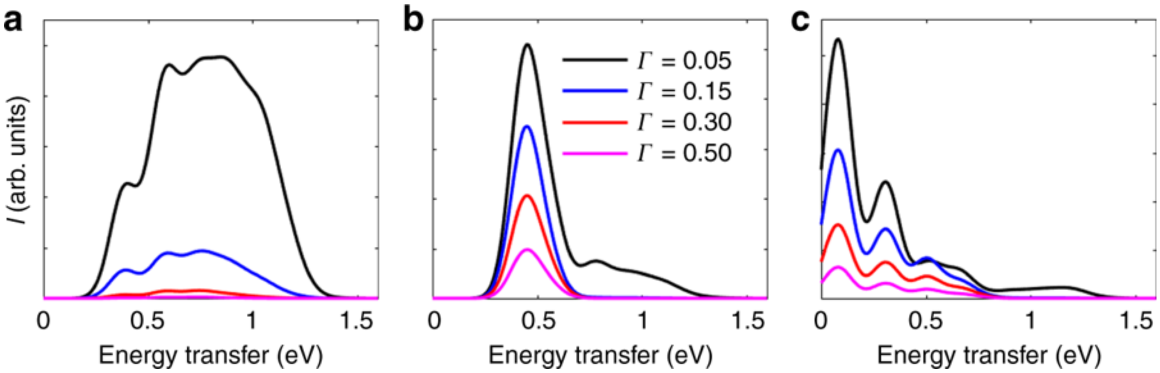

Figure 3.6: The effect of the core-hole lifetime on the RIXS spectra. The variation in the computed RIXS intensity at momentum transfer (a) $q = 0$, (b) $q = \pi/2a$, and (c) $q = \pi/a$. As the core-hole lifetime is decreased (increasing Γ), the four-spinon excitations at $q = 0$ disappear rapidly, while the two-spinon contributions to the spectra at $q = \pi/2a$ and $q = \pi/a$ are more robust.

channel is expected to be weak in Cu L_3 RIXS, whose core-hole is short lived, and completely absent in INS.

We performed calculations for the dependence of these excitations on the lifetime of the intermediate state to test our interpretation. The results are presented in Fig. 3.6. We observe that upon decreasing the core-hole lifetime (increasing Γ) the intensity of magnetic excitations in O K-edge RIXS decreases. Moreover, the spectral weight of the four-spinon excitations moves towards smaller energy losses [see Fig. 3.6(a)]. The decrease in intensity is much slower for excitations belonging to the two-spinon continuum than for the four-spinon excitations. Whereas the two-spinon excitations are still quite pronounced for $\Gamma = 500$ meV [(b) and (c)], the four-spinon excitations are suppressed below $\Gamma = 300$ meV (a), which is comparable to the superexchange interaction J. The suppression of the four-spinon weight at $q = 0$ proves that the core-hole lifetime sets the time scale for the intermediate state to generate these excitations. As its lifetime is quenched below J ($\sim$ 1.3 fs), there is not enough time for additional double spin-flips to occur in the chain during the frustrating presence of the doublon. The dynamics of this intermediate state plays an important role for the discovered excitation channel for magnetic excitations and produces additional magnetic correlation functions beyond a single or double spin-flip.

3.5 Conclusions

In this chapter, we have demonstrated that RIXS grants access to complementary correlation functions for magnetic scattering compared to INS, which arises from the lifetime and dynamics of the intermediate state. Importantly, this new scattering channel is unique to RIXS and provides access to non-local spin correlation functions beyond two-site correlation functions probed by traditional scattering techniques. O K-edge RIXS has long core-hole lifetimes and is therefore ideal for examining excitations that cannot be detected by INS scattering, as long lifetimes of the intermediate state allow charge fluctuations to take place. We have exploited this fact to observe directly four-spinon excitations of a pure 1D HAFM, located outside the boundaries of the two-spinon continuum. This technique opens another avenue to explore quantum magnetism and quasi-particle fractionalization, which has broad applications in the field of quantum magnetism. Time-resolved studies at the upcoming x-ray free-electron laser (XFEL) sources, for example, European XFEL and Swiss FEL, will hopefully facilitate studying such dynamics at the fs-timescale.

Chapter 4

Multi-spinon and antiholon excitations probed by resonant inelastic x-ray scattering on doped one-dimensional antiferromagnets

This chapter is a modified version of U. Kumar, *et al.*, New J. Phys. **20**, 073019 (2018) [97].

4.1 Introduction

In this chapter, we explore the spin and charge dynamics of doped one-dimenssional (1D) antiferromagnets. Resonant inelastic x-ray scattering (RIXS) spectra allows us to explore these directly in the materials exhibiting 1D antiferromagnetic structures.

1D magnetic systems have attracted considerable interest throughout the scientific community for more than half a century. This interest stems from the fact that these systems provide excellent opportunities to study novel quantum phenomena such as quasiparticle fractionalization or quantum criticality. Moreover, model Hamiltonians of 1D systems can often be solved exactly using analytical or numerical techniques, making them ideal starting points for understanding the physics of strongly correlated materials. For example, the exact solution of the 1D Hubbard model by Lieb and Wu [125] represented a breakthrough in the field, showing that interacting electrons confined to 1D are characterized by spin-charge separation, where electronic quasiparticle excitations *break* into collective density fluctuations carrying either spinless charge ("(anti)/holons") or chargeless spin ("spinons") quantum numbers with different characteristic energy scales. This work inspired an intense search for materials showing spin-charge separation, but it has only been in the last two decades that this phenomenon was observed [22, 23, 48, 126, 127, 128].

RIXS [1] has evolved as an important tool for studying the magnetic excitations in correlated materials [29, 129, 130], complementing inelastic neutron scattering (INS). RIXS, however, is also a powerful probe of orbital and charge excitations, as was succinctly demonstrated by the experimental observation of spin-orbital fractionalization in a Cu L-edge RIXS study of Sr_2CuO_3 [5, 96]. Sr_2CuO_3 contains 1D chains of corner-shared CuO_4 plaquettes [see Fig. 4.1(c)], where a single hole occupies each Cu $3d_{x^2-y^2}$ orbital, forming a quasi-1D spin-$\frac{1}{2}$ chain. Due to a very weak interchain interaction, the CuO_3 chains decouple above the bulk ordering temperature $T_N = 5.5$ K and form a nearly ideal realization of a 1D antiferromagnet (AFM) [121]. A recent O K-edge RIXS study [57] of undoped Sr_2CuO_3 directly observed multi-spinon excitations outside of the two-spinon (2S) continuum (see also Fig. 4.1) further highlighting the potential for RIXS to probe such excitations.

To date, spin-charge separation has not been observed using RIXS [96]. In this chapter, we performed exact diagonalization (ED) and density matrix renormalization group (DMRG) [85, 86] calculations to show that RIXS measurements on doped 1D AFMs can fill this need. Specifically, we show that O K-edge RIXS can access multi-spinon excitations, antiholon excitations, and combinations thereof, thus providing a unique view of spin-charge separation in doped 1D AFMs. Since Sr_2CuO_3 can be doped with Zn, Ni, or Co [53, 54], this material can be used to test our predictions.

Moreover, we expect our results to be valid for other 1D doped antiferromagnets, such as Ca_2CuO_3 and $SrCuO_2$, and are not just restricted to Sr_2CuO_3.

Magnetic Scattering at the O K-edge — Before proceeding, we review how magnetic excitations occur in the O K-edge ($1s \to 2p$) [75] measurements on Sr_2CuO_3, as sketched in Fig. 4.1(a). Sr_2CuO_3 is a charge-transfer insulator and the ground state character of the CuO_4 plaquettes is predominantly of the form $\alpha|d^9\rangle + \beta|d^{10}\underline{\mathrm{L}}\rangle$ ($\alpha^2 \approx 0.64$, $\beta^2 \approx 0.36$) [43, 46], due to hybridization between the Cu $3d_{x^2-y^2}$ and O $2p$ orbitals. Here, $\underline{\mathrm{L}}$ denotes a hole on the ligand O orbitals. Due to this hybridization, the incident photon can excite an O $1s$ core electron into the Cu $3d$ orbital when tuned to the O K-edge, creating an upper Hubbard band excitation. In the intermediate state, the d^{10} configuration can move to the neighboring Cu ion via the bridging O orbital. Since the adjacent Cu orbital also hybridizes with the O containing the core hole, one of the d^{10} electrons can then decay to fill it, creating a final state with a double spin flip.

The dynamics in the intermediate state are essential for generating magnetic excitations at this edge, and this is a fundamental difference in how RIXS and INS probe magnetic excitations. One of the advantages of working at the O K-edge is that it has relatively long core-hole lifetimes ($\hbar/\Gamma_n$, $\Gamma_n = 0.15$ eV [131]) in comparison to other edges ($\Gamma_n = 1.5$ eV at the Cu K-edge and 0.3 eV at the Cu L_3-edge [132]), which provides a longer window for generating magnetic excitations [57, 133]. Because of this, inclusion of the intermediate states in the modeling is necessary. Several efforts addressing the spin dynamics in RIXS have mostly used the *ultrashort core-hole lifetime* (UCL) approximations, which applies to edges with short core-hole lifetimes [122, 134], while studies of 1D systems beyond UCL approximations have been limited [90, 132]. Ref. [90] studied the effect of incidence energy on spin dynamics RIXS spectra in 1D using small cluster ED, but a systematic analysis of the incident energy dependence was not carried out. As a result, the multi-spinon excitations at $q = 0$ were not reported. Similarly, Ref. [88] discussed the doping dependence of the RIXS spectrum for the t-J model by evaluating the spin response,

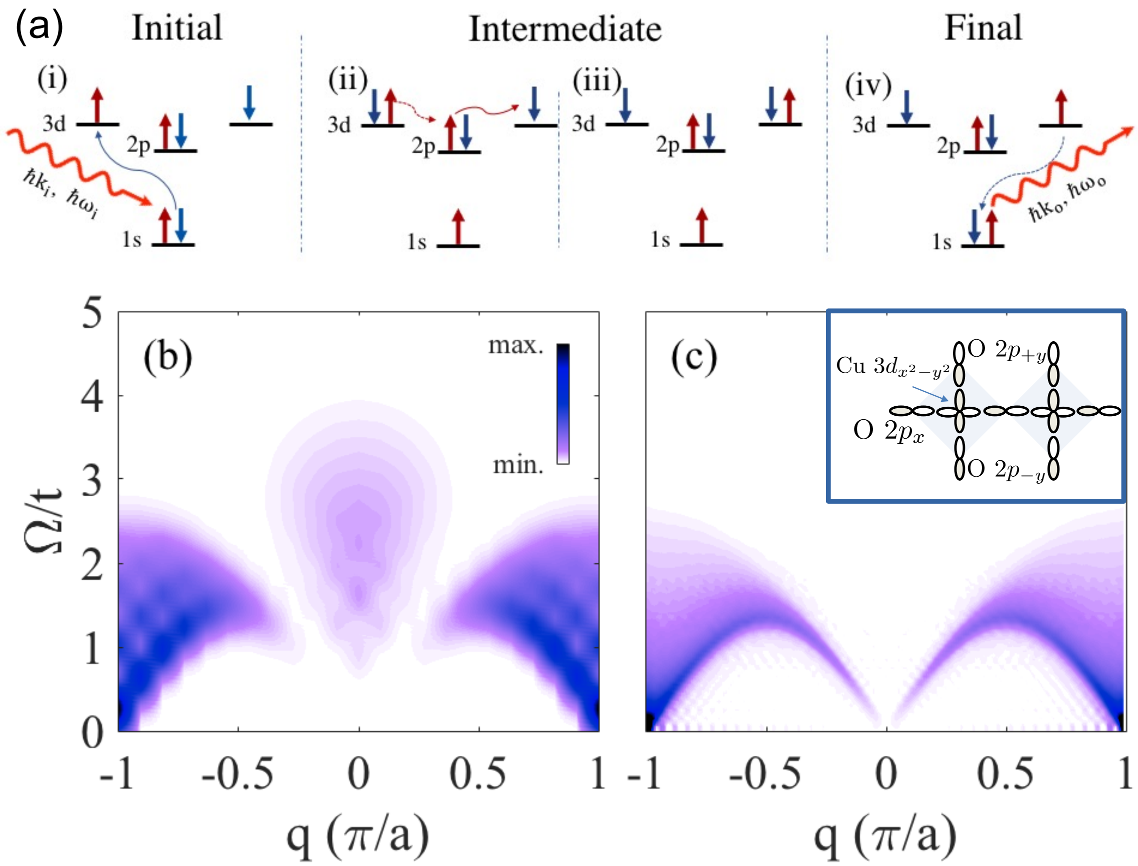

Figure 4.1: a) A sketch of the spin-flip mechanism in oxygen K-edge RIXS. Hybridization between the Cu and O orbitals allows an incident photon to excite an O 1s electron into the $3d_{x^2-y^2}$ orbital on one of the two neighboring Cu sites, creating a Cu d^{10} upper Hubbard band excitation in the intermediate state (subpanel i). The d^{10} excitation can transfer to the other neighboring Cu site via two Cu-O hopping processes [(subpanel ii) & (subpanel iii)]. Finally, the extra electron decays back into the O 1s core level, leaving the system in a final state with a double spin-flip (subpanel iv). The inset in panel c) shows the CuO$_4$ plaquettes of Sr$_2$CuO$_3$ in which only the bridging oxygen participates in the spin-flip process. b) The computed RIXS spectra for an undoped t-J model on a 22-site chain. c) $S(q,\omega)$ for an undoped 80-site chain, calculated with DMRG for the same model. Note the additional spectral weight in the RIXS intensity centered at $q=0$, and absent in $S(q,\omega)$.

but the charge response along with the intermediate state dynamics were left out. For these reasons, the prior studies could not address the physics reported here.

4.2 Model and methods

Sr_2CuO_3 is a multiorbital system, and a multiorbital Hamiltonian should be employed if one wishes to capture the RIXS spectra at all energies. However, our focus here is on the low-energy magnetic and charge excitations that arise from quasiparticle fractionalization. Prior work at the Cu L-edge showed that the dd- and charge-transfer excitations in Sr_2CuO_3 appear at higher energy losses ($\Omega > 1.5$ eV) [5]. Based on this observation, we work with an effective 1D t-J model, where these interorbital excitations have been integrated out, with the caveat that we will restrict ourselves to energy losses below 1.2 eV (*i.e.* $4t$). The fact that this same model accurately captures the low-energy the magnetic excitations observed in undoped Sr_2CuO_3 [57], provides further support for this approach. The model Hamiltonian is

$$H = -t\sum_{i,\sigma}(\tilde{d}^{\dagger}_{i,\sigma}\tilde{d}_{i+1,\sigma} + h.c.) + J\sum_{i}(\mathbf{S}_i \cdot \mathbf{S}_{i+1} - \frac{1}{4}n_i n_{i+1}).$$

Here, $\tilde{d}_{i,\sigma}$ is the annihilation operator for a hole with spin σ at site i, under the constraint of no double occupancy, $n_i = \sum_\sigma n_{i,\sigma}$ is the number operator, and $\mathbf{S}_i$ is the spin operator at site i.

During the RIXS process [1], an incident photon with momentum $\mathbf{k}_{\text{in}}$ and energy ω_{in} ($\hbar = 1$) tuned to an elemental absorption edge resonantly excites a core electron into an unoccupied state in the sample. The resulting core hole and excited electron interact with the system creating several elementary excitations before an electron radiatively decays into the core level, emitting a photon with energy ω_{out} and momentum $\mathbf{k}_{\text{out}}$. The RIXS intensity is given by the Kramers-Heisenberg formula [1]

$$I = \sum_f \left| \sum_n \frac{\langle f|D^\dagger|n\rangle\langle n|D|i\rangle}{E_i + \omega_{\text{in}} - E_n + i\Gamma_n} \right|^2 \delta(E_f - E_i - \Omega), \tag{4.1}$$

where $\Omega = \omega_{\text{in}} - \omega_{\text{out}}$ is the energy loss, $|i\rangle$, $|n\rangle$, and $|f\rangle$ are the initial, intermediate, and final states of the RIXS process with energies E_i, E_n, and E_f, respectively, and D is the dipole operator for the O $1s \to 2p$ transition. In the downfolded t-J model D takes on the effective form

$$D = \sum_{i,\sigma} e^{i\mathbf{k}_{\text{in}}\cdot(\mathbf{R}_i + \mathbf{a}\hat{\mathbf{x}}/2)} \left[\left(\tilde{d}_{i,\sigma} - \tilde{d}_{i+1,\sigma} \right) s^\dagger_{i+\frac{1}{2},\sigma} + h.c. \right], \tag{4.2}$$

where $\mathbf{q}$ $(= \mathbf{k}_{\text{out}} - \mathbf{k}_{\text{in}})$ is the momentum transfer and the relative sign is due to the phases of the Cu $3d_{x^2-y^2}$ and O $2p_x$ orbital overlaps along the chain direction. Here, $s_{i+\frac{1}{2},\sigma}$ is the hole annihilation operator for the $1s$ core level on the O atom bridging the i and $i+1$ Cu sites.

The x-ray absorption scattering (XAS) spectra is given by

$$I_{XAS} = \sum_n \left| \langle n|D|i\rangle \right|^2 \delta(E_n - E_g - \omega_{\text{in}}). \tag{4.3}$$

At the oxygen K-edge, the evaluation of XAS spectra, prior to RIXS calculation is important to get the appropriate ω_{in}. The dependence of the RIXS spectra on incident energy is discussed in section 4.3.2.

In the real material, the core hole potential raises the on-site energy of the bridging oxygen orbital (in hole language) in the intermediate state while exerting a minimal influence on the Cu sites. This change locally modifies the superexchange interaction between the neighboring Cu atoms [135]. To account for this effect, we reduce the value of $J_{i,i+1} = J/2$ when solving for the intermediate states, where the core-hole is created on the O atom bridging the i and $i+1$ sites. Our results are not sensitive to reasonable changes in this value, as shown in Sec. 4.3.2.

Throughout we set $t = 1$ as our unit of energy ($t \approx 300$ meV in Sr_2CuO_3). The remaining parameters are $\Gamma_n = \frac{1}{2}t$ for all n and $J = \frac{5}{6}t$, unless otherwise stated. These values are typical for the O K-edge measurements of Sr_2CuO_3. The *superexchange* J for Sr_2CuO_3 was reported to be around 250 meV by prior INS and RIXS studies [5, 46, 57]. For Sr_2CuO_3 and closely related 1D cuprate $SrCuO_2$, the hopping t was reported to be 300-600 meV [22, 23, 48, 57, 136]. Also, as discussed in Sec. 4.3.2, our calculated spectra do not change qualitatively in the range of reported values of t. The inverse core-hole lifetime Γ_n for the oxygen K-edge is 150 meV [131]. We also introduce a Gaussian broadening ($\Gamma = \frac{1}{3}t$) for energy conserving δ-function appearing in Eq. (4.1). We evaluated Eq. (4.1) on a $L = 20$ site chain using the Lanczos method with a fixed filling.

To help identify the relevant charge and spin excitations in the RIXS spectra, we also performed DMRG simulations [85, 86] for the dynamical charge $N(q,\omega)$ and spin $S(q,\omega)$ structure factors on an $L = 80$ site chain, and using correction-vector method [137, 138]. Within the correction vector approach, we used the Krylov decomposition [139] instead of the conjugate gradient. In the ground state and dynamic DMRG simulations, we used a maximum of $m = 1000$ states, keeping the truncation error below 10^{-8} and used a broadening of the correction-vector calculation of $\eta = 0.08t$. The computer package DMRG++ developed by G. Alvarez, CNMS, ORNL, was used for the DMRG simulations [140].

4.3 Results

4.3.1 Undoped RIXS spectra

Figure 4.1(b) shows the RIXS intensity for the half-filled t-J chain, reproduced from Ref. [57]. For comparison, Fig. 4.1(c) shows $S(q,\omega)$ obtained using DMRG for the same parameters. The RIXS intensity has two main features. The first is a continuum of excitations that closely mirrors $S(q,\omega)$ and is situated within the boundaries of the

2S continuum. Its intensity is relatively independent of the incident photon energy and is associated primarily with 2S excitations [57, 141]. The second feature is a continuum of excitations laying outside of the 2S continuum, corresponding to 4S excitations. As discussed in Chapter 3, intensity is sensitive to both the incident photon energy and the core-hole lifetime, indicating that the intermediate state plays a critical role in creating those excitations [57].

4.3.2 Doped RIXS spectra

We now turn our attention to the results for the doped case. Figures 4.2(a) and 4.2(b) show the RIXS intensity obtained on a 20-site chain at 5% and 10% electron doping, respectively. Here, we have used $\omega_{\text{in}} = 3t$ to enhance the intensity of the features appearing at $q = 0$. To help us better understand the main features, we also computed $S(q, \omega)$ [Fig. 4.3(a)] and $N(q, \omega)$ [Fig. 4.3(b)] for 5% doping using DMRG.

The RIXS spectra for the doped cases have three recognizable sets of features: i) a continuum that mirrors the $S(q, \omega)$ in Fig. 4.3(a); ii) a cosine-like dispersive feature with a bandwidth of $4t$ that mirrors $N(q, \omega)$ in Fig. 4.3(b); and iii) two continua, centered at $q = 0$ and extending up to $\sim 6t$ in energy loss. These features are absent in $S(q, \omega)$ and $N(q, \omega)$. The excitations (i) and (ii) point to a manifestation of spin-charge separation in that the response *bifurcates* into primarily two-spinon (i) and antiholon (ii) excitations, characterized by different energy scales. Also, notice that the dispersions of various peaks in Figs. 4.2(a) and 4.2(b) do not vary significantly with a small change in doping, except for their relative intensities. It is important to note that the RIXS and $N(q, \omega)$ are response functions that probe excitations with net charge zero, and one would expect to see a holon-antiholon continuum [142]. However, for small electron doping, the holon-antiholon continuum appears effectively as a single antiholon excitation band due to phase space constraints in the holon scattering. For larger electron dopings, we expect to see a distinct holon-antiholon continuum in both RIXS and $N(q, \omega)$.

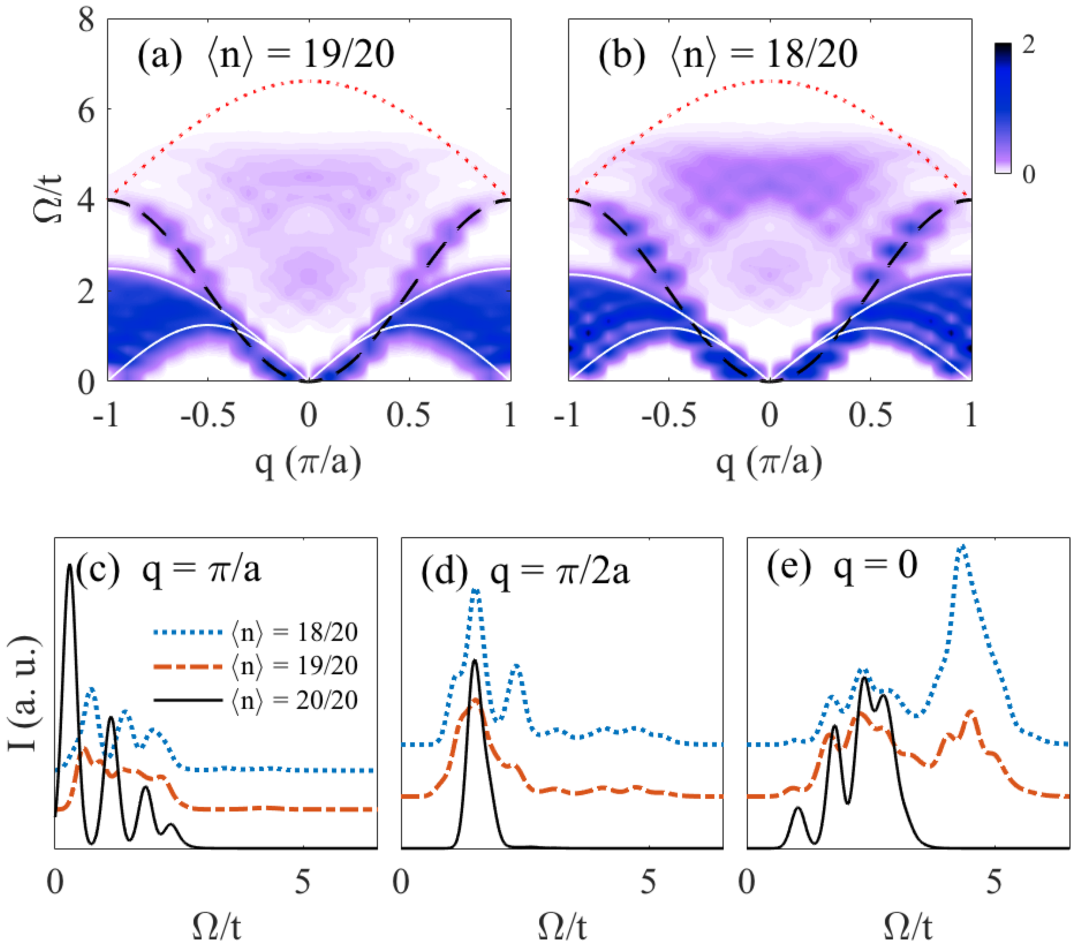

Figure 4.2: Calculated RIXS spectra at $\omega_{\rm in} = 3t$ for an $L = 20$ sites doped t-J chain with (a) one and (b) two additional doped electrons. The white, black, and red lines shows the boundaries for two-spinon continuum, the dispersion of the antiholonic excitation, and upper boundary for antiholon-2S excitations, respectively. Panels (c), (d), and (e) compare the doped RIXS spectra with the undoped case for momentum transfers of $q = \pi/a$, $q = \pi/(2a)$, and $q = 0$, respectively.

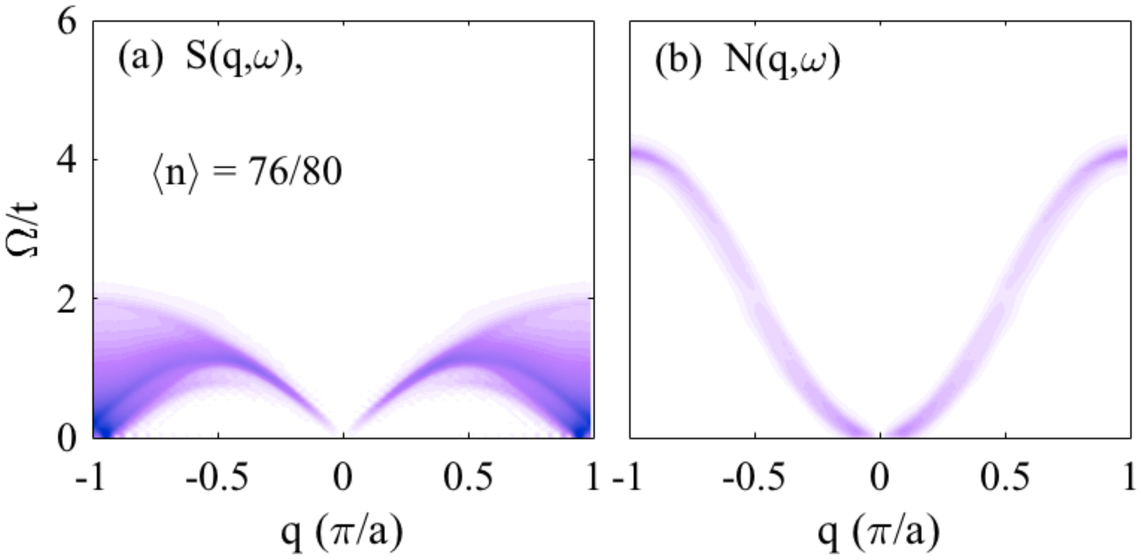

Figure 4.3: DMRG results for (a) $S(q,\omega)$ and (b) $N(q,\omega)$ for the doped t-J model on an L = 80 sites chain and $\langle n \rangle = 0.95$ doping.

Figures 4.2(c)-4.2(e) compare the doping evolution of the RIXS features at fixed momentum points. Fig. 4.2(c) shows $q = \pi/a$, where the upper bound (πJ) of the spin excitations decreases upon doping. Similarly, the line-cut at $q = \pi/2a$ in 4.2(d) shows that the lower bound ($\pi J/2$) of the 2S continuum also decreases with doping, allowing for final states below the 2S continuum of the undoped case. We also observe a secondary feature at higher energy loss due to changes in the holon branch and 4S excitations. Fig. 4.2(e) shows a cut at $q = 0$, where two distinct sets of peaks are clear. The group at lower energy losses appears in the same energy range of the multi-spinon peak observed in the undoped case. The peaks at higher energy loss appear above $\Omega = 4t$ and are identified below. Also, panels (c)-(e) illustrate that the RIXS intensity of spin excitations 2S and 4S is suppressed upon doping, resulting in a much broader spectral features. Conversely, the antiholonic features, absent in the undoped case, are enhanced as doping is increased.

The calculated spectra can be understood by making use of the spin-charge separation picture: in 1D, the wavefunction of the large U Hubbard model for N

electrons in L lattice sites is a product of 'spinless' charge and 'chargeless' spin wavefunctions [143, 144, 145]. The dispersion of charge excitations is given by $\omega_{\bar{h}}(k_{\bar{h}}) = 2t[1 - \cos(k_{\bar{h}}a)]$ [146, 147], which agrees well with the dispersion observed for feature (ii) (see black dashed line) and in $N(q,\omega)$. As shown in the Sec. 4.3.2, the $N(q,\omega)$ computed here for small *electron doping* is identical to the $N(q,\omega)$ obtained for a 1D spinless fermions chain with the same *fermionic filling*, supporting the spin-charge separation picture. This result indicates that the charge excitation is behaving like a nearly free spinless quasiparticle, i.e. a holon/antiholon. Concerning the spin part, the dispersion relation for a single spinon is given by $\omega_s(k_s) = \frac{\pi}{2}J|\sin(k_s a)|$. Due to the RIXS matrix elements, these spin excitations must be generated in even numbers, resulting in a continuum whose boundaries are defined by this dispersion relation. At small doping, the limits of this continuum are modified, which is accounted for using a slightly modified superexchange $\tilde{J} = J\langle n\rangle$ [145]. The upper and lower boundaries of the modified 2S continuum are indicated by the white lines in Fig. 4.2 and agree well with the observed excitations.

We can summarize the picture emerging from our results as follows: the 2S-like continuum present in the RIXS spectrum is a pure magnetic excitation as it compares well with the $S(q,\omega)$ from DMRG. The dispersing cosine-like feature in the doped RIXS spectra compares well with the $N(q,\omega)$ from DMRG. We have verified that the $N(q,\omega)$ of the spinless fermions with occupations equal to the electron-doping considered above are qualitatively similar to the results obtained for the doped t-J chain as discussed in Sec. 4.3.2. We therefore assign this feature to purely charge-like antiholon excitations.

The peaks at $q = 0$ of the RIXS spectrum are not captured by either $S(q,\omega)$ or $N(q,\omega)$. The lower continuum resembles the multi-spinon continuum [57] also observed in the undoped case, and we, therefore, associate it with 4S excitations. Conversely, the continuum of excitations at energy losses between $4t$ and $6.5t$ (well beyond the upper boundary of 4S continuum [$2\pi J$ ($= 5.24t$)] [111]) is unique to the doped case. The excitations are bounded by $4t + \pi J\cos(q/2a)$ (dotted red line), which one obtains from a simple convolution of the antiholon and two-spinon excitations. Therefore, we assign these to an antiholon plus two-spinon final state. The fact that the intensity and distribution of these excitations are very sensitive to doping supports this view. As we further increase the doping, we see additional spectral weight above the $4t + \pi J \cos(q/2a)$ boundary, indicating that these quasiparticle excitations are beginning to interact to produce modified dispersion relationships.

Incidence energy dependence

We now explore dependence of the RIXS spectra on incident energy considering two values of doping. Figs. 4.4 and 4.5 show the changes in RIXS intensity maps as the incident photon energy is varied from $\omega_{\text{in}} = -t$ to $4t$ for the 5% and 10% dopings, respectively. The final state excitations resembling $S(q, \omega)$ and $N(q, \omega)$ are clear in all cases, but there are some variations in the overall intensity as ω_{in} is tuned through the XAS resonance peak (Figs. 4.4a and 4.5a, inset). The remaining excitations exhibit a strong incident energy dependence, where both antiholon excitations and the multi-spinon/antiholon excitations centered at $q = 0$ are difficult to resolve for $\omega_{\text{in}} \notin [-t,\ 4t]$.

By varying ω_{in}, one selects particular intermediate states $|n\rangle$ in the RIXS process. The incident energy dependence shown in Figs. 4.4 and 4.5 indicate that only certain intermediate states can reach the multi-particle excitations centered at $q = 0$. The comparison of Fig. 4.5 with Fig. 4.4 shows that the antiholonic features become more robust whereas the spin excitations are relatively unaffected at each incident energies on increased doping in the 1D chain.

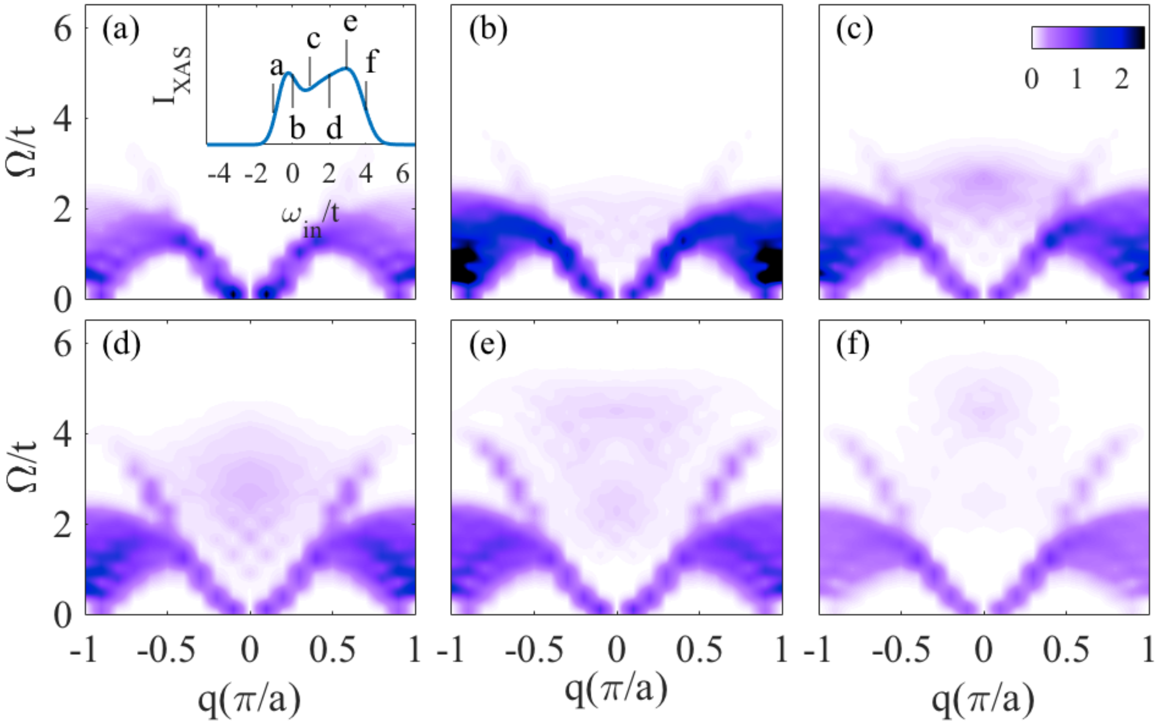

Figure 4.4: The dependence of RIXS spectra on the incident photon energy ω_{in} for a 5% doped 20-site chain, evaluated using the full Kramers-Heisenberg formalism. The inset of panel (a) shows the XAS spectrum from the model, along with the incident energies used in each of the RIXS calculations.

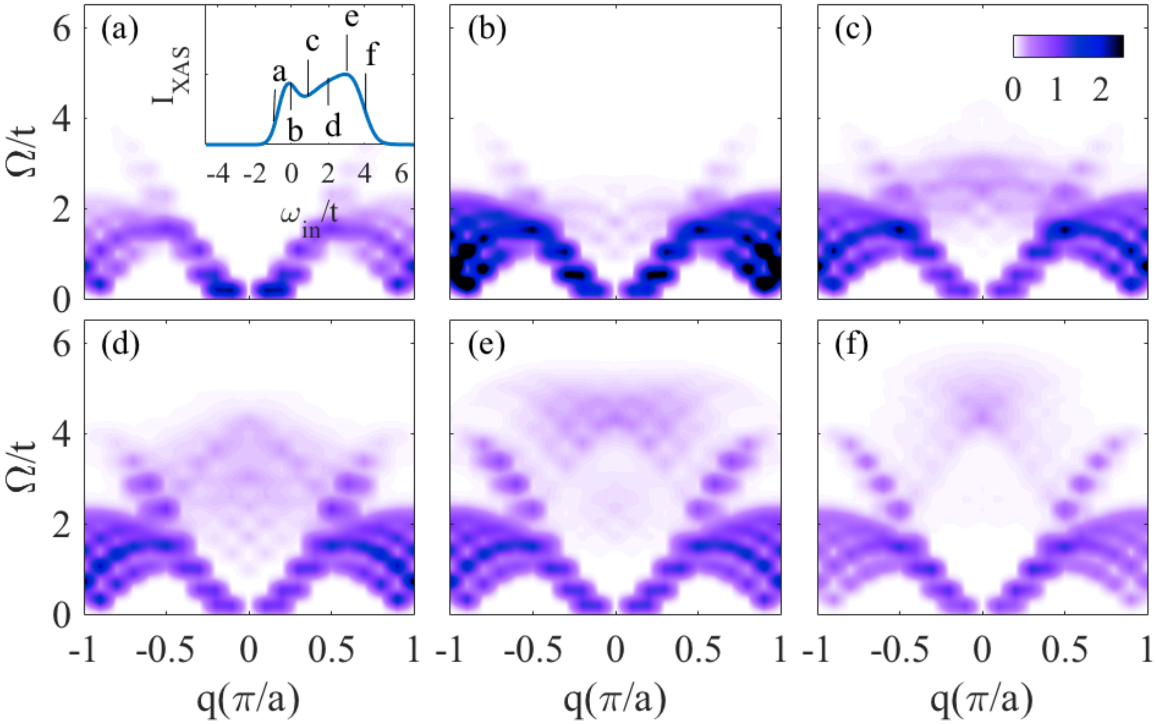

Figure 4.5: Dependence of RIXS spectra on the incident photon energy ω_{in} for a 10% doped $L = 20$ site chain. The inset of panel (a) shows the XAS spectrum of the same system, along with the incident energies used in each of the RIXS calculations.

Effect of hopping parameter on the RIXS spectra

In this section, we discuss dependence of the RIXS spectra on the hopping parameter t for a fixed J. This analysis helps us further clarify the spin- and charge-like nature of the excitations observed in the RIXS spectra. Fig. 4.6 shows two set of excitations: The *first* are purely magnetic excitations, which are insensitive to hopping parameter. In this case, the 2S excitations highlighted by the red solid lines overlay is completely driven by the *superexchange* coupling (J). The 4S excitation continuum upper boundary is highlighted by red dotted line. Note that in panels (c) and (d), the 4S continuum is not visible due to our choice of incident energy ω_{in}. In panel (a), the $q = \pi/a$ excitations vanish at $t = 0$. This behavior has also been obtained in Ref. [90]. The *second* set of excitations are the antiholonic excitations whose dispersion are governed by the hopping amplitude and have a bandwidth of $4t$. Additionally, an antiholon plus two-spinon continuum ($\bar{h}2S$) is characterized by both the J and t parameters. Indeed, the upper boundary of these excitations is given by $[4t + \pi J \cos(q/a2)]$. As t is changed, the RIXS spectra evolves as expected.

$\mathbf{N(q}, \omega)$ of a spinless chain and electron-doped $t - J$ model

We study the dynamical charge structure factor $N(q, \omega)$ of a $t - J$ chain [148] at small electron *doping*, which is similar to the spectrum of a spinless fermion 1D chain with the *same* small fermionic *filling*.

The $N(q, \omega)$ of a 1D non-interacting spinless fermion chain is given by

$$N(q, \omega) = \sum_{i,j} e^{iq(R_i - R_j)} \langle \psi_g | \hat{n}_j \frac{1}{\omega - \hat{H} + E_{gs} + i\eta} \hat{n}_i | \psi_g \rangle, \tag{4.4}$$

where $\hat{n}_i = \hat{c}_i^\dagger \hat{c}_i$ is the fermionic density operator on site i, and η indicates the spectral peaks' broadening. We also denote the ground state as $|\psi_g\rangle = \prod_{|k| \leq k_F} \hat{c}_k^\dagger |0\rangle$ with energy E_{gs}, and Fermi momentum $k_F = \pi n$, where $n = N/L$ is the fermionic filling. Focusing

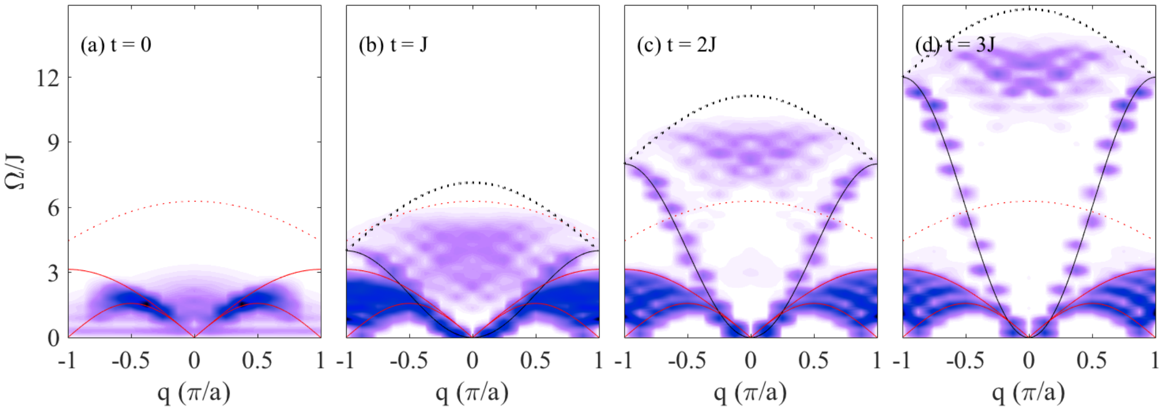

Figure 4.6: Dependence of the RIXS spectra on the hopping parameter t for an $L = 16$ site doped $t - J$ chain with $\langle n \rangle = 0.94$ doping. The incidence energy, $\omega_{\text{in}} = 1.8J$, $3.4J$, $5.6J$ and $7J$ for (a), (b), (c) and (d) panel, respectively. We have chosen these values of the incident energy to highlight the $\bar{h}2S$ continuum portion (absent in $t = 0$ case) of the RIXS spectrum. The spin parts shown with red overlays are insensitive to the hopping, whereas the parts involving antiholon shown with black overlays are directly dependent on the hopping parameter t. Solid and dotted (red) lines report the boundaries of the 2S and 4S continuum, while the solid and dotted (black) show the dispersion of antiholon excitations and upper boundary of antiholon-2S continuum.

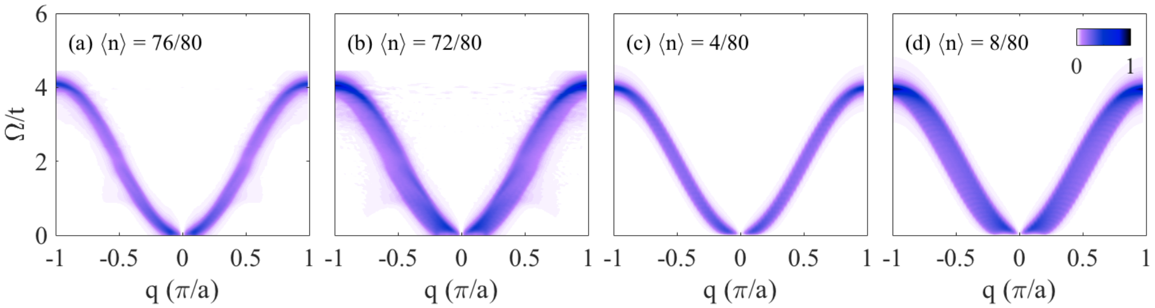

Figure 4.7: Panels (a) and (b) report the $N(q,\omega)$ for 1D $t-J$ chain with $L=80$ sites calculated using DMRG at 5% and 10% doping, respectively. Panels (c) and (d) report the $N(q,\omega)$ for *spinless*-fermion 1D chain with $L=80$ sites computed analytically at 5% and 10% fermionic fillings, respectively.

on the $q \neq 0$ part, one finds

$$N(q,\omega) = \frac{1}{L}\sum_{k}\frac{\theta(|k| \leq k_F)\theta(|k+q| > k_F)}{\omega - \epsilon_{k+q} + \epsilon_k + i\eta}, \tag{4.5}$$

where $\epsilon_k = -2t\cos(k)$ is the dispersion relation for free fermions.

Fig. 4.7 shows explicitly that the $N(q,\omega)$ of the $t-J$ chain at 5% and 10% electron doping computed with DMRG is qualitatively very similar to the results obtained for a spinless fermion chain ($L=80$ sites) with 5% and 10% fermionic fillings, respectively.

Effect of J_{ch} at core-hole site on the RIXS spectra

We explore the dependence of RIXS spectra on the value of superexchange interaction J_{ch} in the vicinity of the core-hole. Fig. 4.8 confirms that the RIXS spectra, at fixed incident energy, do not depend on J_{ch} qualitatively.

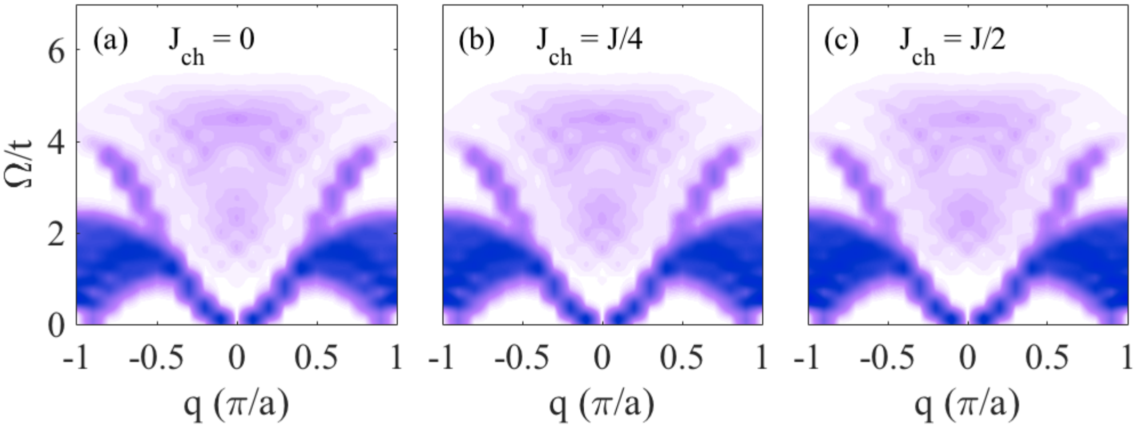

Figure 4.8: RIXS spectra for different J_{ch} values used in the RIXS intermediate state, with incident energy ω_{in} $(= 3t)$.

4.4 Discussion

Several previous theoretical works have calculated the RIXS spectra for 1D t-J [122, 134] and Hubbard [90, 132] chains using the same formalism. In the doped and undoped cases, these studies obtained RIXS spectra resembling $S(q, \omega)$; however, they did not capture the (anti)holon or multi-spinon excitations observed here. Refs. [90] and [134], obtained nonzero weight in the $q = 0$ response but with a significantly reduced spectral weight in comparison to our results. In RIXS at oxygen K-edge, only $\Delta S = 0$ excitations are allowed. Refs. [90] and [132] showed that $\Delta S = 0$ excitations vanishes at $q = \pi/a$, whereas we have the maximum at that point in our model. We believe that this discrepancy is due to the lack of hopping from the core-hole site due to the strong core-hole potential used in that work, which is appropriate for the Cu L and K-edges. A strong core-hole potential will tend to localize the excited electrons in the intermediate state, thus suppressing its dynamics. We can confirm this in our model by setting $t = 0$ in the intermediate state for the undoped system, which also prohibits charge fluctuations and produces spectra similar to Refs. [90] and [132]. Furthermore, given the sensitivity to ω_{in} as discussed in section 4.3.2, prior studies may have missed the relevant excitations due to their choice of incident energies.

In RIXS experiment, we expect a uniform modulation of all the excitations in the RIXS intensity given by the angular dependence of the bridging oxygen p_x-orbital [57]. At the oxygen K-edge, the 2S, 4S and antiholon excitations are $\Delta S = 0$ excitations without any polarization dependence and hence, one cannot use it to disentangle these excitations. However, 2S and 4S can be disentangled from the antiholonic excitations by making use of the differences in doping dependence of these excitations. One expects that the 2S and 4S will be suppressed upon doping. Instead, the antiholonic features absent in the undoped case, will be enhanced on increased doping.

4.5 Conclusions

In this chapter, we have shown that spin-charge separation can be observed in O K-edge RIXS on doped 1D-AFMs and that these systems exhibit remarkably rich spectra consisting of multi-spinon and holon excitations. Our results highlight the potential for RIXS to simultaneously access the charge, spin, and orbital degrees of freedom in fractionalized quasiparticle excitations, applicable to many quantum materials. Our work provides strong motivation for RIXS experiments at the oxgen K-edge of doped 1D antiferromagnets. The recent RIXS experiment at the O K-edge of undoped Sr_2CuO_3 [57] and the availability of doped Sr_2CuO_3 and $SrCuO_2$ crystals [53, 54, 149] give us confidence that our predictions can be verified experimentally in the near future.

Chapter 5

Systematic study of spin and charge dynamics in two-leg spin ladders probed by resonant inelastic x-ray scattering

This chapter is a modified version of U. Kumar, *et al.*, Phys. Rev. B **99**, 205130 (2019) [150].

5.1 Introduction

In this chapter, we explore the spin and charge dynamics of spin-ladder antiferromagnets. Strongly correlated spin ladders are excellent platforms for studying quantum many-body phenomena, such as high critical temperature (high-T_c) superconductivity [151] and spinon confinement [70]. Quantum ladders are intermediate between one- and two-dimensional materials, and their study allows for detailed comparisons between theoretical models and experimental probes [2, 5, 41, 42, 57, 58, 59, 60, 61, 62, 63, 64, 65, 66, 67, 68, 69, 70, 71]. The discovery of superconductivity in the ladder "telephone number" compound $Sr_{0.4}Ca_{13.6}Cu_{24}O_{41.84}$ [19], which had been theoretically predicted [72], created new opportunities to study the relationships between lattice, orbital, charge, and magnetic degrees of freedom and unconventional superconductivity in copper-oxide materials. Accordingly, a significant effort has been launched to understand the magnetic excitation spectrum of materials hosting quantum ladders and its connection to superconductivity. For example, inelastic neutron scattering (INS) studies have reported the observation of a spin gap in $Sr_{14}Cu_{24}O_{41}$ [42], triplon and two-triplon excitations in $La_4Sr_{10}Cu_{24}O_{41}$ [56], and spinon confinement in $CaCu_2O_3$ [70].

With continued improvements in instrumentation, resonant inelastic x-ray scattering (RIXS) is being increasingly employed to study collective magnetic excitations [2, 3, 4, 5, 28, 30, 33, 34, 57, 114]. RIXS is complementary to INS in that the scattering processes allows for both $\Delta S = 0$ and $\Delta S = 1$ excitations, depending on the elemental edge [29, 114], the strength of the spin-orbit coupling in the core level [29], and the local crystal stucture of the material [123]. As such, the technique accesses many magnetic excitations including magnons [4, 28, 30, 33, 34] and bimagnons in two-dimensional (2D) cuprates [114, 152], and multi-spinon excitations in one-dimensional (1D) cuprates [57, 88, 90, 97]. RIXS also provided surprising results for 2D cuprates, where the paramagnon excitations are found to persist deep into the overdoped region of the phase diagram [4, 30, 32, 33, 34]. Recently, an electron-hole asymmetry in the doping dependence of the spin excitations of 2D cuprates was reported, as well as an additional collective charge excitation in the electron-doped case that is absent in the hole-doped case [28].

The rich variety of excitations observed in 1D and 2D cuprates described above, and their possible connection to unconventional superconductivity, provides a strong motivation for exploring the RIXS spectra of two-leg spin ladders, both as a function of the rung coupling and doping. Such studies provide information not only about magnetic excitations but also about potentially cooperative/competing charge, orbital, and lattice excitations. Early RIXS Cu K-edge experiments on the telephone number compounds focused primarily on the high-energy charge excitations across the Mott gap [153, 154, 155]. Later, as the instrumental resolution improved, studies started addressing low-energy magnetic excitations. For example, the magnetic response of $Sr_{14}Cu_{24}O_{41}$ at the Cu L_3-edge was measured [2] and interpreted in terms of the lower boundaries of a two-triplon continuum. Another Cu L_3-edge study on $CaCu_2O_3$ – a weakly coupled spin-ladder system – showed that the spectra could be decomposed into contributions from the spin-conserving (SC) and non-spin-conserving (NSC) channels [74]. Subsequent work at the same edge on the same material focused on spin-orbital fractionalization, but did not carry out an analysis of spinon confinement [73].

From a theoretical perspective, studies of the RIXS response of spin ladders have mainly focused on undoped systems using a projector method [59] or exact diagonalization (ED) of small (4×2) Hubbard clusters [2], and were restricted to a limited set of rung couplings. To our knowledge, no systematic RIXS study of the low-energy excitations of doped and undoped ladders has been carried out. Here, we present such a study. Specifically, we use the Kramers-Heisenberg formalism to compute the RIXS response of undoped and doped two-leg t-J ladders while varying the superexchange coupling along the rungs over a wide range of values. The RIXS intensity is evaluated numerically, exactly or with a very small error, using ED and the density matrix renormalization group (DMRG) [84, 156, 157] methods. Using these tools, we investigate the charge and magnetic excitations in both the SC and NSC channels and catalog an assortment of quasiparticle and collective excitations. The present systematic study can guide future RIXS experiments and help to classify compounds as being in the weak- or strong-rung coupling regime, depending on the observed excitations.

Iridates are another group of spin-$\frac{1}{2}$ ($J_{\text{eff}} = \frac{1}{2}$) materials that have been studied with RIXS [6, 7, 8, 9]. Moreover, progress was recently made in engineering quasi-1D iridates in heterostructures [158], establishing another platform for examining and controlling the properties of quantum spin ladders. The results presented here can serve as a valuable roadmap in these contexts as well.

Our organization in this chapter is as follows: Section 5.2 introduces the spin ladder model and the relevant scattering cross-sections for RIXS within the Kramers-Heisenberg formalism. Sections 5.3.1 and 5.3.2 present results for the RIXS spectra in the NSC and SC channels, respectively. Section 5.3.3 reports effective correlation functions that can reproduce the RIXS spectra of NSC and SC channels. Section 5.3.4 revisits and discusses the RIXS data reported [2] on the spin-ladder compound $Sr_{14}Cu_{24}O_{41}$ in the context of our results. Finally, section 5.4 summarizes our findings.

5.2 Methods

5.2.1 Model Hamiltonian

We study the t-J model in a two-leg ladder geometry. The Hamiltonian is

$$\begin{aligned} H = J_{\text{rung}} \sum_{i} \left(\mathbf{S}_{i,0} \cdot \mathbf{S}_{i,1} - \tfrac{1}{4} n_{i,0} n_{i,1}\right) + J_{\text{leg}} \sum_{i,\tau} \left(\mathbf{S}_{i,\tau} \cdot \mathbf{S}_{i+1,\tau} - \tfrac{1}{4} n_{i,\tau} n_{i+1,\tau}\right) \\ + t_{\text{rung}} \sum_{i,\sigma} \left(c^{\dagger}_{i,0,\sigma} c_{i,1,\sigma} + \text{h.c.}\right) + t_{\text{leg}} \sum_{i,\tau,\sigma} \left(c^{\dagger}_{i,\tau,\sigma} c_{i+1,\tau,\sigma} + \text{h.c.}\right). \end{aligned} \tag{5.1}$$

Here, $\tau = 0,\ 1$ indexes the legs of the ladder while $i = 1, \ldots, L$ indexes the unit cell along each leg; $\mathbf{S}_{i,\tau}$ is a spin operator; $c_{i,\tau,\sigma}$ ($c^{\dagger}_{i,\tau,\sigma}$) annihilates (creates) a hole with spin σ ($=\uparrow,\downarrow$) at site (i,τ) subject to the constraint of no double occupancy; J_{leg} (J_{rung}) and t_{leg} (t_{rung}) are the superexchange and hopping integrals along the leg (rung) direction of the ladder, respectively; and $n_{i,\tau} = \sum_{\sigma} c^{\dagger}_{i,\tau,\sigma} c_{i,\tau,\sigma}$ is the hole number operator. Note that we neglected the ring-exchange terms in our model for simplicity.

The two-leg spin-ladder model can be used to describe several compounds, and a range of model parameters have been reported, as summarized in Table 5.1. The

Table 5.1: Different values of the exchange parameters (in units of meV) reported in the literature for various spin-$\frac{1}{2}$ ladder systems. Entries where the value of J_{ring} is missing correspond to studies where the ring exchange terms were not included in the analysis.

Material	J_{leg}	J_{rung}	J_{ring}	Experiment
$Sr_{14}Cu_{24}O_{41}$	130	72		INS [42].
	110	140		RIXS [2].
	110 ± 20	$4J_{\text{leg}}/5$		Raman [159].
	145	123		This work.
$La_4Sr_{10}Cu_{24}O_{41}$	186	124	31	INS [56].
$La_6Ca_8Cu_{24}O_{41}$	110	110	16.5	INS [64].
$CaCu_2O_3$	134	11		RIXS [73].

parameters can be different even for the same compound depending on the nature of the experiment or model used to analyze the data. Due to the variability in the reported couplings, we opted to carry out a systematic study over a range of rung parameters spanning from *weak* to *strong* rung couplings. Unless otherwise stated, we adopt the specific couplings (in units of meV) $J_{\text{leg}} = 140$, $J_{\text{rung}} = 140r$, $t_{\text{leg}} = -300$, and $t_{\text{rung}} = -300\sqrt{r}$, where $r = \frac{J_{\text{rung}}}{J_{\text{leg}}}$ is a parameter used to adjust the ratio of the rung-leg couplings. The choice $t_{\text{rung}} = -300\sqrt{r}$ preserves the relationship $J_{\text{rung}} \propto \frac{t^2_{\text{rung}}}{U}$, assuming a fixed value of U.

5.2.2 RIXS Intensity

We evaluated the RIXS response at the Cu L-edge of cuprate materials. In a RIXS experiment, photons with energy ω_{in} and momentum $\mathbf{k}_{\text{in}}$ ($\hbar = 1$) scatter inelastically from a sample, transferring momentum $\mathbf{q} = \mathbf{k}_{\text{out}} - \mathbf{k}_{\text{in}}$ and energy $\omega = \omega_{\text{out}} - \omega_{\text{in}}$ to its elementary excitations. The RIXS spectrum is evaluated using the Kramers-Heisenberg formula [1] and is given by

$$\mathcal{I} = \sum_f \left| \frac{\langle f|\mathcal{D}^\dagger_{\mathbf{k}_{\text{out}}}|n\rangle\langle n|\mathcal{D}_{\mathbf{k}_{\text{in}}}|g\rangle}{E_g + \omega_{\text{in}} - E_n + \mathrm{i}\Gamma} \right|^2 \delta(E_f - E_g + \omega), \tag{5.2}$$

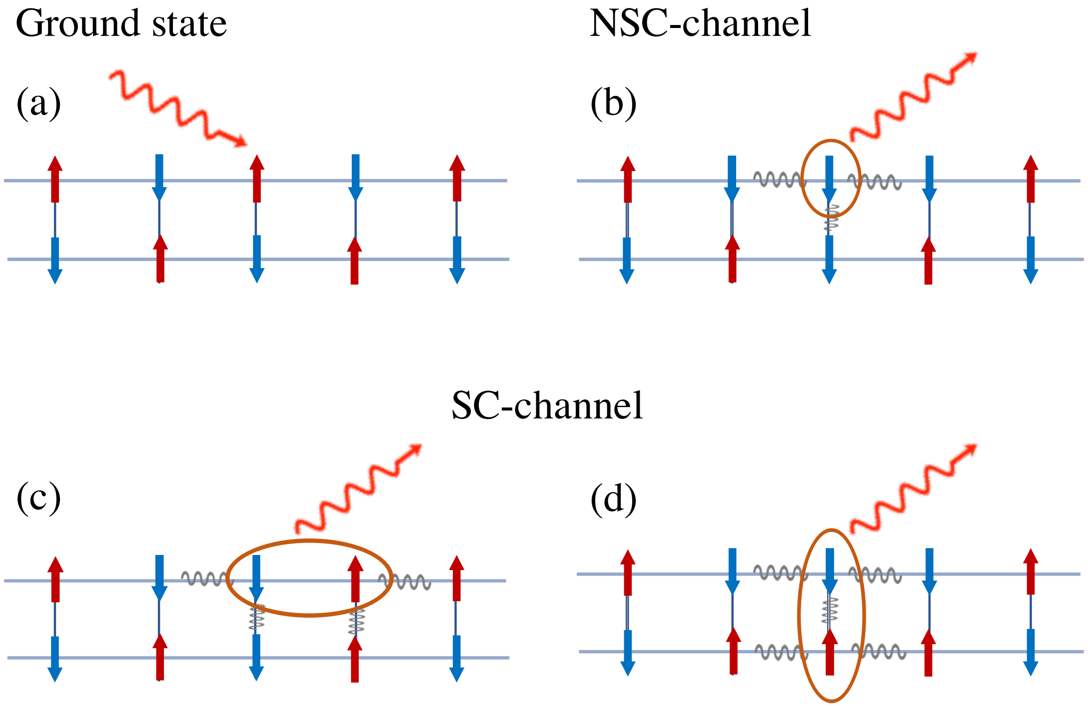

Figure 5.1: Schematic diagrams of the elementary magnetic excitations that are possible in spin-ladders. Panel (a) shows the ground state configuration of the spins with antiferromagnetic correlations. Panel (b) shows the single spin-flip excitations that appear in the non-spin-conserving (NSC) channel. Panels (c) and (d) show the double spin-flip processes relevant to the spin-conserving channel (SC). In each panel, the wiggly grey lines indicate "broken" magnetic bonds.

where $|g\rangle, |n\rangle$, and $|f\rangle$ are the ground, intermediate, and final states with energies E_g, E_n, and E_f, respectively, and Γ is the core-hole lifetime broadening. The eigenstates are obtained by diagonalizing $H + H_{\text{ch}}$, where $H_{\text{ch}} = V_c \sum_{i,\tau} n_{i,\tau} n^p_{i,\tau}$ accounts for the interaction between the valence and the core holes in the intermediate state. Here, V_c is the inter-orbital repulsion between the holes in the Cu $2p$ and $3d$ orbitals, $n^p_{i,\tau} = \sum_{m_J} p^\dagger_{i,\tau,m_J} p_{i,\tau,m_J}$, and $p^\dagger_{i,\tau,m_J}$ (p_{i,τ,m_J}) creates (annhilates) a hole in the $m_J = \pm\frac{3}{2}, \pm\frac{1}{2}$ ($m_J = \pm\frac{1}{2}$) states of the $J = \frac{3}{2}$ ($J = \frac{1}{2}$) manifold of the core level of site (i,τ) for L_3 (L_2)-edge. In the two-leg t-J ladder, the dipole operator is given by $\mathcal{D}_{\mathbf{k}} = \sum_{i,\tau,\sigma,m_J} e^{\mathrm{i}\mathbf{k}\cdot\mathbf{R}_{i,\tau}} [c_{i,\tau,\sigma} p^\dagger_{i,\tau,m_J} + \text{h.c.}]$, where we have neglected the prefactor that depends on the polarization of the photon and the scattering angle. Due to the large spin-orbit coupling in the core $2p$ orbital, both NSC ($\Delta S = 1$) and SC ($\Delta S = 0$) excitations can occur at this edge [74, 84, 90], and the RIXS spectra has contributions from both of these channels. However, it has been recently shown how the Cu L_3-edge spectra can be resolved into their individual SC and NSC components [74]. For this reason, we will consider these two channels separately in what follows.

The momentum transfer has two components in a two-leg ladder geometry: $\mathbf{q} = (q_x, q_y)$, where $q_x = 2\pi n/La$, with $n \in [0, L)$ but $q_y = 0$ or π/a, only. For our ED calculations, we evaluate Eq. (2) directly, while the details of our DMRG approach are given in section 2.2.2 of Chapter 2 [84].

Throughout this study, we use $V_c = 6.7t$, $\Gamma = |t|$ for all n, and a Lorentzian broadening with $\eta = J_{\text{leg}}/6$ for the energy-conserving delta function appearing in Eq. (2), unless stated otherwise. These parameters are typical for Cu L-edge measurements on the cuprates. Most of the spectra were computed using ED on $N = L \times 2 = 10 \times 2$ clusters with periodic boundary conditions, while DMRG was used on $N = L \times 2 = 16 \times 2$ undoped clusters with open boundary conditions. For the doped cases, our ED results are for a filling of $\langle n \rangle = 0.9$ (or 10% doping). Due to the finite size of the lattice, we have discrete peak-like structure in our RIXS plots instead of smooth dispersions, both along momentum and energy axis. Nevertheless, as will become clear in our analysis, the computed RIXS response of small size systems still

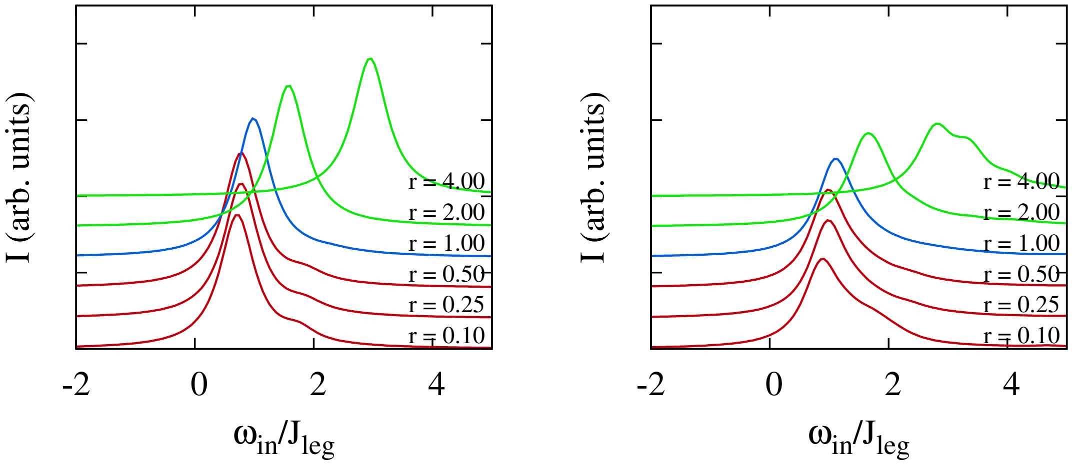

Figure 5.2: XAS spectra for the undoped (left panel; $n = 1.0$) and doped (right panel; $n = 0.9$) ladders for various values of $r = \frac{J_{\text{rung}}}{J_{\text{leg}}}$, using ED and a 10×2 cluster. Increasing the rung coupling factor r, the peak position of the XAS shifts to higher incident photon energies.

captures the correct energy scales of the excitations as evident from the comparison with the overlays evaluated from other methods with better momentum resolution.

X-ray absorption: — For all the RIXS figures discussed in this chapter, we tuned the incident photon energy to the peak position observed in the x-ray absorption (XAS) spectra given by

$$I(\omega_{\text{in}}) = \sum_n \left|\langle n|D_{\mathbf{k}=0}|g\rangle\right|^2 \delta(E_n - E_g - \omega_{\text{in}}). \tag{5.3}$$

Figure 5.2 shows the XAS spectra for the undoped and doped cases as a function of the rung coupling $r = J_{\text{rung}}/J_{\text{leg}}$. For the undoped two-leg ladder shown in left panel of Fig. 5.2, the resonance peak in the XAS spectra shifts to larger values of ω_{in} with increasing rung coupling. In the strong-rung case ($r > 1$), the ladder acts as a collection of rung-dimers and the shift in the XAS peak reflects the increased cost of breaking the dimer singlets. For the doped two-leg ladder shown in right panel of Fig. 5.2, the overall intensity of the XAS also decreases with increasing r and an additional peak appears on the high-energy side of the resonance.

5.3 Results and Discussion

We calculated the RIXS spectra in various rung coupling regimes, ranging from *strong* ($r = \frac{J_\text{rung}}{J_\text{leg}} = 4,\ 2$), to *isotropic* ($r = 1$), to *weak* ($r = 0.5, 0.25, 0.1$). But before examining our results, it is worthwhile to review the various excitations that are expected in a two-leg spin-ladder system.

The magnetic excitations of undoped spin-$\frac{1}{2}$ ladders in the *strong* rung coupling limit are well understood starting from a dimerized rung basis [72, 160]. For $r \to \infty$, the individual rungs of the ladder are decoupled, each forming a spin dimer. For the antiferromagnetic case, the ground state of the L-rung ladder is then a direct product of rung singlets with total spin $S = 0$. The elementary excitations of this state are "triplons" [161, 162, 163], where one or more of the rungs are excited into the triplet manifold.[1] For example, the first excited state is L-fold degenerate, where one of the rungs is in a triplet spin configuration, while the higher lying excited states involve integer numbers of rung triplets distributed throughout the system. The degeneracy of the excited states is lifted when $J_\text{leg} \neq 0$, leading to a dispersive quasiparticle excitation. To order $\mathcal{O}\left(J_\text{leg}^2/J_\text{rung}\right)$, the triplon dispersion is [163]

$$\omega_t(q) = J_\text{rung}\left[1 + \frac{1}{r}\cos(qa) + \frac{3}{4r^2}\right], \tag{5.4}$$

where a is the lattice constant along the leg direction.

The two-triplon excitation manifold is even richer. Here, the two-triplon excitations appear in three angular momentum channels corresponding to $S = 0, 1, 2$, namely the *singlet*, *triplet* and *quintet* channels, respectively [160, 164, 165]. Previous work [164] showed that a finite value of J_leg can lead to two-triplon bound states whose dispersions in the singlet ($S = 0$) and triplet ($S = 1$) channels are to order

---

[1] The triplon and bound two-triplon excitations are often referred to as magnon and bound two-magnon excitations, respectively, in the literature. We have adopted the triplon nomenclature to be consistent with the previous RIXS studies [2, 59].

$\mathcal{O}\left(J_{\text{leg}}^3/J_{\text{rung}}^2\right)$ given by [160]

$$\begin{aligned}\omega_{2t}^{S}(q) = J_{\text{rung}}\Big[&2 - \tfrac{3}{2r} + \tfrac{19}{16r^2} - \tfrac{9}{32r^3} - \left(\tfrac{1}{2r} - \tfrac{1}{8r^2} + \tfrac{51}{128r^3}\right)\cos(qa) \\ &- \left(\tfrac{5}{16r^2} + \tfrac{21}{32r^3}\right)\cos(2qa) - \tfrac{37}{128r^3}\cos(3qa)\Big],\end{aligned} \tag{5.5}$$

and

$$\begin{aligned}\omega_{2t}^{T}(q) = J_{\text{rung}}\Big[&2 - \tfrac{3}{2r} + \tfrac{11}{8r^2} + \tfrac{17}{16r^3} - \left(\tfrac{1}{r} + \tfrac{1}{4r^2} - \tfrac{9}{16r^3}\right)\cos(qa) \\ &- \left(\tfrac{1}{2r^2} + \tfrac{1}{2r^3}\right)\cos(2qa) - \tfrac{5}{16r^3}\cos(3qa)\Big],\end{aligned} \tag{5.6}$$

respectively.

The two-triplon excitations in the *triplet* channel were analyzed in a recent INS study [56], reporting a dispersive excitation along the $\mathbf{q} = (q_x, 0)$ direction in the Brillouin zone, in very good agreement with the *lower boundary* line of the two-triplon continuum. It was also argued that the four-spin ring-exchange term frustrates the formation of a $S = 1$ bound state below the continuum. In this effort, we neglect the four-spin cyclic exchange, thus we find that our data overlays well with the dispersion of the $S = 1$ two-triplon bound state. Our results are also consistent with the available RIXS experimental data [2]. We know of no experimental study probing two-triplon excitations in the *singlet* and *quintet* channels; however, our results below show that the RIXS SC channel can access the two-triplon bound state in the *singlet* channel.

In the *weak* rung coupling limit for undoped two-leg spin-$\frac{1}{2}$ ladders, the system can be viewed as a set of weakly coupled Heisenberg chains. In this regime, the excitation spectrum is understood in terms of a confined spinon continuum with a finite spin gap [166]. Intuitively, the excitations of a Heisenberg chain are spin-$\frac{1}{2}$ spinons, which always appear in pairs and are basically free to move along a single chain. When the two chains are coupled antiferromagnetically, however, the spinons within a single chain feel an effective confining potential [70]. This potential is created by the region of ferromagnetically coupled spins that forms on the rungs between the two spinons as they separate.

When $r \ll 1$, the two-leg ladder problem can be mapped onto one of weakly interacting *singlet* and *triplet* Majorana fermions with effective masses $m_s = 3m$ and $m_t = m$, respectively, where $m \approx 0.41 J_{\text{rung}}$ [167]. The excitation spectrum, as encoded in the dynamical spin structure factor $S(q, \omega)$ [62], is characterized by combination of sharp modes and a broader continuum arising from several multi-particle Majorana excitations. The lower boundaries of these excitations are defined by

$$\omega_l(q) \approx \sqrt{m_{\text{thres}}^2 + v^2(q_x - q_x^{\text{min}})}, \tag{5.7}$$

where $v = \frac{\pi J_{\text{leg}}}{2}$ is the spin velocity of the chain and m_{thres} and $\mathbf{q}^{\text{min}}$ depend on the particles involved in the excitation. A summary of the relevant values can be found in Table I of Ref. [62], which we have reproduced in Table 5.1 for convenience. From this table, one can see that a Majorana triplet (1T) excitation appears near $\mathbf{q}^{\text{min}} = (\pi/a, \pi/a)$ and $m_{\text{thres}} = m$, while the excitations near $\mathbf{q}^{\text{min}} = (\pi/a, 0)$ correspond to a three-particle bound state consisting of two Majorana triplets and a Majorana singlet (2T + 1S) with a threshold set by $m_{\text{thres}} = 5m$. While the mapping to the Majorana fermion picture holds for $r \ll 1$, recent DMRG results for $S(q, \omega)$ [62] have shown that this picture provides a qualitative description of the excitation spectrum for a wide range of $r < 1$. These same calculations also showed that the spectral weight of the multi-particle continuum increases as $r \to 0$ until the entire excitation spectrum converges to the expected two-spinon continuum of the antiferromagnetic Heisenberg chain with lower and upper boundaries given by $\omega_s^l(q) = \frac{\pi}{2} J \left|\sin(qa)\right|$ and $\omega_s^u(q) = \pi J \left|\sin(qa/2)\right|$, respectively.

Understanding the behavior of a small number of holes doped into an antiferromagnetic background is one of the central problems in the quest to comprehend unconventional superconductivity. In this context less is known about the excitations in doped spin-ladders as compared to the undoped case, where the former are usually studied using numerical methods [72, 168, 169, 170, 171, 172]. A single hole doped into a two-leg ladder introduces a spin $\frac{1}{2}$ and charge $+e$ to the system. DMRG

Table 5.2: The momentum $\mathbf{q}^{\text{min}}$ and m_{thres} values that define the lower boundaries of the single- and multiparticle excitations that occur in the Majorana fermion description of the spin-$\frac{1}{2}$ ladders. Reproduced from Ref. [62].

Excitation	$\mathbf{q}^{\text{min}}$	m_{thres}
1T	$(\pi/a, \pi/a)$	$1m$
2T	$(0, 0)$	$2m$
3T	$(\pi/a, \pi/a)$	$3m$
1T + 1S	$(0, \pi/a)$	$4m$
2T + 1S	$(\pi/a, 0)$	$5m$

results [169] indicate that in the strong-rung coupling limit, the doped hole behaves as a quasiparticle, where the spin and charge remain tightly bound within a typical distance of about one lattice constant. In the isotropic limit, the quasiparticle develops more internal structure with a length scale of $\sim 3a$. In the decoupled case ($J_{\text{rung}} = 0$), the doped hole fractionalizes completely into a spinon and holon [97, 125].

In the analysis below, we explore the RIXS spectra in both the NSC and SC channels and identify the relevant elementary excitations in these spectra.

5.3.1 Results for the non-spin-conserving channel

We begin our study with the NSC or "spin-flip" channel, which typically dominates the Cu L-edge RIXS spectra in cuprates [74, 113]. The NSC channel produces local single spin-flips due to a large spin-orbit coupling in the $2p$ core level, as shown in Fig 5.1(b). The elementary excitations generated in this scattering channel correspond to magnetic excitations with $\Delta S = 1$ relative to the ground state. In terms of the spectra, the NSC channel is comparable to the spin-flip channel of INS, and hence RIXS spectra at the Cu L-edge of cuprates compare well with $S(\mathbf{q}, \omega)$ (see Sec. 5.3.3) [32, 113].

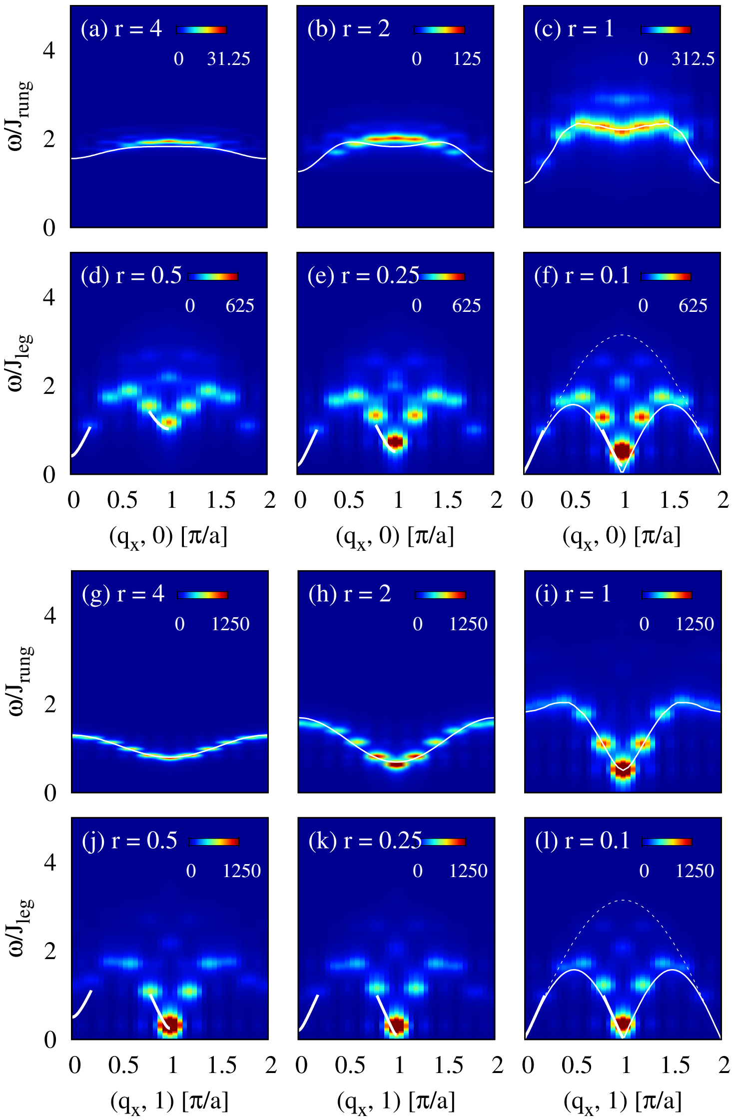

Figure 5.3: The RIXS spectra in the non-spin-conserving channel for a half-filled t-J ladder, using ED and a 10×2 cluster. $I^{\Delta S=1}(q_x, 0, \omega)$ and $I^{\Delta S=1}(q_x, \pi/a, \omega)$ are shown in panels (a)-(f) and (g)-(l), respectively. Panels (a)-(c) and (g)-(i) have overlays of the dispersion relationships for the bound *triplet* two-triplon [Eq. (5.6)] and the one-triplon excitations [Eq. (5.4)], respectively, calculated using perturbation theory. Panels (c) and (i) have overlays (solid white) of the dispersion relationships for the same excitations extracted from Ref. [161], which were evaluated using a continuous unitary transformation (CUT) method. The thin dotted and solid white lines in panels (f) and (l) plot the upper and lower boundaries of the two spinon continuum expected for completely decoupled chains. The thick white lines in panels (d)-(f) and (j)-(l) plot the lower boundaries of the multiparticle continua near their respective minima. Note that the y-axis of the top and bottom rows are scaled with respect to J_{rung} and J_{leg}, respectively.

Undoped t-J ladders

The RIXS spectra in the NSC channel for undoped ladders are plotted in Fig. 5.3. Panels (a)-(f) and (g)-(l) show results for momentum transfers $\mathbf{q} = (q_x, 0)$ and $\mathbf{q} = (q_x, \pi/a)$, respectively. Several excitations are identified.

In the limit of strong rung coupling, the spectra along the $\mathbf{q} = (q_x, 0)$ direction [Figs. 5.3(a) and 5.3(b)] exhibit a dispersive quasiparticle-like excitation. To determine its nature, we overlayed the dispersion $\omega_{2t}^{T}(q)$ given by Eq. (5.6). We find that the observed excitation closely follows the dispersion relationship for $r = 4$ but for $r = 2$ there are some deviations, most notably at the zone boundary. (The disagreement becomes even more apparent for $r = 1$, as discussed below.) The agreement between the dispersion of the excitations and $\omega_{2t}^{T}(q)$, and the fact that we are in the NSC channel, allows us to conclude that these excitations are the two-triplon bound state in the *triplet* channel. Similarily, the $\mathbf{q} = (q_x, \pi/a)$ excitation in the strong-rung coupling case [Figs. 5.3(g) and 5.3(h)] corresponds to a single triplon excitation. To confirm this, we overlayed the dispersion $\omega_t(q)$ given by Eq. (5.4), showing it captures well the observed excitations for $r \geq 2$.

As discussed in the previous section, in the weak-rung coupling limit we expect the legs of the ladders to behave as weakly coupled antiferromagnetic chains. Indeed, along both the $(q_x, 0)$ [Figs. 5.3(d)-(f)] and $(q_x, \pi/a)$ [Figs. 5.3(j)-(l)] directions, the spectra can be described using the picture of confined spinons with a continuum of excitations appearing above a sharper dispersing mode. The lower boundaries of the continua near their respective minima are overlaid as thick white lines. According to Table 5.2, we assign the excitations near $\mathbf{q}^{\text{min}} = (0, 0)$ to 2T excitations with $m_{\text{thres}} = 2m$, while the excitations near $\mathbf{q}^{\text{min}} = (\pi/a, 0)$ correspond the 2T + 1S excitations with $m_{\text{thres}} = 5m$. Similarily, the excitations near $\mathbf{q}^{\text{min}} = (\pi/a, \pi/a)$ are 1T excitations with $m_{\text{thres}} = m$ and the excitations near $\mathbf{q}^{\text{min}} = (0, \pi/a)$ correspond to 1T + 1S excitations with $m_{\text{thres}} \approx 4m$.

The *isotropic* coupling case behaves qualitatively like the strong-rung coupling cases, but the calculated spectra deviate significantly from the dispersion predicted by perturbation theory [Eq. (5.6)]. Nevertheless, we are still able to assign the intense dispersing features to the $S = 1$ two-triplon bound state and the one-triplon excitations, as in the strong-rung coupling limit. In Fig. 5.3(c) and Fig. 5.3(i) we have overlayed the dispersions of *triplet* two-triplon bound states and one-triplon excitations, respectively, this time extracted from Fig. 4 of Ref. [161]. In this case, the dispersions were computed using a continuous unitary transformation (CUT) method, and agree well with our evaluated spectra. In Fig. 5.3(c) we also observe additional spectral weight at higher energies, which corresponds to the two-triplon continuum. Our results in this regime should be of considerable interest for future RIXS experiments on cuprate spin-$\frac{1}{2}$ ladder materials, as most of the estimated values of the $J_{\text{rung}}/J_{\text{leg}}$ ratios fall in this intermediate category.

Doped t-J ladders

The excitations of doped ladder compounds are relevant to explain pressure-induced superconductivity. Moreover, while low-energy spin-fluctuations are widely considered pivotal for superconductivity, the relationship between the doping evolution of charge and high-energy spin excitations and the superconducting mechanism has recently become the subject of considerable debate, especially in 2D cuprates. Our results for the RIXS spectra of the doped spin-ladder in the NSC-channel are in Fig. 5.4. As in the undoped case, panels (a)-(f) and (g)-(l) show spectra along the $(q_x, 0)$ and $(q_x, \pi/a)$ directions, respectively.

For strong-rung couplings [Figs. 5.4(a) and 5.4(b)], the spectra along the $\mathbf{q} = (q_x, 0)$ directions have two distinct sets of excitations. The first corresponds to the same *triplet* two-triplon excitations identified in the undoped case, as confirmed by overlaying the dispersion given by Eq. (5.6) as solid white lines. The second is the Bloch quasiparticle excitation formed from the tightly bound spin and charge of the doped hole [169]. Its dispersion is well described by $\omega(k) = 2\tilde{t}[1 - \cos(ka)]$ (the

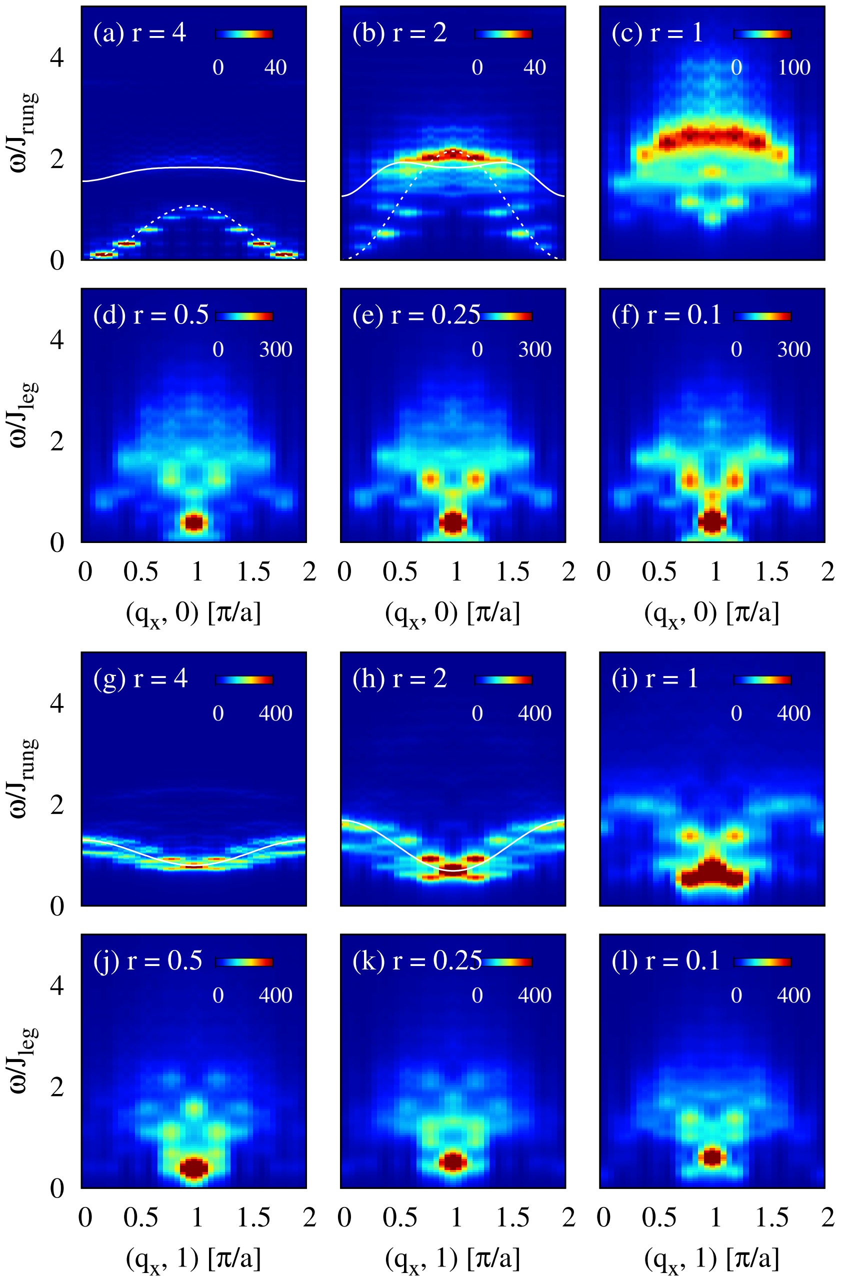

Figure 5.4: RIXS spectra in the non-spin-conserving channel for a doped t-J ladder, using ED on a 10×2 cluster and a filling of $\langle n \rangle = 0.9$. $I^{\Delta S=1}(q_x, 0, \omega)$ and $I^{\Delta S=1}(q_x, \pi/a, \omega)$ are in panels (a)-(f) and (g)-(l), respectively. Panels (a), (b) and (g), (h) have overlays (solid white) of the dispersion relationships for the bound *triplet* two-triplon [Eq. (5.6)] and one-triplon excitations [Eq. (5.4)], respectively, derived using perturbation theory. Panels (a) and (b) have an additional overly (dashed white) of the dispersion for a quasiparticle $\omega(k) = 2\tilde{t}[1 - \cos(ka)]$. The y-axis of the top and bottom rows are scaled with respect to J_{rung} and J_{leg}, respectively.

dashed line overlay), where $\tilde{t} = t_{\text{rung}}/2$ is the effective hopping of a quasiparticle in the bonding band [168]. The fact that the spectra exhibit gapless charge and gapped spin (C1S0) excitations is consistent with the system's classification as a Luther-Emery liquid [168, 173]. The spectra along the $\mathbf{q} = (q_x, \pi/a)$ direction, shown in Figs. 5.4(g) and 5.4(h), have only a single set of excitations, whose dispersions agree well with the one-triplon excitation Eq. (5.4), which is again overlaided as a solid white line.

Results for the weak-rung coupling regime along the $\mathbf{q} = (q_x, 0)$ and $(q_x, \pi/a)$ directions are shown in Figs. 5.4(d)-(f) and Figs. 5.4(j)-(l), respectively. We find that the spectra soften as compared to the undoped spin ladders. Moreover, the spin gap no longer appears to scale with J_{rung} but instead appears to vanish at $(\pi/a, 0)$ for all $r < 1$ while persisting at $\mathbf{q} = (\pi/a, \pi/a)$.

In the *isotropic* case at $\mathbf{q} = (0, \pi/a)$, shown in Fig. 5.4(c), the brightest dispersing peak does not have the same downturn in the two-triplon dispersion that was observed in the undoped case. Instead, there is an increased weight appearing in at higher energy losses, corresponding to the two-triplon continuum. In contrast, the excitations at $\mathbf{q} = (\pi/a, \pi/a)$, shown in Fig. 5.4(i), have the ubiquitous incommensurate peaks that are also commonly observed in doped ladders and 2D cuprates [172, 174, 175, 176]. It is interesting to contrast the results for the doped two-leg spin ladder found above with available results in the doped 2D cuprates at the Cu L-edge. In 2D cuprates, a weakly dispersive high-energy paramagnon band along the $\mathbf{q} = (q_x, 0)$ line was reported to be persistent upon hole doping [4, 30, 32, 33, 34]. This type of excitation compares relatively well with our results in the two-leg ladder case in Fig. 5.4(c) for the isotropic case.

5.3.2 Results for the spin-conserving channel

We now analyze the RIXS spectra in the SC channel, both for the undoped and doped cases. As shown pictorially in Figs. 5.1(c) and 5.1(d), the magnetic excitations that are accessible in this channel occur via double spin-flip processes, which correspond to $\Delta S = 0$ excitations in the antiferromagnetic ladders. For the undoped cuprates measured at the Cu L-edge, the SC channel probes excitations encoded in the dynamical exchange structure factor $S^{\text{exch}}(\mathbf{q}, \omega)$ (see Sec. 5.3.3), which is a second order term in the ultrashort core-hole lifetime (UCL) expansion [88, 113]. The fact that $S^{\text{exch}}(\mathbf{q}, \omega)$ captures most of the RIXS intensity indicates that magnetic excitations in this channel are dominated by double spin-flip processes. Because these are higher order processes, this channel is expected to be weaker as compared to the NSC channel, [74, 113] and our results are consistent with this expectation. In the doped case, magnetic and charge excitations coexist in the RIXS spectra and the SC channel also has a significant contribution at second order given by a modified charge structure factor $\tilde{N}(\mathbf{q}, \omega)$ (see Eq. (9) of Ref. [113] and Sec. 5.3.3). The SC channel is also particularly relevant at the O and Cu K-edges, where direct spin-flip excitations are often forbidden [57, 97, 114]. Our numerical study motivates RIXS experiments that can disentangle SC and NSC components of the spectra by the use of photon polarization, which has been successfully demonstrated in Ref. [74] for the weakly coupled ladder cuprate $CaCu_2O_3$.

Undoped t-J ladders

The RIXS spectra in the SC channel for the undoped ladders are shown in Fig. 5.5. Panels (a)-(f) and (g)-(l) show the RIXS spectra for momentum transfers along the $\mathbf{q} = (q_x, 0)$ and $(q_x, \pi/a)$ directions, respectively. As expected, the intensity of the excitations in this channel is weaker as compared to the NSC channel by approximately one order of magnitude.

As with the previous sections, we first consider the strong-rung coupling limit. Along the $(q_x, 0)$ direction [Figs. 5.5(a) and 5.5(b)], we observe a weakly dispersing feature that agrees well with the two-triplon bound state in the *singlet* channel given by Eq. (5.5). This is one of the important results of our current investigation: because the SC channel probes $\Delta S = 0$ excitations, we are able to clearly identify

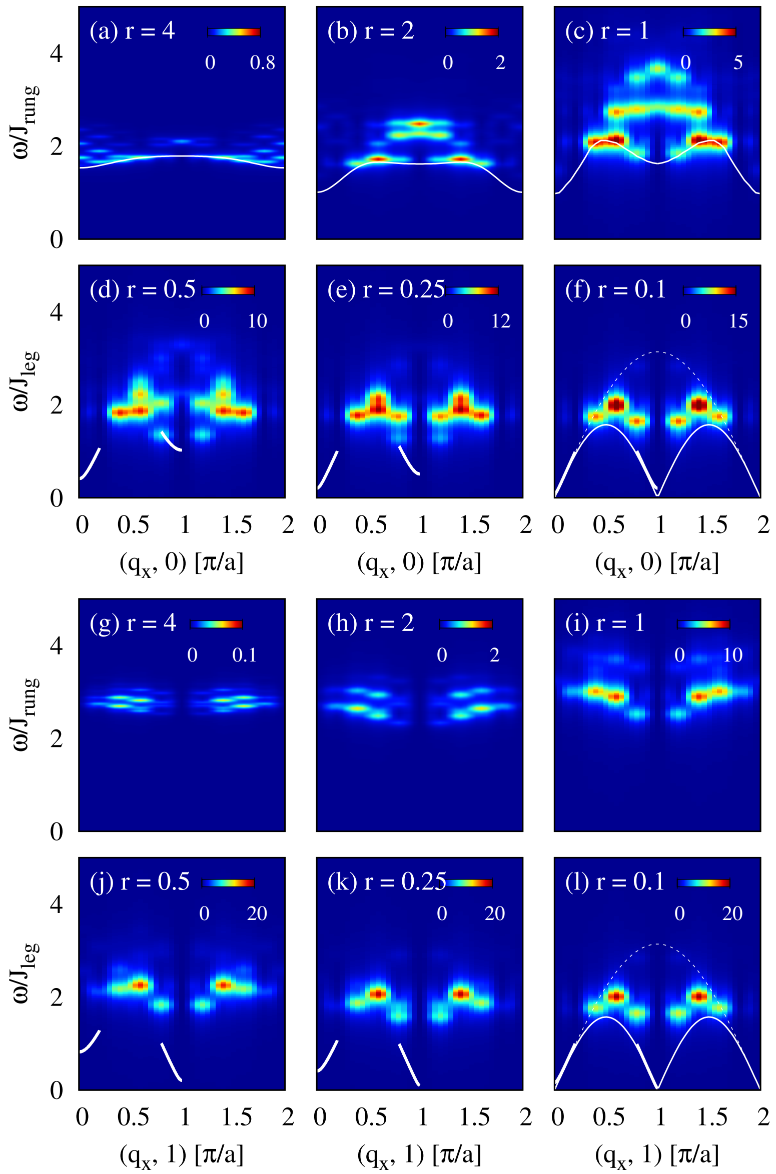

Figure 5.5: RIXS spectra in the spin-conserving channel for the half-filled t-J ladder, using ED and a 10×2 cluster. $I^{\Delta S=0}(q_x, 0, \omega)$ and $I^{\Delta S=0}(q_x, \pi/a, \omega)$ are in panels (a)-(f) and (g)-(l), respectively. Panels (a) and (b) have overlays (solid white) of the dispersion relations of the *singlet* bound two-triplon excitations [Eq. (5.5)] derived using perturbation theory, while panel (c) has an overlay of the dispersion relation for the same excitation from Ref. [161], using the CUT method. The thin dotted and solid white lines in panels (f) and (l) plot the upper and lower boundaries of the two spinon continuum expected for completely decoupled chains. The thick white lines in panels (d)-(f) and (j)-(l) plot the lower boundaries of the multiparticle continua near their respective minima. The y-axis of the top and bottom rows are plotted in units of J_{rung} and J_{leg}, respectively.

and distinguish the two-triplon bound states in both the singlet and triplet channels. We also see additional spectral weight at higher binding energies near $(\pi/a, 0)$, which contrasts qualitatively with the results in the weak-rung coupling limit. This weight falls within the two-triplon continuum and likely corresponds to the two-triplon continuum in the singlet channel.

Along the $\mathbf{q} = (q_x, \pi/a)$ direction in the strong-rung coupling regime shown in panels (g) and (h), the spectra can again be understood as multiparticle excitations in the *singlet* channel, which we observe at energy losses around $3J_{\text{rung}}$. Further analysis of these excitations using strong-coupling series expansion methods is desirable [160]. We observe zero spectral weight at $(\pi/a, \pi/a)$ for all the rung couplings we investigated, in contrast to the weak spectral weight observed at $(\pi/a, 0)$. The nature of these excitations can be qualitatively captured using the dynamical exchange structure factor $S^{\text{exch}}(\mathbf{q}, \omega)$, which has been computed and shown in Fig. 5.9 of Appendix 5.3.3. Indeed, $S^{\text{exch}}(\mathbf{q}, \omega)$ shows the spectral weight cancellation at $(\pi/a, \pi/a)$ for all the rung couplings investigated.

In the weak rung regime ($r < 1$), the spectra along $\mathbf{q} = (q_x, 0)$ and $(q_x, \pi/a)$, shown in Figs. 5.5(d)-(f) and 5.5(j)-(l), respectively, resemble the continuum expected for confined spinons also observed in the NSC channel. To highlight this, we overlaid the boundaries of the two-spinon continuum as well as the lower boundaries of the multi-particle continua that were introduced when describing the NSC channel. In this case, all of the excitations appear above the lower boundary lines, indicating that these excitations are multiparticle in nature. We also note that spectra along both momentum directions have a suppressed intensity at $q_x = \pi/a$, which is similar to what occurs in one-dimensional antiferromagnetic chains when probed in the SC channel [90, 122, 124].

The spectra along both momentum directions for the isotropic case ($r = 1$) behaves qualitatively similar to the strong-rung coupling case, where we observe a continuum of excitations. In Fig. 5.5c, we plot an overlay extracted from Fig. 4(b) of Ref. [161] for bound two-triplon excitation in the *singlet* channel, again evaluated using the CUT method. This dispersion agrees well with the lower boundary of the evaluated spectra suggesting that the continuum of excitations is related to *singlet* two-triplon excitations and that the bound singlet state is not far removed from the continuum.

Doped t-J ladders

Finally, we examine the RIXS spectra of the doped ladders in the SC channel. As before, Figs. 5.6(a)-(f) and 5.6(g)-(l) show results for momentum transfers $\mathbf{q} = (q_x, 0)$ and $(q_x, \pi/a)$, respectively. The spectra are quite rich and we observe several new excitations that were not present in the undoped ladders. Indeed, we expect that magnetic and charge excitations coexist in the SC channel response and that most of the spectral features observed in the full RIXS response can be described using the modified dynamical charge correlation function $\tilde{N}(\mathbf{q}, \omega)$ (see Fig. 5.10 in Sec. 5.3.3 and Ref. [113]).

As before, we begin our discussion from the strong-rung coupling limit. In this case, the ladder can be considered as composed of weakly decoupled dimers where the orbitals on each leg form bonding and antibonding orbitals. If t_{leg} is finite, these bonding (-) and antibonding (+) states form the basis for Bloch states with dispersion relations given by $\omega(q) = \mp t_{\text{rung}} + 2\tilde{t}[1 - \cos(qa)]$ [168], where $\tilde{t}$ is the effective hopping parameter obtained from the change of basis to the bonding and antibonding states. When a small number of holes are doped into the system, they first occupy the bonding band as quasiparticles, as shown in Fig. 5.7. The charge excitations observed in this channel can then be understood by invoking quasiparticle scattering within and between the bonding and antibonding bands, respectively.

Along the $(q_x, 0)$ direction in the strong-rung coupling regime, Figs. 5.6(a) and 5.6(b), we observe dispersive charge excitations consistent with particle-hole scattering within the bonding band, as shown in Fig. 5.7. To confirm this, we overlaid the dispersion $\omega(q) = 2\tilde{t}[1 - \cos(qa)]$, where $\tilde{t} \approx t_{\text{leg}}/2$, which agrees with the numerical data [168]. Along the $(q_x, \pi/a)$ direction [Figs. 5.6(g) and 5.6(h)] we find the

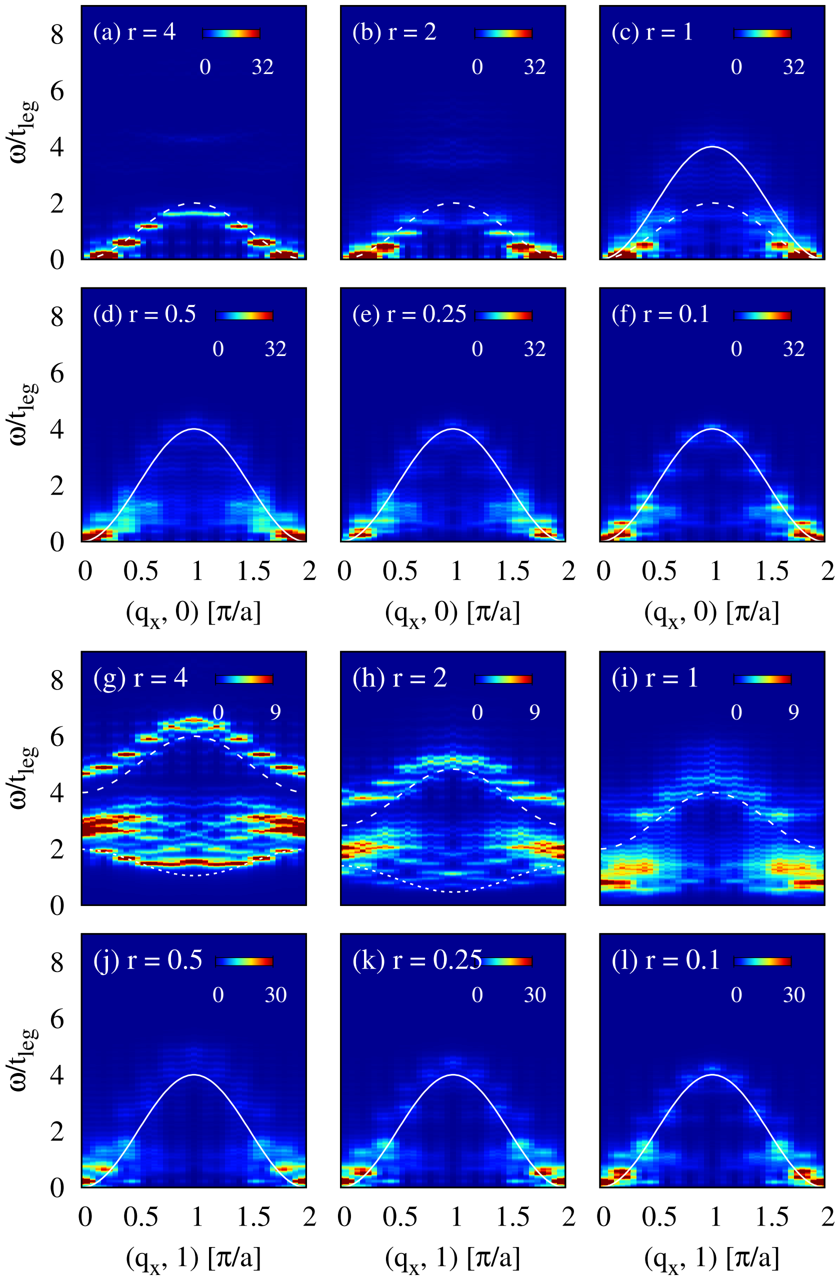

Figure 5.6: RIXS spectra in the spin-conserving channel for the doped t-J ladder, using ED, a 10×2 cluster, and $n = 0.9$. $I^{\Delta S=0}(q_x, 0, \omega)$ and $I^{\Delta S=0}(q_x, \pi/a, \omega)$ are in panels (a)-(f) and (g)-(l), respectively. In panels (a)-(c) the dispersions of the quasiparticle state with a bandwidth $W = 2t_{\text{rung}}$ are shown (white dashed). In panels (d)-(f) and (j)-(l) the holon dispersion with a bandwidth $W = 4t_{\text{leg}}$ is also shown (solid white). The white dashed overlay in panels (g)-(i) plot the boundary of the spinon-holon continuum gapped by $2t_{\text{rung}}$, while the dotted overlay in panels (g) and (h) corresponds to the dispersion relation of the one-triplon excitations. The y-axis of the top row and bottom rows are plotted in units of t_{leg}.

corresponding particle-hole excitation where scattering occurs into the antibonding band. In this case, we overlaid the dispersion $\omega(q) = 2t_{\text{rung}} + 2\tilde{t}[1 - \cos(qa)]$ (white dashed line). We also notice that the bonding and anti-bonding band are separated by $2t_{\text{rung}}$, which accounts for the shift in cosine-like dispersion observed when $q_y = \pi/a$.

It is important to note that, even in this case, these charge excitations are weaker in intensity when compared to the magnetic excitations in NSC channel by approximately one order of magnitude, but stronger than the SC channel of the undoped case. Our results show that RIXS can explicitly probe charge excitations at low energies as suggested in the literature for the Cu L_3-edge [36, 37].

In addition to the charge excitations, we also observe a continuum of magnetic excitations for momentum transfers along $(q_x, \pi/a)$. The lower boundary of this continuum is defined by the one triplon dispersion given by Eq. (5.4), which has been overlaid as a dotted white line.

In the weak-rung coupling regime, shown in Figs. 5.7(d)-(f) and 5.7(j)-(l), the quasiparticle excitations display a bandwidth $4t_{\text{leg}}$ with dispersion $\omega(q) = 2t_{\text{leg}}[1 - \cos(qa)]$ along both the $(q_x, 0)$ and $(q_x, \pi/a)$ directions. This is similar to the results for the 1D AFM chain reported in Ref. [97] where the excitations are holons, and consistent with the notion that the individual legs of the ladder are weakly coupled. The fact that these observed excitations are completely governed by t_{leg} indicates that the holes can be viewed as occupying the chains of the ladder rather than the bonding and antibonding orbitals on each rung.

Finally, we consider the isotropic rung-coupling limit, which is of much interest for future RIXS experiments and future theoretical investigations. In this case, our spectra show a gapless and a gapped continuum along the $(q_x, 0)$ and $(q_x, \pi/a)$ directions, respectively. These results hence resemble qualitatively the spectral features also observed in the strong-rung coupling limit. It is interesting to compare our full RIXS spectra with the dynamical charge structure factor results reported in Fig. 7 of Ref. [71]: our results compare well with the lower Hubbard band excitation observed in which $N(q_x, \pi/a, \omega)$ is gapped, in contrast to the gapless $N(q_x, 0, \omega)$.

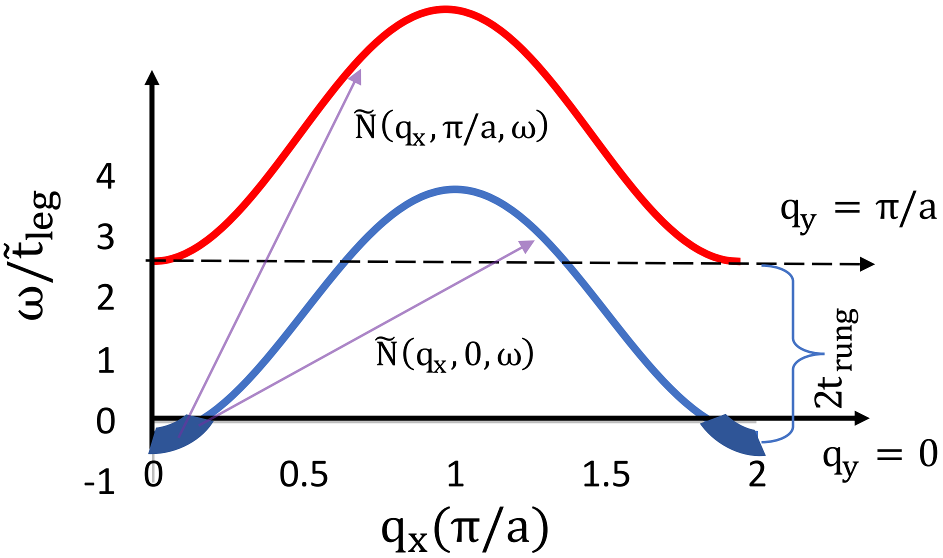

Figure 5.7: A schematic diagram of the particle-hole excitations possible in the doped t-J ladder in the strong-rung coupling regime. In this limit, the orbitals along the legs form bonding $\frac{1}{\sqrt{2}}(c^{\dagger}_{i,\sigma,1} - c^{\dagger}_{i,\sigma,2})|0\rangle$ and anti-bonding $\frac{1}{\sqrt{2}}(c^{\dagger}_{i,\sigma,1} + c^{\dagger}_{i,\sigma,2})|0\rangle$ states, which form the basis for the Bloch states propagating along the leg direction. In this case, the dispersions of the two Bloch states are split by an amount proportional to the rung hopping $\pm t_{\text{rung}}$. The doped holes form quasiparticles carrying both spin-$\frac{1}{2}$ and charge e, and the broad blue colour highlights the filled states in the ground state. RIXS probes scattering within the bonding and to the antibonding band, as shown by the arrows.

5.3.3 Results for the dynamical correlation functions

The interpretation of RIXS spectra computed with the Kramers-Heisenberg formalism can be difficult. To simplify matters, the full RIXS intensity can be expanded in powers of J/Γ using the ultra-short core-hole lifetime (UCL) approximation. This procedure expresses the RIXS intensity as a series of increasingly complicated multi-particle correlation functions, which can then be further subdivided into correlation functions of the NSC and SC channels. The detailed procedure to be followed has been reported in several prior studies [113, 124, 177, 178]. Here, we evaluate some effective correlation functions motivated by Eqs. (B1) and (B2) of Ref. [113]. In many cases, these simplified correlation functions give an accurate description of the RIXS intensity in this chapter.

The spectral weight of the NSC channel is dominated by the first-order term in the UCL expansion, which is equivalent to the dynamical spin structure factor

$$S(\mathbf{q},\omega) = \frac{1}{L}\sum_{f}\left|\langle f|\sum_{i,\tau} e^{i\mathbf{q}\cdot\mathbf{R}_{i,\tau}} S^{\alpha}_{i,\tau}|g\rangle\right|^{2}\delta(E_f - E_g + \omega). \tag{5.8}$$

Here, $S^{\alpha}_{i,\tau}$ ($\alpha = \{\pm, z\}$) is a component of the spin operator at site (i,τ). The $S(\mathbf{q},\omega)$ responses for an undoped ladder along the $(q_x, 0)$ and $(q_x, \pi/a)$ directions are plotted in Figs. 5.8(a)-(c) and 5.8(c)-(f), respectively. These results compare well with the RIXS intensity computed within the Kramers-Heisenberg formalism shown in Figs. 5.3 for all values of the rung coupling.

To account for the magnetic excitations of the SC channel, the second-order term in the UCL expansion of the Kramers-Heisenberg formula is needed (see Eq. (B2) of Ref. [113]). In the undoped case, the first-order term only contributes to the elastic line in this channel and a double spin-flip process appearing at second-order generates magnetic excitations. The RIXS spectra in the SC channel of the undoped ladders is

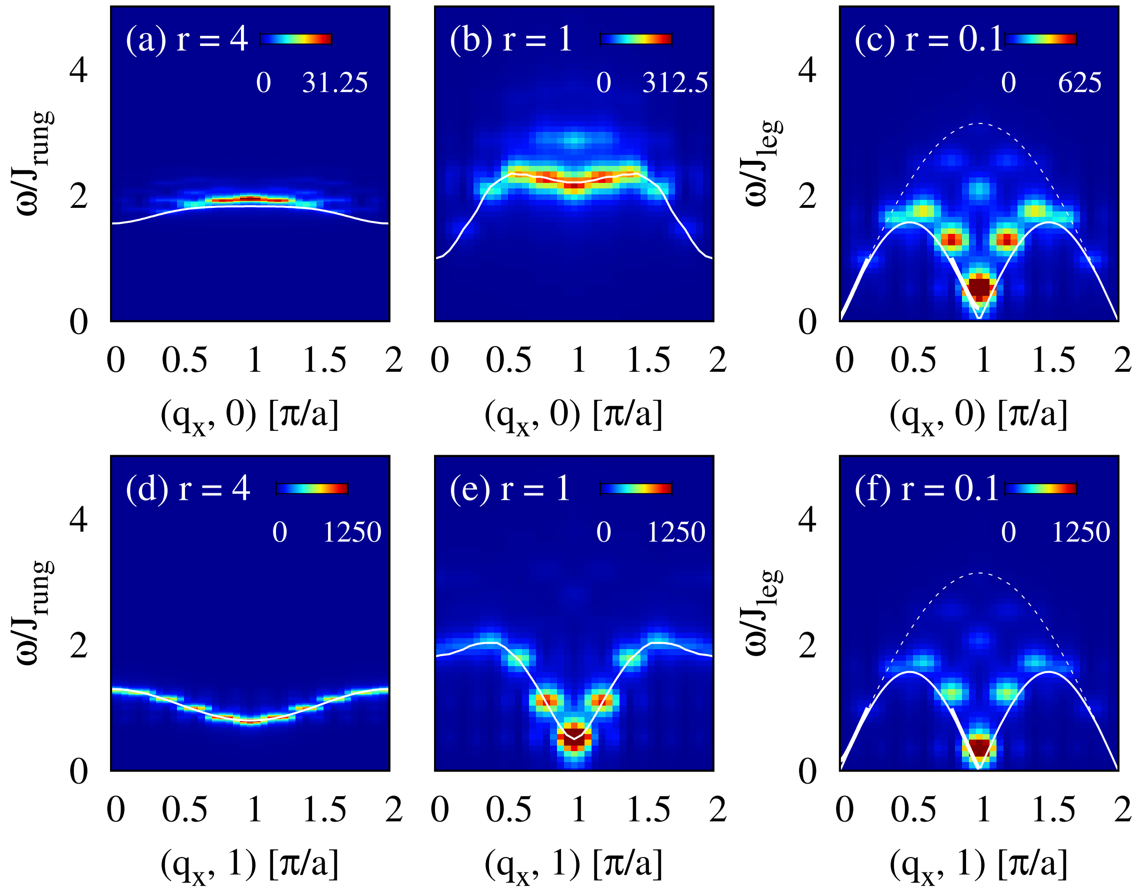

Figure 5.8: The dynamical spin correlation function $S(\mathbf{q}, \omega)$ evaluated for the undoped ladder with $r = \frac{J_{\text{rung}}}{J_{\text{leg}}} = \{4, 1, 0.1\}$ rung couplings, using ED and a 10×2 cluster. Panels (a)-(c) and (d)-(f) show the spectra along the $\mathbf{q} = (q_x, 0)$ and $\mathbf{q} = (q_x, \pi/a)$ directions, respectively. The overall intensity has been rescaled by a factor $1/\Gamma^2$, which corresponds to the prefactor relating $S(\mathbf{q}, \omega)$ to the RIXS intensity. These plots capture all of the features of the spectra presented in Fig. 5.3.

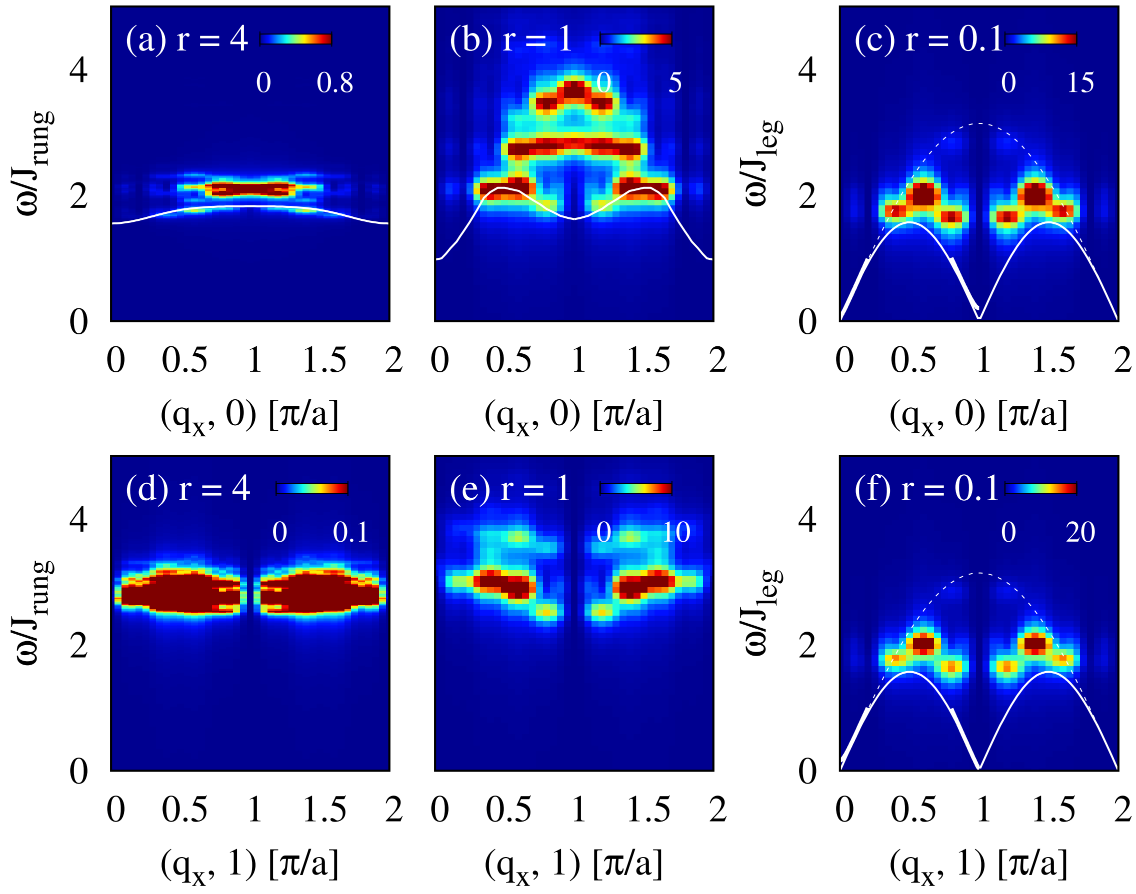

Figure 5.9: The dynamical spin exchange correlation function $S^{\text{exch}}(\mathbf{q}, \omega)$ evaluated for the undoped ladder with $r = \frac{J_{\text{rung}}}{J_{\text{leg}}} = \{4, 1, 0.1\}$ rung couplings, using ED and a 10×2 cluster. Panels (a)-(c) and (d)-(f) show the spectra along the $\mathbf{q} = (q_x, 0)$ and $\mathbf{q} = (q_x, \pi/a)$ directions, respectively. The overall intensity was rescaled by a factor of $1/\Gamma^4$, which corresponds to the prefactor relating $S^{\text{exch}}(\mathbf{q}, \omega)$ to the RIXS intensity. These plots capture many of the features of the spectra Fig. 5.5.

hence dominated by the dynamical spin-exchange structure factor [113, 122, 124]

$$S^{\mathrm{exch}}(\mathbf{q},\omega)=\frac{1}{L}\sum_{f}\Big|\langle f|\sum_{i,\tau}e^{i\mathbf{q}\cdot\mathbf{R}_{i,\tau}}O^{\mathrm{exch}}_{i,\tau}|g\rangle\Big|^2\delta(E_f-E_g+\omega). \tag{5.9}$$

Here, $O^{\mathrm{exch}}_{i,\tau}=\mathbf{S}_{i,\tau}\cdot\left[J_{\mathrm{leg}}\left(\mathbf{S}_{i+1,\tau}+\mathbf{S}_{i-1,\tau}\right)+J_{\mathrm{rung}}\mathbf{S}_{i,\bar{\tau}}\right]/2$ evaluates the spin exchange between nearest-neighbor sites of the ladder, as sketched in Fig. 5.1(c) and 5.1(d).

The results for $S^{\mathrm{exch}}(\mathbf{q},\omega)$ in the undoped ladder along the $(q_x,0)$ and $(q_x,\pi/a)$ directions are shown in Figs. 5.9(a)-(c) and 5.9(d)-(f), respectively. These results compare well with the RIXS intensities shown in Fig. 5.5 evaluted using the full Kramers-Heisenberg formalism. $S^{\mathrm{exch}}(\mathbf{q},\omega)$ captures the correct excitations for weak-rung couplings, but the intensities are overpredicted for strong-rung couplings, the regime where the UCL approximation is expected to fail (large J/Γ).

The SC channel for the doped ladders is dominated by charge excitations. In this case, one must also go to second order and the RIXS intensity is well approximated by a modified dynamical charge structure factor [113]

$$\begin{aligned}\tilde{N}(q,\omega)=\frac{1}{L}\Big(\sum_{f}\Big|\langle f|\sum_{i,\tau}e^{i\mathbf{q}\cdot\mathbf{R}_{i,\tau}}O^{1}_{i,\tau}|g\rangle\Big|^2+\frac{1}{\Gamma^2}\Big|\langle f|\sum_{i,\tau}e^{i\mathbf{q}\cdot\mathbf{R}_{i,\tau}}O^{2}_{i,\tau}|g\rangle\Big|^2\Big)\\ \times\delta(E_f-E_g-\omega).\end{aligned} \tag{5.10}$$

Here, $O^1_{i,\tau}=\sum_\sigma c^\dagger_{i,\tau,\sigma}c_{i,\tau,\sigma}$, $O^2_{i,\tau}=\sum_\sigma[t_{\mathrm{leg}}(c^\dagger_{i+1,\tau,\sigma}+c^\dagger_{i-1,\tau,\sigma})+t_{\mathrm{rung}}c^\dagger_{i,\bar{\tau},\sigma}]c_{i,\tau,\sigma}/2$, and $c_{i,\tau,\sigma}$ annihilates a spin σ hole at site (i,τ), subject to the constraint of no double occupancy. Results for $\tilde{N}(\mathbf{q},\omega)$ along the $(q_x,0)$ and $(q_x,\pi/a)$ directions are shown in panels Fig. 5.10(a)-(c) and Fig. 5.10(d)-(f), respectively. In the doped case, the first-order term is non-zero but the majority of the intensity is set by the second-order term. The $\tilde{N}(\mathbf{q},\omega)$ results compare reasonably well to the RIXS spectra shown in Fig. 5.6 evaluated using the full Kramers-Heisenberg formalism.

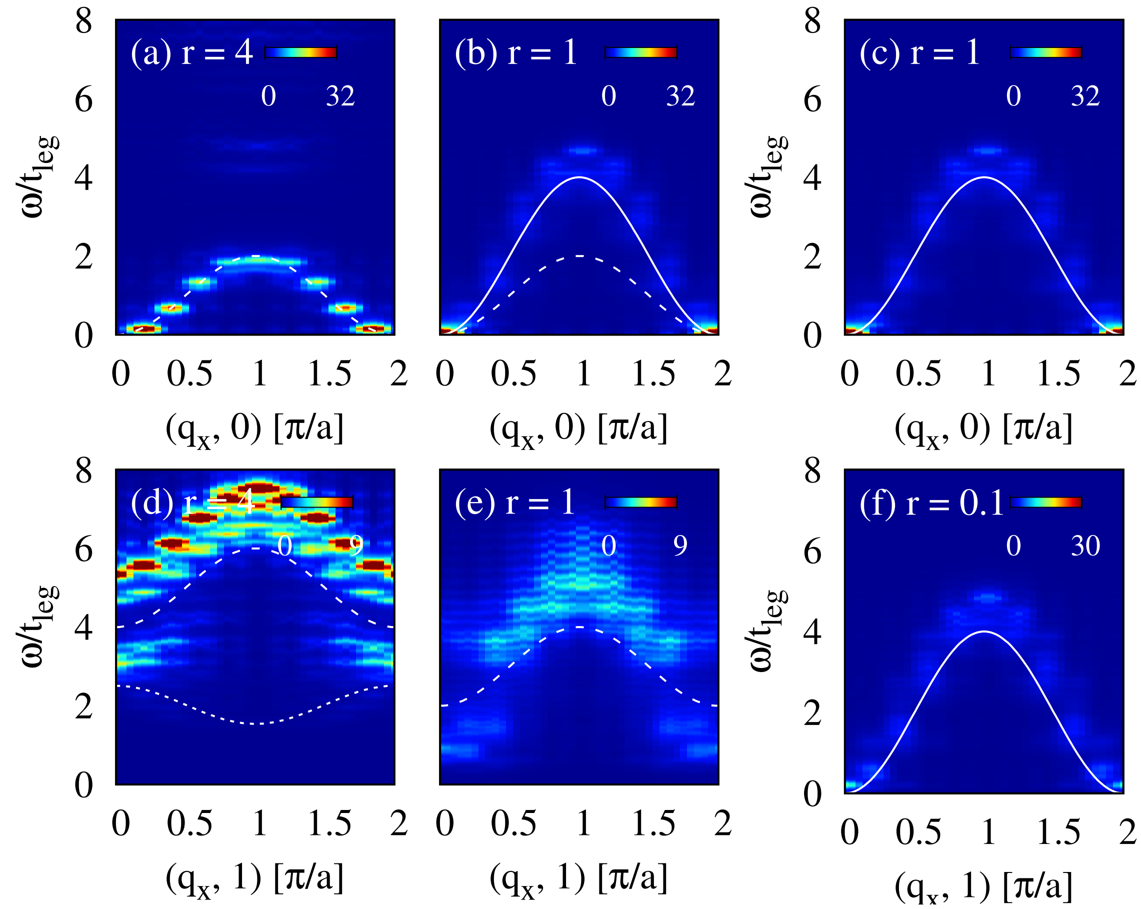

Figure 5.10: The modified dynamical charge structure factor $\tilde{N}(\mathbf{q},\omega)$ evaluated for the doped ladder with $r = \frac{J_{\text{rung}}}{J_{\text{leg}}} = \{4, 1, 0.1\}$ rung couplings, using ED, a 10×2 cluster, and $n = 0.9$. Panels (a)-(c) and (d)-(f) show the spectra along the $\mathbf{q} = (q_x, 0)$ and $\mathbf{q} = (q_x, \pi/a)$ directions, respectively. The overall intensity has been rescaled by a factor $1/\Gamma^2$, corresponding to the prefactor relating $\tilde{N}(\mathbf{q},\omega)$ to the RIXS intensity. These plots capture many of the features of the spectra presented in Fig. 5.6.

5.3.4 Revisiting $Sr_{14}Cu_{24}O_{41}$ RIXS data

Cu L_3-edge RIXS data has been reported [2] for the prototypical spin-ladder $Sr_{14}Cu_{24}O_{41}$. At that time, the observed spectra were interpreted in terms of two-triplon $\Delta S = 0$ excitations in the strong rung coupling regime ($r \approx 1.37$) as it was believed that $\Delta S = 1$ excitations were forbidden at the Cu L_3-edge. It was later shown that not only is this channel allowed but that it dominates the magnetic RIXS response in the undoped cuprates [29]. The RIXS spectra were later theoretically evaluated [59] employing a projection method for the two-leg ladder using the parameter set derived from $La_4Sr_{10}Cu_{24}O_{41}$ in Ref. [56] (the model involved additional ring spin-exchange term as compared to our model). These calculations showed that the RIXS spectra was associated with the two-triplon excitations with $\Delta S = 1$ when momentum transfers of $q_y = 0$ were used, as shown in Fig. 6 of Ref. [59]. But there was also a significant difference in the dispersion of the experimental and theoretical data. Armed now with these theoretical insights of this chapter and our new model calculations, we revisit the existing $Sr_{14}Cu_{24}O_{41}$ data.

To access large system sizes with improved momentum resolution, we computed the RIXS spectra in the $\Delta S = 1$ channel for an undoped spin-ladder using our recently formulated DMRG approach [84]. To obtain a unified description of RIXS and INS experiments, we first adopted a model given by Eq. (5.1) without ring exchange terms, however, we found that this model gave poor agreement with the experimentally observed RIXS spectra. Instead, we are able to find good agreement when we set $J_{\text{leg}} = 145$ meV and $J_{\text{rung}} = 0.85 J_{\text{leg}}$. This result places $Sr_{14}Cu_{24}O_{41}$ in the weak rung-coupling regime but close to the isotropic limit. The resulting RIXS spectra shown in Fig. 5.11 agree well with the experimental data, but the theoretical model predicts a vanishing spectral weight at $q_x = 0$. This observation is consistent with the model of Ref. [59] but inconsistent with the finite intensity observed in the experiment. At this time, the source of this discrepancy is unclear.

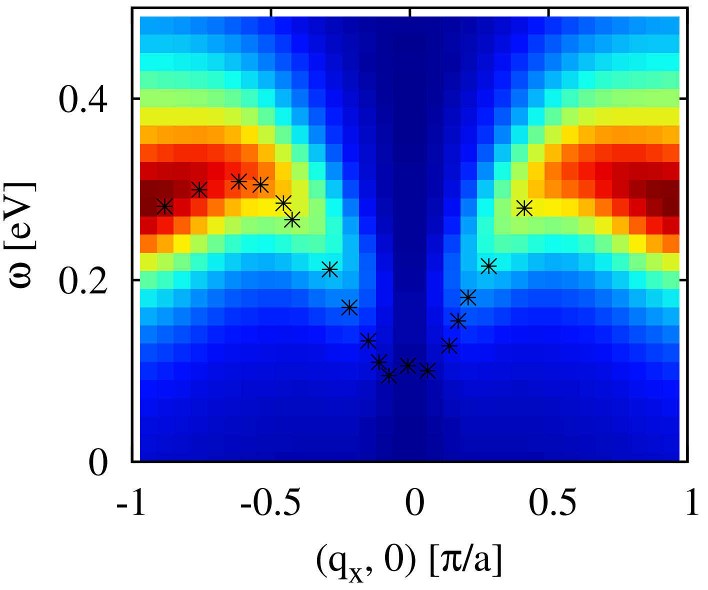

Figure 5.11: Calculated RIXS spectra of an undoped t-J ladder in the non-spin-conserving channel $I^{\Delta S=1}(q_x, 0, \omega)$ evaluated using DMRG on an $N = 16 \times 2$ lattice. The black squares overlay the peak positions of the spectra extracted from the experimental Cu L$_3$-edge data for $Sr_{14}Cu_{24}O_{41}$, reproduced from Ref. [2].

Because r is close to the isotropic case, the data can be qualitatively understood using either the dimer excitation picture or the confined spinon picture. In the former case, the excitations are understood as $S = 1$ two-triplet bound excitations. In the latter case, they are viewed as a three particle bound state composed of Majorana fermions near the zone boundary. However, a quantitative description of the data can only be achieved with nonperturbative numerical methods. In this sense, our results place $Sr_{14}Cu_{24}O_{41}$ in a regime similar to the organometallic compound $(C_7H_{10}N)_2CuBr_4$ [62], but with larger exchange couplings.

5.4 Conclusions

In this chapter, we have systematically studied the RIXS spectra of both undoped and doped spin-$\frac{1}{2}$ ladders, covering the weak- to strong-rung coupling regimes. Our study shows that RIXS experiments performed on these compounds can access a wealth of magnetic and charge excitations. This study was motivated by RIXS experiments at the Cu L-edge in low-dimensional cuprates, where the RIXS data can be decomposed into the non-spin-conserving (NSC) and spin conserving (SC) channels [74, 90, 113, 114]. Therefore, we evaluated the RIXS spectra in both of these channels and provided an energy-momentum resolved roadmap that can guide future RIXS experiments on spin-ladder compounds.

In the first part of this chapter, we reported the RIXS excitations in the NSC or "spin-flip" channel, which typically dominates the Cu L-edge RIXS spectra in the cuprates [74, 113]. In the undoped two-leg ladder, we have shown that RIXS can access dispersive one triplon excitations and a two-triplon bound state in the *triplet* ($S = 1$) channel in the intermediate to strong rung coupling regime. In the weak-rung coupling regime, the NSC channel probes single- and multiparticle excitations consistent with the Majorana fermion description of confined spinons.

The study of the RIXS spectra for doped spin-$\frac{1}{2}$ ladder compounds is of much importance in the context of pressure-induced superconductivity in low-dimensional high-$\mathrm{T_c}$ cuprates. In the doped ladder, we accessed one- and (triplet) two-triplon excitations in the strong-rung coupling limit and softened confined spinons in the weak-rung coupling limit. We also identified signatures of a bound spin-charge quasiparticle excitation in the strong-rung coupling limit.

In the second part of this chapter, we studied the RIXS spectra of the spin-ladder in the SC channel, which probes $\Delta S = 0$ excitations of the system [74, 113]. This component of the RIXS spectra has received less attention in the literature, and our work provides a starting point for future theoretical and experimental investigations of this channel on spin-ladders. In the undoped ladders, magnetic excitations are created in this channel via double spin-flip processes. Because these are higher order processes, their contribution to the RIXS spectra is expected to be weaker compared to the NSC channel [74, 113]. Our results are consistent with this expectation, and we found that the spectral intensity is at least one order of magnitude smaller than the corresponding spectra in the SC channel. Nevertheless, in the intermediate to strong rung coupling regime, we are able to identify bound two-triplon excitations in the singlet ($S = 0$) channel.

In the SC RIXS channel for doped spin-ladders, we identified a set of dispersive low-energy charge excitations that were interpreted by invoking quasiparticle scattering within and between the bonding and antibonding bands, respectively, in the strong rung coupling case. Conversely, the spectra are dominated by holon excitations in the weak-rung coupling limit. The direct access to charge excitations offered by this channel provides a new opportunity to study superconductivity in cuprate ladders, where the role of spin and charge excitations is still debated. We believe our numerical study motivates new RIXS experiments on spin-ladders such as $\mathrm{Sr_{14}Cu_{24}O_{41}}$ allowing disentanglement of data into the NSC and SC channels, due to the richness predicted in the RIXS spectra.

Since the Kramers-Heisenberg formalism is complicated, we also reproduced the RIXS cross-section using simpler correlation functions. It was shown that the RIXS spectra observed in the NSC channel are captured well by $S(q,\omega)$. To capture the RIXS spectra in the SC channel, higher order correlation functions such as $S^{\mathrm{exch}}(q,\omega)$ and $\tilde{N}(q,\omega)$ are needed for the undoped and doped spin ladders, respectively. Studying these correlation functions on spin-ladders using analytical methods will allow one to characterize the excitations observed in these responses.

Finally, we revisited the available RIXS data for $\mathrm{Sr_{14}Cu_{24}O_{41}}$ and found that it was best described using a model in the weak rung coupling regime with $r = 0.85$. This result is in contrast to the previous analysis [2] that placed it in the strong rung coupling regime but in qualitative agreement with the INS data [42].

Chapter 6

Summary and Outlook

This dissertation presented the spin and charge dynamics of quasi-one-dimensional (1D) antiferromagnets as revealed by resonant inelastic x-ray scattering (RIXS) using numerical methods such as exact diagonalization (ED) and density matrix renormalization group (DMRG). Specifically, we reported several exotic fractionalized quasiparticles as revealed in the RIXS spectra of 1D chain and two-leg ladders.

In chapter 1, we discussed the need for investigating 1D cuprates using RIXS and how such studies complement those of two-dimensional (2D) cuprates. The crystal structure of Sr_2CuO_3 and $Sr_{14}Cu_{24}O_{41}$, and how these compounds realize 1D antiferromagnetic chain and two-leg ladder structures, respectively, was discussed. In chapter 2, we introduced the RIXS cross-section, starting with the theory of light-matter interactions, and how the Kramers-Heisenberg formalism captures RIXS cross-section. Numerical methods, such as ED and DMRG used in this thesis were also discussed.

In chapter 3, we reported the first direct observation of multi-spinon excitations at the oxygen K-edge of Sr_2CuO_3. We demonstrated that RIXS grants access to complementary correlation functions for magnetic scattering compared to INS, which arises from the lifetime and dynamics of the intermediate state. Importantly, this new scattering channel was shown to be unique to RIXS and provides access to non-local spin correlation functions beyond the two-site correlation functions probed by traditional scattering techniques. O K-edge RIXS with long core-hole lifetimes, is therefore demonstrated as an important probe for examining excitations that cannot be detected by INS, as long lifetimes of the intermediate state allow charge fluctuations to take place during the scattering process.

In chapter 4, we showed that spin-charge separation can be observed in O K-edge RIXS on doped Sr_2CuO_3, and further, that these systems exhibit remarkably rich spectra consisting of multi-spinon and holon excitations. Our results highlighted the potential for RIXS to simultaneously access the charge and spin degrees of freedom in fractionalized quasiparticle excitations, applicable to many quantum materials. The availability of doped Sr_2CuO_3 and $SrCuO_2$ crystals [53, 54, 149] give us confidence that our predictions can be verified experimentally in the near future.

In chapter 5, we systematically studied the RIXS spectra of both undoped and doped spin-$\frac{1}{2}$ ladders, covering the weak- to strong-rung coupling regimes. Since RIXS data at the Cu L-edge of cuprates can be decomposed into the non-spin-conserving (NSC) and spin conserving (SC) channels [74, 90, 113, 114], we investigated both these channels and provided an energy-momentum resolved roadmap that can guide future RIXS experiments on spin-ladder compounds. Our study showed that RIXS experiments performed on these compounds can access a wealth of magnetic and charge excitations. Importantly, we showed that the SC channel allows one to observe *singlet* two-triplon bound states in spin ladders. Conversely, in the doped case, the SC channel primarily probes gapless and gapped charge excitations, originating due to bonding and antibonding states of a bound spin-1/2 and charge along a rung of the ladder. Finally, we revisited the available experimental data for the ladder compound $Sr_{14}Cu_{24}O_{41}$ [2] in the context of our results. Our work classifies this ladder compound in the $J_{\mathrm{rung}}/J_{\mathrm{leg}} < 1$ limit, instead of the $J_{\mathrm{rung}}/J_{\mathrm{leg}} > 1$ limit reported earlier [2, 132].

In this thesis, we have largely characterized the signatures of spin and charge dynamics in both the undoped and doped 1D chain and ladder antiferromagnets using numerical methods. Our work has motivated RIXS experiments on doped 1D antiferromagnets, and both the undoped and doped two-leg spin ladder compounds to test the richness of our predictions. These predictions would indeed count as some of the most stringent tests of many-body physics in those materials. From a numerical methods perspective, our work is readily expandable to further exotic geometries such as spin-1/2 Kitaev-Heisenberg ladder [179, 180] relevant for Kitaev materials. The recently developed RIXS -DMRG formalism [84] can allow one to simulate the RIXS response of 2D cuprates using multi-leg ladders [174]. In recent years, there have also been advancements in the instrumentation of non-equilibrium RIXS and there is an urgent need for theoretical developments for these probes [181]. The 1D geometries discussed in this thesis are easy to simulate, and hence are the well-suited to explore novel phases of matter such as superconductivity [182] under driven conditions realized in these probes using non-equilibrium RIXS.

Bibliography

[1] Luuk J. P. Ament, Michel van Veenendaal, Thomas P. Devereaux, John P. Hill, and Jeroen van den Brink. Resonant inelastic x-ray scattering studies of elementary excitations. *Rev. Mod. Phys.*, 83:705–767, Jun 2011. 1, 2, 28, 29, 30, 47, 50, 51, 69

[2] J. Schlappa, T. Schmitt, F. Vernay, V. N. Strocov, V. Ilakovac, B. Thielemann, H. M. Rønnow, S. Vanishri, A. Piazzalunga, X. Wang, L. Braicovich, G. Ghiringhelli, C. Marin, J. Mesot, B. Delley, and L. Patthey. Collective magnetic excitations in the spin ladder $Sr_{14}Cu_{24}O_{41}$ measured using high-resolution resonant inelastic x-ray scattering. *Phys. Rev. Lett.*, 103:047401, Jul 2009. 1, 4, 10, 28, 30, 65, 66, 67, 68, 69, 73, 74, 94, 95, 97, 99

[3] L. Braicovich, J. van den Brink, V. Bisogni, M. Moretti Sala, L. J. P. Ament, N. B. Brookes, G. M. De Luca, M. Salluzzo, T. Schmitt, V. N. Strocov, and G. Ghiringhelli. Magnetic excitations and phase separation in the underdoped $La_{2-x}Sr_xCuO_4$ superconductor measured by resonant inelastic x-ray scattering. *Phys. Rev. Lett.*, 104:077002, Feb 2010. 1, 2, 66

[4] M. Le Tacon, M. Minola, D. C. Peets, M. Moretti Sala, S. Blanco-Canosa, V. Hinkov, R. Liang, D. A. Bonn, W. N. Hardy, C. T. Lin, T. Schmitt, L. Braicovich, G. Ghiringhelli, and B. Keimer. Dispersive spin excitations in highly overdoped cuprates revealed by resonant inelastic x-ray scattering. *Phys. Rev. B*, 88:020501, Jul 2013. 1, 2, 66, 81

[5] J. Schlappa, K. Wohlfeld, K. J. Zhou, M. Mourigal, M. W. Haverkort, V. N. Strocov, L. Hozoi, C. Monney, S. Nishimoto, S. Singh, A. Revcolevschi, J.-S. Caux, L. Patthey, H. M. Ronnow, J. van den Brink, and T. Schmitt. Spin-orbital separation in the quasi-one-dimensional mott insulator Sr_2CuO_3. *Nature*, 485:195138, May 2012. 1, 2, 4, 5, 7, 8, 10, 28, 30, 31, 32, 33, 34, 35, 36, 37, 47, 50, 52, 65, 66

[6] B. J. Kim, Hosub Jin, S. J. Moon, J.-Y. Kim, B.-G. Park, C. S. Leem, Jaejun Yu, T. W. Noh, C. Kim, S.-J. Oh, J.-H. Park, V. Durairaj, G. Cao, and E. Rotenberg. Novel $J_{\text{eff}} = 1/2$ mott state induced by relativistic spin-orbit coupling in Sr_2IrO_4. *Phys. Rev. Lett.*, 101:076402, Aug 2008. 1, 67

[7] Luuk J. P. Ament, Giniyat Khaliullin, and Jeroen van den Brink. Theory of resonant inelastic x-ray scattering in iridium oxide compounds: Probing spin-orbit-entangled ground states and excitations. *Phys. Rev. B*, 84:020403, Jul 2011. 1, 67

[8] Jungho Kim, D. Casa, M. H. Upton, T. Gog, Young-June Kim, J. F. Mitchell, M. van Veenendaal, M. Daghofer, J. van den Brink, G. Khaliullin, and B. J. Kim. Magnetic excitation spectra of Sr_2IrO_4 probed by resonant inelastic x-ray scattering: Establishing links to cuprate superconductors. *Phys. Rev. Lett.*, 108:177003, Apr 2012. 1, 67

[9] H. Gretarsson, N. H. Sung, J. Porras, J. Bertinshaw, C. Dietl, Jan A. N. Bruin, A. F. Bangura, Y. K. Kim, R. Dinnebier, Jungho Kim, A. Al-Zein, M. Moretti Sala, M. Krisch, M. Le Tacon, B. Keimer, and B. J. Kim. Persistent paramagnons deep in the metallic phase of $Sr_{2-x}La_xIrO_4$. *Phys. Rev. Lett.*, 117:107001, Sep 2016. 1, 67

[10] S. G. Chiuzbăian, G. Ghiringhelli, C. Dallera, M. Grioni, P. Amann, X. Wang, L. Braicovich, and L. Patthey. Localized electronic excitations in NiO studied with resonant inelastic x-ray scattering at the Ni M threshold: Evidence of spin flip. *Phys. Rev. Lett.*, 95:197402, Oct 2005. 1

[11] Valentina Bisogni, Sara Catalano, Robert J. Green, Marta Gibert, Raoul Scherwitzl, Yaobo Huang, Vladimir N. Strocov, Pavlo Zubko, Shadi Balandeh, Jean-Marc Triscone, George Sawatzky, and Thorsten Schmitt. Ground-state oxygen holes and the metal-insulator transition in the negative charge-transfer

rare-earth nickelates. *Nature Communications*, 7:13017 EP –, Oct 2016. Article. 1

[12] K. Fürsich, Y. Lu, D. Betto, M. Bluschke, J. Porras, E. Schierle, R. Ortiz, H. Suzuki, G. Cristiani, G. Logvenov, N. B. Brookes, M. W. Haverkort, M. Le Tacon, E. Benckiser, M. Minola, and B. Keimer. Resonant inelastic x-ray scattering study of bond order and spin excitations in nickelate thin-film structures. *Phys. Rev. B*, 99:165124, Apr 2019. 1

[13] Y. Lu, D. Betto, K. Fürsich, H. Suzuki, H.-H. Kim, G. Cristiani, G. Logvenov, N. B. Brookes, E. Benckiser, M. W. Haverkort, G. Khaliullin, M. Le Tacon, M. Minola, and B. Keimer. Site-selective probe of magnetic excitations in rare-earth nickelates using resonant inelastic x-ray scattering. *Phys. Rev. X*, 8:031014, Jul 2018. 1

[14] C. G. Fatuzzo, M. Dantz, S. Fatale, P. Olalde-Velasco, N. E. Shaik, B. Dalla Piazza, S. Toth, J. Pelliciari, R. Fittipaldi, A. Vecchione, N. Kikugawa, J. S. Brooks, H. M. Rønnow, M. Grioni, Ch. Rüegg, T. Schmitt, and J. Chang. Spin-orbit-induced orbital excitations in Sr_2RuO_4 and Ca_2RuO_4: A resonant inelastic x-ray scattering study. *Phys. Rev. B*, 91:155104, Apr 2015. 1

[15] B. J. Kim and Giniyat Khaliullin. Resonant inelastic x-ray scattering operators for t_{2g} orbital systems. *Phys. Rev. B*, 96:085108, Aug 2017. 1

[16] L. Das, F. Forte, R. Fittipaldi, C. G. Fatuzzo, V. Granata, O. Ivashko, M. Horio, F. Schindler, M. Dantz, Yi Tseng, D. E. McNally, H. M. Rønnow, W. Wan, N. B. Christensen, J. Pelliciari, P. Olalde-Velasco, N. Kikugawa, T. Neupert, A. Vecchione, T. Schmitt, M. Cuoco, and J. Chang. Spin-orbital excitations in Ca_2RuO_4 revealed by resonant inelastic x-ray scattering. *Phys. Rev. X*, 8:011048, Mar 2018. 1

[17] H. Suzuki, H. Gretarsson, H. Ishikawa, K. Ueda, Z. Yang, H. Liu, H. Kim, D. Kukusta, A. Yaresko, M. Minola, J. A. Sears, S. Francoual, H.-C. Wille, J. Nuss, H. Takagi, B. J. Kim, G. Khaliullin, H. Yavas, and B. Keimer. Spin waves and spin-state transitions in a ruthenate high-temperature antiferromagnet. *Nature Materials*, 18(6):563–567, 2019. 1

[18] J. G. Bednorz and K. A. Müller. Possible high-T_c superconductivity in the balacuo system. *Zeitschrift für Physik B Condensed Matter*, 64(2):189–193, Jun 1986. 1

[19] Masatomo Uehara, Takashi Nagata, Jun Akimitsu, Hiroki Takahashi, Nobuo Mri, and Kyoichi Kinoshita. Superconductivity in the ladder material $Sr_{0.4}Ca_{13.6}Cu24O_{41.84}$. *Journal of the Physical Society of Japan*, 65(9):2764–2767, 1996. 1, 10, 66

[20] Gerald D. Mahan. *Exactly Solvable Models*, pages 187–294. Springer US, Boston, MA, 2000. 2

[21] J. M. Luttinger. An exactly soluble model of a manyfermion system. *Journal of Mathematical Physics*, 4(9):1154–1162, 1963. 2

[22] C. Kim, A. Y. Matsuura, Z.-X. Shen, N. Motoyama, H. Eisaki, S. Uchida, T. Tohyama, and S. Maekawa. Observation of spin-charge separation in one-dimensional $SrCuO_2$. *Phys. Rev. Lett.*, 77:4054–4057, Nov 1996. 2, 47, 52

[23] B. J. Kim, H. Koh, E. Rotenberg, S.-J. Oh, H. Eisaki, N. Motoyama, S. Uchida, T. Tohyama, S. Maekawa, Z.-X. Shen, and C. Kim. Distinct spinon and holon dispersions in photoemission spectral functions from one-dimensional $SrCuO_2$. *Nat Phys*, 2(6):397–401, Jun 2006. 2, 4, 47, 52

[24] J. van den Brink, W. Stekelenburg, D. I. Khomskii, G. A. Sawatzky, and K. I. Kugel. Elementary excitations in the coupled spin-orbital model. *Phys. Rev. B*, 58:10276–10282, Oct 1998. 2

[25] H. F. Pen, J. van den Brink, D. I. Khomskii, and G. A. Sawatzky. Orbital ordering in a two-dimensional triangular lattice. *Phys. Rev. Lett.*, 78:1323–1326, Feb 1997. 2

[26] Pengcheng Dai, H. A. Mook, S. M. Hayden, G. Aeppli, T. G. Perring, R. D. Hunt, and F. Doğan. The magnetic excitation spectrum and thermodynamics of high-T_c superconductors. *Science*, 284(5418):1344–1347, 1999. 2

[27] D.J. Scalapino. The case for $d_{x^2-y^2}$ pairing in the cuprate superconductors. *Physics Reports*, 250(6):329 – 365, 1995. 2

[28] W. S. Lee, J. J. Lee, E. A. Nowadnick, S. Gerber, W. Tabis, S. W. Huang, V. N. Strocov, E. M. Motoyama, G. Yu, B. Moritz, H. Y. Huang, R. P. Wang, Y. B. Huang, W. B. Wu, C. T. Chen, D. J. Huang, M. Greven, T. Schmitt, Z. X. Shen, and T. P. Devereaux. Asymmetry of collective excitations in electron- and hole-doped cuprate superconductors. *Nature Physics*, 10:883 EP –, Oct 2014. Article. 2, 3, 30, 66

[29] Luuk J. P. Ament, Giacomo Ghiringhelli, Marco Moretti Sala, Lucio Braicovich, and Jeroen van den Brink. Theoretical demonstration of how the dispersion of magnetic excitations in cuprate compounds can be determined using resonant inelastic x-ray scattering. *Phys. Rev. Lett.*, 103:117003, Sep 2009. 2, 30, 42, 47, 66, 94

[30] M. Le Tacon, G. Ghiringhelli, J. Chaloupka, M. Moretti Sala, V. Hinkov, M. W. Haverkort, M. Minola, M. Bakr, K. J. Zhou, S. Blanco-Canosa, C. Monney, Y. T. Song, G. L. Sun, C. T. Lin, G. M. De Luca, M. Salluzzo, G. Khaliullin, T. Schmitt, L. Braicovich, and B. Keimer. Intense paramagnon excitations in a large family of high-temperature superconductors. *Nature Physics*, 7:725, Jul 2011. 2, 30, 66, 81

[31] Matthias Vojta. Magnetic fluctuations revealed. *Nature Physics*, 7:674 EP –, Sep 2011. 2

[32] C. J. Jia, E. A. Nowadnick, K. Wohlfeld, Y. F. Kung, C.-C. Chen, S. Johnston, T. Tohyama, B. Moritz, and T. P. Devereaux. Persistent spin excitations in doped antiferromagnets revealed by resonant inelastic light scattering. *Nature Communications*, 5:3314, Feb 2014. 2, 4, 66, 76, 81

[33] M. Minola, G. Dellea, H. Gretarsson, Y. Y. Peng, Y. Lu, J. Porras, T. Loew, F. Yakhou, N. B. Brookes, Y. B. Huang, J. Pelliciari, T. Schmitt, G. Ghiringhelli, B. Keimer, L. Braicovich, and M. Le Tacon. Collective nature of spin excitations in superconducting cuprates probed by resonant inelastic x-ray scattering. *Phys. Rev. Lett.*, 114:217003, May 2015. 2, 4, 66, 81

[34] H. Y. Huang, C. J. Jia, Z. Y. Chen, K. Wohlfeld, B. Moritz, T. P. Devereaux, W. B. Wu, J. Okamoto, W. S. Lee, M. Hashimoto, Y. He, Z. X. Shen, Y. Yoshida, H. Eisaki, C. Y. Mou, C. T. Chen, and D. J. Huang. Raman and fluorescence characteristics of resonant inelastic x-ray scattering from doped superconducting cuprates. *Scientific Reports*, 6:19657, Jan 2016. 2, 66, 81

[35] Y. F. Kung, E. A. Nowadnick, C. J. Jia, S. Johnston, B. Moritz, R. T. Scalettar, and T. P. Devereaux. Doping evolution of spin and charge excitations in the Hubbard model. *Phys. Rev. B*, 92:195108, Nov 2015. 4

[36] David Benjamin, Israel Klich, and Eugene Demler. Single-band model of resonant inelastic x-ray scattering by quasiparticles in high-T_c cuprate superconductors. *Phys. Rev. Lett.*, 112:247002, Jun 2014. 4, 87

[37] M. Kanász-Nagy, Y. Shi, I. Klich, and E. A. Demler. Resonant inelastic x-ray scattering as a probe of band structure effects in cuprates. *Phys. Rev. B*, 94:165127, Oct 2016. 4, 87

[38] M. Guarise, B. Dalla Piazza, H. Berger, E. Giannini, T. Schmitt, H. M. Rønnow, G. A. Sawatzky, J. van den Brink, D. Altenfeld, I. Eremin, and M. Grioni. Anisotropic softening of magnetic excitations along the nodal direction in superconducting cuprates. *Nature Communications*, 5:5760 EP –, Dec 2014. Article. 4

[39] M. Kang, J. Pelliciari, Y. Krockenberger, J. Li, D. E. McNally, E. Paris, R. Liang, W. N. Hardy, D. A. Bonn, H. Yamamoto, T. Schmitt, and R. Comin. Resolving the nature of electronic excitations in resonant inelastic x-ray scattering. *Phys. Rev. B*, 99:045105, Jan 2019. 4

[40] B. Dalla Piazza, M. Mourigal, N. B. Christensen, G. J. Nilsen, P. Tregenna-Piggott, T. G. Perring, M. Enderle, D. F. McMorrow, D. A. Ivanov, and H. M. Rønnow. Fractional excitations in the square-lattice quantum antiferromagnet. *Nature Physics*, 11:62 EP –, Dec 2014. Article. 4

[41] Martin Mourigal, Mechthild Enderle, Axel Klöpperpieper, Jean-Sébastien Caux, Anne Stunault, and Henrik M. Rønnow. Fractional spinon excitations in the quantum Heisenberg antiferromagnetic chain. *Nature Physics*, 9:435 EP –, Jun 2013. Article. 4, 10, 28, 29, 42, 65

[42] Roger S. Eccleston, Masatomo Uehara, Jun Akimitsu, Hiroshi Eisaki, Naoki Motoyama, and Shin-ichi Uchida. Spin dynamics of the spin-ladder dimer-chain material $Sr_{14}Cu_{24}O_{41}$. *Phys. Rev. Lett.*, 81:1702–1705, Aug 1998. 4, 8, 10, 65, 66, 69, 97

[43] R. Neudert, S.-L. Drechsler, J. Málek, H. Rosner, M. Kielwein, Z. Hu, M. Knupfer, M. S. Golden, J. Fink, N. Nücker, M. Merz, S. Schuppler, N. Motoyama, H. Eisaki, S. Uchida, M. Domke, and G. Kaindl. Four-band extended Hubbard Hamiltonian for the one-dimensional cuprate Sr_2CuO_3 distribution of oxygen holes and its relation to strong intersite coulomb interaction. *Phys. Rev. B*, 62:10752–10765, Oct 2000. 5, 6, 48

[44] Sebastian Eggert. Accurate determination of the exchange constant in Sr_2CuO_3 from recent theoretical results. *Phys. Rev. B*, 53:5116–5118, Mar 1996. 5

[45] N. Motoyama, H. Eisaki, and S. Uchida. Magnetic susceptibility of ideal spin-1/2 Heisenberg antiferromagnetic chain systems, Sr_2CuO_3 and $SrCuO_2$. *Phys. Rev. Lett.*, 76:3212–3215, Apr 1996. 5

[46] Andrew C. Walters, Toby G. Perring, Jean-Sebastien Caux, Andrei T. Savici, Genda D. Gu, Chi-Cheng Lee, Wei Ku, and Igor A. Zaliznyak. Effect of covalent bonding on magnetism and the missing neutron intensity in copper oxide compounds. *Nat Phys*, 5(12):867–872, Dec 2009. 5, 28, 34, 36, 48, 52

[47] I. A. Zaliznyak, H. Woo, T. G. Perring, C. L. Broholm, C. D. Frost, and H. Takagi. Spinons in the strongly correlated copper oxide chains in $SrCuO_2$. *Phys. Rev. Lett.*, 93:087202, Aug 2004. 5

[48] H. Fujisawa, T. Yokoya, T. Takahashi, S. Miyasaka, M. Kibune, and H. Takagi. Angle-resolved photoemission study of Sr_2CuO_3. *Phys. Rev. B*, 59:7358–7361, Mar 1999. 5, 47, 52

[49] Dalila Bounoua, Romuald Saint-Martin, Ji Dai, Tobias Rdel, Shamashis Sengupta, Emmanouil Frantzeskakis, Franois Bertran, Patrick Lefevre, Franck Fortuna, Andrs F. Santander-Syro, and Loreynne Pinsard-Gaudart. Angle resolved photoemission spectroscopy study of the spin-charge separation in the strongly correlated cuprates $SrCuO_2$ and Sr_2CuO_3 with $S = 0$ impurities. *Journal of Electron Spectroscopy and Related Phenomena*, 225:49 – 54, 2018. 5, 8

[50] Kozo Okada and Akio Kotani. Copper K and oxygen K resonant inelastic x-ray scattering of one-dimensional cuprates. *Journal of the Physical Society of Japan*, 75(4):044702, 2006. 5

[51] J. Richter, C. Waidacher, and K. W. Becker. Role of Zhang-Rice singletlike excitations in one-dimensional cuprates. *Phys. Rev. B*, 61:9871–9874, Apr 2000. 5

[52] D. S. Ellis, J. P. Hill, S. Wakimoto, R. J. Birgeneau, D. Casa, T. Gog, and Young-June Kim. Charge-transfer exciton in La_2CuO_4 probed with resonant inelastic x-ray scattering. *Phys. Rev. B*, 77:060501, Feb 2008. 5

[53] Koushik Karmakar, Rabindranath Bag, and Surjeet Singh. Crystal growth of spin chain compound Sr_2CuO_3 doped with quantum defects: Zn, Co, Ni, and Mn. *Crystal Growth & Design*, 15(10):4843–4853, 2015. 8, 47, 64, 99

[54] Koushik Karmakar, Rabindranath Bag, Markos Skoulatos, Christian Rüegg, and Surjeet Singh. Impurities in the weakly coupled quantum spin chains Sr_2CuO_3 and $SrCuO_2$. *Phys. Rev. B*, 95:235154, Jun 2017. 8, 47, 64, 99

[55] K.M Kojima, N Motoyama, H Eisaki, and S Uchida. The electronic properties of cuprate ladder materials. *Journal of Electron Spectroscopy and Related Phenomena*, 117-118:237 – 250, 2001. Strongly correlated systems. 9

[56] S. Notbohm, P. Ribeiro, B. Lake, D. A. Tennant, K. P. Schmidt, G. S. Uhrig, C. Hess, R. Klingeler, G. Behr, B. Büchner, M. Reehuis, R. I. Bewley, C. D. Frost, P. Manuel, and R. S. Eccleston. One- and two-triplon spectra of a cuprate ladder. *Phys. Rev. Lett.*, 98:027403, Jan 2007. 8, 66, 69, 74, 94

[57] J. Schlappa, U. Kumar, K. J. Zhou, S. Singh, M. Mourigal, V. N. Strocov, A. Revcolevschi, L. Patthey, H. M. Rønnow, S. Johnston, and T. Schmitt. Probing multi-spinon excitations outside of the two-spinon continuum in the antiferromagnetic spin chain cuprate Sr_2CuO_3. *Nature Communications*, 9:5394, 2018. 10, 14, 22, 27, 47, 48, 50, 52, 53, 56, 64, 65, 66, 82

[58] Steven R. White and D. J. Scalapino. Stripes on a 6-leg Hubbard ladder. *Phys. Rev. Lett.*, 91:136403, Sep 2003. 10, 65

[59] Tatsuya Nagao and Jun-ichi Igarashi. Theory of L-edge resonant inelastic x-ray scattering for magnetic excitations in two-leg spin ladders. *Phys. Rev. B*, 85:224436, Jun 2012. 10, 65, 67, 73, 94

[60] D. Schmidiger, P. Bouillot, S. Mühlbauer, S. Gvasaliya, C. Kollath, T. Giamarchi, and A. Zheludev. Spectral and thermodynamic properties of a strong-leg quantum spin ladder. *Phys. Rev. Lett.*, 108:167201, Apr 2012. 10, 65

[61] M. Jeong, H. Mayaffre, C. Berthier, D. Schmidiger, A. Zheludev, and M. Horvatić. Magnetic-order crossover in coupled spin ladders. *Phys. Rev. Lett.*, 118:167206, Apr 2017. 10, 65

[62] D. Schmidiger, S. Mühlbauer, A. Zheludev, P. Bouillot, T. Giamarchi, C. Kollath, G. Ehlers, and A. M. Tsvelik. Symmetric and asymmetric excitations of a strong-leg quantum spin ladder. *Phys. Rev. B*, 88:094411, Sep 2013. 10, 65, 75, 76, 95

[63] B. Thielemann, Ch. Rüegg, H. M. Rønnow, A. M. Läuchli, J.-S. Caux, B. Normand, D. Biner, K. W. Krämer, H.-U. Güdel, J. Stahn, K. Habicht, K. Kiefer, M. Boehm, D. F. McMorrow, and J. Mesot. Direct observation of magnon fractionalization in the quantum spin ladder. *Phys. Rev. Lett.*, 102:107204, Mar 2009. 10, 65

[64] M. Matsuda, K. Katsumata, R. S. Eccleston, S. Brehmer, and H.-J. Mikeska. Magnetic excitations and exchange interactions in the spin-$\frac{1}{2}$ two-leg ladder compound $La_6Ca_8Cu_{24}O_{41}$. *Phys. Rev. B*, 62:8903–8908, Oct 2000. 10, 65, 69

[65] J. E. Lorenzo, L. P. Regnault, C. Boullier, N. Martin, A. H. Moudden, S. Vanishri, C. Marin, and A. Revcolevschi. Macroscopic quantum coherence of the spin triplet in the spin-ladder compound $Sr_{14}Cu_{24}O_{41}$. *Phys. Rev. Lett.*, 105:097202, Aug 2010. 10, 65

[66] G. Deng, N. Tsyrulin, P. Bourges, D. Lamago, H. Ronnow, M. Kenzelmann, S. Danilkin, E. Pomjakushina, and K. Conder. Spin-gap evolution upon ca doping in the spin-ladder series $Sr_{14-x}Ca_xCu_{24}O_{41}$ studied by inelastic neutron scattering. *Phys. Rev. B*, 88:014504, Jul 2013. 10, 65

[67] A. T. Savici, G. E. Granroth, C. L. Broholm, D. M. Pajerowski, C. M. Brown, D. R. Talham, M. W. Meisel, K. P. Schmidt, G. S. Uhrig, and S. E. Nagler. Neutron scattering evidence for isolated spin-$\frac{1}{2}$ ladders in $(C_5D_{12}N)_2CuBr_4$. *Phys. Rev. B*, 80:094411, Sep 2009. 10, 65

[68] J. E. Lorenzo, L. P. Regnault, C. Boullier, N. Martin, S. Vanishri, and C. Marin. Magnetic chirality of the spin triplet in the spin-ladder compound $Sr_{14}Cu_{24}O_{41}$ as seen via polarized inelastic neutron scattering. *Phys. Rev. B*, 83:140413, Apr 2011. 10, 65

[69] Tao Hong, K. P. Schmidt, K. Coester, F. F. Awwadi, M. M. Turnbull, Y. Qiu, J. A. Rodriguez-Rivera, M. Zhu, X. Ke, C. P. Aoyama, Y. Takano, Huibo Cao, W. Tian, J. Ma, R. Custelcean, H. D. Zhou, and M. Matsuda. Magnetic ordering induced by interladder coupling in the spin-$\frac{1}{2}$ Heisenberg two-leg ladder antiferromagnet $C_9H_{18}N_2CuBr_4$. *Phys. Rev. B*, 89:174432, May 2014. 10, 65

[70] Bella Lake, Alexei M. Tsvelik, Susanne Notbohm, D. Alan Tennant, Toby G. Perring, Manfred Reehuis, Chinnathambi Sekar, Gernot Krabbes, and Bernd Büchner. Confinement of fractional quantum number particles in a condensed-matter system. *Nature Physics*, 6:50, Nov 2009. 10, 28, 65, 66, 74

[71] A. Nocera, Y. Wang, N. D. Patel, G. Alvarez, T. A. Maier, E. Dagotto, and S. Johnston. Doping evolution of charge and spin excitations in two-leg Hubbard ladders: Comparing dmrg and flex results. *Phys. Rev. B*, 97:195156, May 2018. 10, 65, 87

[72] E. Dagotto, J. Riera, and D. Scalapino. Superconductivity in ladders and coupled planes. *Phys. Rev. B*, 45:5744–5747, Mar 1992. 10, 66, 73, 75

[73] Valentina Bisogni, Krzysztof Wohlfeld, Satoshi Nishimoto, Claude Monney, Jan Trinckauf, Kejin Zhou, Roberto Kraus, Klaus Koepernik, Chinnathambi Sekar, Vladimir Strocov, Bernd Büchner, Thorsten Schmitt, Jeroen van den Brink, and Jochen Geck. Orbital control of effective dimensionality: From spin-orbital fractionalization to confinement in the anisotropic ladder system $CaCu_2O_3$. *Phys. Rev. Lett.*, 114:096402, Mar 2015. 10, 67, 69

[74] Valentina Bisogni, Stefanos Kourtis, Claude Monney, Kejin Zhou, Roberto Kraus, Chinnathambi Sekar, Vladimir Strocov, Bernd Büchner, Jeroen van den Brink, Lucio Braicovich, Thorsten Schmitt, Maria Daghofer, and Jochen Geck. Femtosecond dynamics of momentum-dependent magnetic excitations from resonant inelastic x-ray scattering in $CaCu_2O_3$. *Phys. Rev. Lett.*, 112:147401, Apr 2014. 10, 67, 71, 76, 82, 96, 99

[75] Luuk J. P. Ament. *Ph.D. thesis, Univeriteit Leiden, Netherlands*, 2010. 15, 48, 133

[76] J. J. Sakurai and Jim Napolitano. *Modern quantum mechanics.* Pearson, Essex (England), 2014. 16

[77] Michel van Veenendaal. Polarization dependence of L- and M-edge resonant inelastic x-ray scattering in transition-metal compounds. *Phys. Rev. Lett.*, 96:117404, Mar 2006. 19

[78] Michel van Veenendaal, Xiaosong Liu, Matthew H. Carpenter, and Stephen P. Cramer. Observation of dd excitations in NiO and $NiCl_2$ using K-edge resonant inelastic x-ray scattering. *Phys. Rev. B*, 83:045101, Jan 2011. 19

[79] K. Ishii, S. Ishihara, Y. Murakami, K. Ikeuchi, K. Kuzushita, T. Inami, K. Ohwada, M. Yoshida, I. Jarrige, N. Tatami, S. Niioka, D. Bizen, Y. Ando,

J. Mizuki, S. Maekawa, and Y. Endoh. Polarization-analyzed resonant inelastic x-ray scattering of the orbital excitations in $KCuF_3$. *Phys. Rev. B*, 83:241101, Jun 2011. 19

[80] R. Fumagalli, L. Braicovich, M. Minola, Y. Y. Peng, K. Kummer, D. Betto, M. Rossi, E. Lefrançois, C. Morawe, M. Salluzzo, H. Suzuki, F. Yakhou, M. Le Tacon, B. Keimer, N. B. Brookes, M. Moretti Sala, and G. Ghiringhelli. Polarization-resolved Cu L_3-edge resonant inelastic x-ray scattering of orbital and spin excitations in $\mathrm{ndba_2cu_3o_{7-\delta}}$. *Phys. Rev. B*, 99:134517, Apr 2019. 19

[81] N. V. Smith, C. T. Chen, F. Sette, and L. F. Mattheiss. Relativistic tight-binding calculations of x-ray absorption and magnetic circular dichroism at the L_2 and L_3 edges of nickel and iron. *Phys. Rev. B*, 46:1023–1032, Jul 1992. 19

[82] F. M. F. de Groot, P. Kuiper, and G. A. Sawatzky. Local spin-flip spectral distribution obtained by resonant x-ray Raman scattering. *Phys. Rev. B*, 57:14584–14587, Jun 1998. 19

[83] R. B. Lehoucq, D. C. Sorensen, and C. Yang. Arpack users guide: Solution of large scale eigenvalue problems by implicitly restarted arnoldi methods. 1997. 20

[84] A. Nocera, U. Kumar, N. Kaushal, G. Alvarez, E. Dagotto, and S. Johnston. Computing resonant inelastic x-ray scattering spectra using the density matrix renormalization group method. *Scientific Reports*, 8(1):11080, July 2018. 22, 32, 38, 67, 71, 94, 100

[85] Steven R. White. Density matrix formulation for quantum renormalization groups. *Phys. Rev. Lett.*, 69:2863–2866, Nov 1992. 22, 47, 52

[86] Steven R. White. Density-matrix algorithms for quantum renormalization groups. *Phys. Rev. B*, 48:10345–10356, Oct 1993. 22, 47, 52

[87] Steven R. White and Adrian E. Feiguin. Real-time evolution using the density matrix renormalization group. *Phys. Rev. Lett.*, 93:076401, Aug 2004. 22, 24

[88] Filomena Forte, Mario Cuoco, Canio Noce, and Jeroen van den Brink. Doping dependence of magnetic excitations of one-dimensional cuprates as probed by resonant inelastic x-ray scattering. *Phys. Rev. B*, 83:245133, Jun 2011. 22, 28, 29, 41, 42, 48, 66, 82

[89] Kozo Okada and Akio Kotani. Zhang-rice singlet-state formation by oxygen $1s$ resonant x-ray emission in edge-sharing copper-oxide systems. *Phys. Rev. B*, 63:045103, Jan 2001. 22

[90] Stefanos Kourtis, Jeroen van den Brink, and Maria Daghofer. Exact diagonalization results for resonant inelastic x-ray scattering spectra of one-dimensional mott insulators. *Phys. Rev. B*, 85:064423, Feb 2012. 22, 28, 48, 60, 63, 66, 71, 84, 96, 99

[91] K. Ishii, K. Tsutsui, Y. Endoh, T. Tohyama, S. Maekawa, M. Hoesch, K. Kuzushita, M. Tsubota, T. Inami, J. Mizuki, Y. Murakami, and K. Yamada. Momentum dependence of charge excitations in the electron-doped superconductor $\mathrm{Nd_{1.85}Ce_{0.15}CuO_4}$: A resonant inelastic x-ray scattering study. *Phys. Rev. Lett.*, 94:207003, May 2005. 22

[92] Kenji Tsutsui, Takami Tohyama, and Sadamichi Maekawa. Mott gap excitations and resonant inelastic x-ray scattering in doped cuprates. *Phys. Rev. Lett.*, 91:117001, Sep 2003. 22

[93] R. O. Kuzian, S. Nishimoto, S.-L. Drechsler, J. Málek, S. Johnston, Jeroen van den Brink, M. Schmitt, H. Rosner, M. Matsuda, K. Oka, H. Yamaguchi, and T. Ito. $\mathrm{Ca_2Y_2Cu_5O_{10}}$: The first frustrated quasi-1D ferromagnet close to criticality. *Phys. Rev. Lett.*, 109:117207, Sep 2012. 22

[94] Steve Johnston, Claude Monney, Valentina Bisogni, Ke-Jin Zhou, Roberto Kraus, Günter Behr, Vladimir N. Strocov, Jiri Málek, Stefan-Ludwig Drechsler, Jochen Geck, Thorsten Schmitt, and Jeroen van den Brink. Electron-lattice interactions strongly renormalize the charge-transfer energy in the spin-chain cuprate Li_2CuO_2. *Nature Communications*, 7:10563 EP –, Feb 2016. Article. 22, 28, 30, 32, 35

[95] F. Vernay, B. Moritz, I. S. Elfimov, J. Geck, D. Hawthorn, T. P. Devereaux, and G. A. Sawatzky. Cu K-edge resonant inelastic x-ray scattering in edge-sharing cuprates. *Phys. Rev. B*, 77:104519, Mar 2008. 22

[96] Krzysztof Wohlfeld, Satoshi Nishimoto, Maurits W. Haverkort, and Jeroen van den Brink. Microscopic origin of spin-orbital separation in Sr_2CuO_3. *Phys. Rev. B*, 88:195138, Nov 2013. 22, 28, 32, 34, 35, 47

[97] Umesh Kumar, Alberto Nocera, Elbio Dagotto, and Steve Johnston. Multi-spinon and antiholon excitations probed by resonant inelastic x-ray scattering on doped one-dimensional antiferromagnets. *New Journal of Physics*, 20(7):073019, 2018. 22, 46, 66, 76, 82, 87

[98] A. Nocera and G. Alvarez. Spectral functions with the density matrix renormalization group: Krylov-space approach for correction vectors. *Phys. Rev. E*, 94:053308, Nov 2016. 24, 25

[99] D. Alan Tennant, Roger A. Cowley, Stephen E. Nagler, and Alexei M. Tsvelik. Measurement of the spin-excitation continuum in one-dimensional $KCuF_3$ using neutron scattering. *Phys. Rev. B*, 52:13368–13380, Nov 1995. 28

[100] D. A. Tennant, T. G. Perring, R. A. Cowley, and S. E. Nagler. Unbound spinons in the $S = 1/2$ antiferromagnetic chain $KCuF_3$. *Phys. Rev. Lett.*, 70:4003–4006, Jun 1993. 28

[101] H. Suzuura, H. Yasuhara, A. Furusaki, N. Nagaosa, and Y. Tokura. Singularities in optical spectra of quantum spin chains. *Phys. Rev. Lett.*, 76:2579–2582, Apr 1996. 28, 34

[102] S. Glawion, J. Heidler, M. W. Haverkort, L. C. Duda, T. Schmitt, V. N. Strocov, C. Monney, K. J. Zhou, A. Ruff, M. Sing, and R. Claessen. Two-spinon and orbital excitations of the spin-peierls system tiocl. *Phys. Rev. Lett.*, 107:107402, Sep 2011. 28, 30

[103] O. V. Misochko, S. Tajima, C. Urano, H. Eisaki, and S. Uchida. Raman-scattering evidence for free spinons in the one-dimensional spin-$\frac{1}{2}$ chains of Sr_2CuO_3 and $SrCuO_2$. *Phys. Rev. B*, 53:R14733–R14736, Jun 1996. 28

[104] B. Lake, D. A. Tennant, J.-S. Caux, T. Barthel, U. Schollwöck, S. E. Nagler, and C. D. Frost. Multispinon continua at zero and finite temperature in a near-ideal Heisenberg chain. *Phys. Rev. Lett.*, 111:137205, Sep 2013. 28, 29

[105] A. Nocera, N. D. Patel, J. Fernandez-Baca, E. Dagotto, and G. Alvarez. Magnetic excitation spectra of strongly correlated quasi-one-dimensional systems: Heisenberg versus Hubbard -like behavior. *Phys. Rev. B*, 94:205145, Nov 2016. 28

[106] M. Enderle, B. Fåk, H.-J. Mikeska, R. K. Kremer, A. Prokofiev, and W. Assmus. Two-spinon and four-spinon continuum in a frustrated ferromagnetic spin-1/2 chain. *Phys. Rev. Lett.*, 104:237207, Jun 2010. 28, 29

[107] S.-L. Drechsler, S. Nishimoto, R. O. Kuzian, J. Málek, W. E. A. Lorenz, J. Richter, J. van den Brink, M. Schmitt, and H. Rosner. Comment on "two-spinon and four-spinon continuum in a frustrated ferromagnetic spin-1/2 chain". *Phys. Rev. Lett.*, 106:219701, May 2011. 28, 29

[108] M. Enderle, B. Fåk, H.-J. Mikeska, and R.K. Kremer. Enderle et al. reply:. *Phys. Rev. Lett.*, 106:219702, May 2011. 28, 29

[109] Claude Monney, Valentina Bisogni, Ke-Jin Zhou, Roberto Kraus, Vladimir N. Strocov, Günter Behr, Ji ři Málek, Roman Kuzian, Stefan-Ludwig Drechsler, Steve Johnston, Alexandre Revcolevschi, Bernd Büchner, Henrik M. Rønnow, Jeroen van den Brink, Jochen Geck, and Thorsten Schmitt. Determining the short-range spin correlations in the spin-chain Li_2CuO_2 and $CuGeO_3$ compounds using resonant inelastic x-ray scattering. *Phys. Rev. Lett.*, 110:087403, Feb 2013. 28, 30, 32

[110] Michael Karbach, Gerhard Müller, A. Hamid Bougourzi, Andreas Fledderjohann, and Karl-Heinz Mütter. Two-spinon dynamic structure factor of the one-dimensional $S = 1/2$ Heisenberg antiferromagnet. *Phys. Rev. B*, 55:12510–12517, May 1997. 28, 29

[111] Jean-Sbastien Caux and Rob Hagemans. The four-spinon dynamical structure factor of the Heisenberg chain. *Journal of Statistical Mechanics: Theory and Experiment*, 2006(12):P12013, 2006. 28, 29, 36, 41, 56

[112] L. S. Wu, W. J. Gannon, I. A. Zaliznyak, A. M. Tsvelik, M. Brockmann, J.-S. Caux, M. S. Kim, Y. Qiu, J. R. D. Copley, G. Ehlers, A. Podlesnyak, and M. C. Aronson. Orbital-exchange and fractional quantum number excitations in an f-electron metal, Yb_2Pt_2Pb. *Science*, 352(6290):1206–1210, 2016. 29

[113] Chunjing Jia, Krzysztof Wohlfeld, Yao Wang, Brian Moritz, and Thomas P. Devereaux. Using rixs to uncover elementary charge and spin excitations. *Phys. Rev. X*, 6:021020, May 2016. 29, 76, 82, 85, 89, 92, 96, 99, 133, 134

[114] V. Bisogni, L. Simonelli, L. J. P. Ament, F. Forte, M. Moretti Sala, M. Minola, S. Huotari, J. van den Brink, G. Ghiringhelli, N. B. Brookes, and L. Braicovich. Bimagnon studies in cuprates with resonant inelastic x-ray scattering at the O K edge. I. assessment on La_2CuO_4 and comparison with the excitation at Cu L_3 and Cu K edges. *Phys. Rev. B*, 85:214527, Jun 2012. 30, 66, 82, 96, 99

[115] Y. Y. Peng, G. Dellea, M. Minola, M. Conni, A. Amorese, D. Di Castro, G. M. De Luca, K. Kummer, M. Salluzzo, X. Sun, X. J. Zhou, G. Balestrino, M. Le Tacon, B. Keimer, L. Braicovich, N. B. Brookes, and G. Ghiringhelli. Influence of apical oxygen on the extent of in-plane exchange interaction in cuprate superconductors. *Nature Physics*, 13:1201 EP –, Aug 2017. Article. 30

[116] L. Chaix, G. Ghiringhelli, Y. Y. Peng, M. Hashimoto, B. Moritz, K. Kummer, N. B. Brookes, Y. He, S. Chen, S. Ishida, Y. Yoshida, H. Eisaki, M. Salluzzo, L. Braicovich, Z.-X. Shen, T. P. Devereaux, and W.-S. Lee. Dispersive charge density wave excitations in $Bi_2Sr_2CaCu_2O_{8+d}$. *Nature Physics*, 13:952 EP –, Jun 2017. 30

[117] V. N. Strocov, T. Schmitt, U. Flechsig, T. Schmidt, A. Imhof, Q. Chen, J. Raabe, R. Betemps, D. Zimoch, J. Krempasky, X. Wang, M. Grioni, A. Piazzalunga, and L. Patthey. High-resolution soft X-ray beamline ADRESS at the Swiss Light Source for resonant inelastic X-ray scattering and angle-resolved photoelectron spectroscopies. *Journal of Synchrotron Radiation*, 17(5):631–643, Sep 2010. 31

[118] G. Ghiringhelli, A. Piazzalunga, C. Dallera, G. Trezzi, L. Braicovich, T. Schmitt, V. N. Strocov, R. Betemps, L. Patthey, X. Wang, and M. Grioni. Saxes, a high resolution spectrometer for resonant x-ray emission in the 4001600ev energy range. *Review of Scientific Instruments*, 77(11):113108, 2006. 31

[119] Faris Gel'mukhanov, Paweł Sałek, Timofei Privalov, and Hans Ågren. Duration of x-ray Raman scattering. *Phys. Rev. A*, 59:380–389, Jan 1999. 31, 43

[120] Mark S Golden, Christian Drr, Andreas Koitzsch, Sibylle Legner, Zhiwei Hu, Sergey Borisenko, Martin Knupfer, and Jrg Fink. The electronic structure of cuprates from high energy spectroscopy. *Journal of Electron Spectroscopy and*

Related Phenomena, 117-118:203 – 222, 2001. Strongly correlated systems. 32, 33, 34

[121] K. M. Kojima, Y. Fudamoto, M. Larkin, G. M. Luke, J. Merrin, B. Nachumi, Y. J. Uemura, N. Motoyama, H. Eisaki, S. Uchida, K. Yamada, Y. Endoh, S. Hosoya, B. J. Sternlieb, and G. Shirane. Reduction of ordered moment and néel temperature of quasi-one-dimensional antiferromagnets Sr_2CuO_3 and Ca_2CuO_3. *Phys. Rev. Lett.*, 78:1787–1790, Mar 1997. 34, 47

[122] Antoine Klauser, Jorn Mossel, Jean-Sébastien Caux, and Jeroen van den Brink. Spin-exchange dynamical structure factor of the $S = 1/2$ Heisenberg chain. *Phys. Rev. Lett.*, 106:157205, Apr 2011. 41, 42, 48, 63, 84, 92

[123] Xingye Lu, Paul Olalde-Velasco, Yaobo Huang, Valentina Bisogni, Jonathan Pelliciari, Sara Fatale, Marcus Dantz, James G. Vale, E. C. Hunter, Johan Chang, Vladimir N. Strocov, R. S. Perry, Marco Grioni, D. F. McMorrow, Henrik M. Rønnow, and Thorsten Schmitt. Dispersive magnetic and electronic excitations in iridate perovskites probed by oxygen K-edge resonant inelastic x-ray scattering. *Phys. Rev. B*, 97:041102, Jan 2018. 41, 66

[124] Filomena Forte, Luuk J. P. Ament, and Jeroen van den Brink. Magnetic excitations in La_2CuO_4 probed by indirect resonant inelastic x-ray scattering. *Phys. Rev. B*, 77:134428, Apr 2008. 41, 84, 89, 92, 133

[125] Elliott H. Lieb and F. Y. Wu. Absence of mott transition in an exact solution of the short-range, one-band model in one dimension. *Phys. Rev. Lett.*, 20:1445–1448, Jun 1968. 47, 76

[126] P. Segovia, D. Purdie, M. Hengsberger, and Y. Baer. Observation of spin and charge collective modes in one-dimensional metallic chains. *Nature*, 402(6761):504–507, Dec 1999. 47

[127] A. Koitzsch, S. V. Borisenko, J. Geck, V. B. Zabolotnyy, M. Knupfer, J. Fink, P. Ribeiro, B. Büchner, and R. Follath. Current spinon-holon description of the one-dimensional charge-transfer insulator $SrCuO_2$: Angle-resolved photoemission measurements. *Phys. Rev. B*, 73:201101, May 2006. 47

[128] Y. Jompol, C. J. B. Ford, J. P. Griffiths, I. Farrer, G. A. C. Jones, D. Anderson, D. A. Ritchie, T. W. Silk, and A. J. Schofield. Probing spin-charge separation in a Tomonaga-Luttinger liquid. *Science*, 325(5940):597–601, 2009. 47

[129] J. P. Hill, G. Blumberg, Young-June Kim, D. S. Ellis, S. Wakimoto, R. J. Birgeneau, Seiki Komiya, Yoichi Ando, B. Liang, R. L. Greene, D. Casa, and T. Gog. Observation of a 500 mev collective mode in $La_{2-x}Sr_xCuO_4$ and Nd_2CuO_4 using resonant inelastic x-ray scattering. *Phys. Rev. Lett.*, 100:097001, Mar 2008. 47

[130] M. P. M. Dean, A. J. A. James, R. S. Springell, X. Liu, C. Monney, K. J. Zhou, R. M. Konik, J. S. Wen, Z. J. Xu, G. D. Gu, V. N. Strocov, T. Schmitt, and J. P. Hill. High-energy magnetic excitations in the cuprate superconductor $Bi_2Sr_2CaCu_2O_{8+\delta}$: Towards a unified description of its electronic and magnetic degrees of freedom. *Phys. Rev. Lett.*, 110:147001, Apr 2013. 47

[131] W. S. Lee, S. Johnston, B. Moritz, J. Lee, M. Yi, K. J. Zhou, T. Schmitt, L. Patthey, V. Strocov, K. Kudo, Y. Koike, J. van den Brink, T. P. Devereaux, and Z. X. Shen. Role of lattice coupling in establishing electronic and magnetic properties in quasi-one-dimensional cuprates. *Phys. Rev. Lett.*, 110:265502, Jun 2013. 48, 52

[132] Jun-ichi Igarashi and Tatsuya Nagao. Magnetic excitations in l-edge resonant inelastic x-ray scattering from one-dimensional cuprates. *Phys. Rev. B*, 85:064422, Feb 2012. 48, 63, 99

[133] Takami Tohyama and Kenji Tsutsui. Spectral weight of resonant inelastic x-ray scattering in doped cuprates: Effect of core-hole lifetime. *International Journal of Modern Physics B*, 0(0):1840017, 0. 48

[134] Luuk J. P. Ament, Filomena Forte, and Jeroen van den Brink. Ultrashort lifetime expansion for indirect resonant inelastic x-ray scattering. *Phys. Rev. B*, 75:115118, Mar 2007. 48, 63, 134

[135] Henk Eskes and John H. Jefferson. Superexchange in the cuprates. *Phys. Rev. B*, 48:9788–9798, Oct 1993. 51

[136] Z. V. Popović, V. A. Ivanov, M. J. Konstantinović, A. Cantarero, J. Martínez-Pastor, D. Olguín, M. I. Alonso, M. Garriga, O. P. Khuong, A. Vietkin, and V. V. Moshchalkov. Optical studies of gap, hopping energies, and the Anderson-Hubbard parameter in the zigzag-chain compound $SrCuO_2$. *Phys. Rev. B*, 63:165105, Apr 2001. 52

[137] Till D. Kühner and Steven R. White. Dynamical correlation functions using the density matrix renormalization group. *Phys. Rev. B*, 60:335–343, Jul 1999. 52

[138] Eric Jeckelmann. Dynamical density-matrix renormalization-group method. *Phys. Rev. B*, 66:045114, Jul 2002. 52

[139] A. Nocera and G. Alvarez. Spectral functions with the density matrix renormalization group: Krylov-space approach for correction vectors. *Phys. Rev. E*, 94:053308, Nov 2016. 52

[140] G. Alvarez. The density matrix renormalization group for strongly correlated electron systems: A generic implementation. *Computer Physics Communications*, 180(9):1572 – 1578, 2009. 52

[141] Martin Mourigal, Mechthild Enderle, Axel Klopperpieper, Jean-Sebastien Caux, Anne Stunault, and Henrik M. Ronnow. Fractional spinon excitations in the quantum Heisenberg antiferromagnetic chain. *Nat Phys*, 9:435, 07 2013. 53

[142] Young-June Kim, J. P. Hill, H. Benthien, F. H. L. Essler, E. Jeckelmann, H. S. Choi, T. W. Noh, N. Motoyama, K. M. Kojima, S. Uchida, D. Casa, and T. Gog. Resonant inelastic x-ray scattering of the holon-antiholon continuum in $SrCuO_2$. *Phys. Rev. Lett.*, 92:137402, Apr 2004. 53

[143] F Woynarovich. Excitations with complex wavenumbers in a Hubbard chain. I. States with one pair of complex wavenumbers. *Journal of Physics C: Solid State Physics*, 15(1):85, 1982. 56

[144] Masao Ogata and Hiroyuki Shiba. Bethe-ansatz wave function, momentum distribution, and spin correlation in the one-dimensional strongly correlated Hubbard model. *Phys. Rev. B*, 41:2326–2338, Feb 1990. 56

[145] Karlo Penc, Karen Hallberg, Frédéric Mila, and Hiroyuki Shiba. Spectral functions of the one-dimensional Hubbard model in the $U \to +\infty$ limit: How to use the factorized wave function. *Phys. Rev. B*, 55:15475–15488, Jun 1997. 56

[146] S Sorella and A Parola. One-hole green function, momentum distribution and quasiparticle weight of the U to infinity 1D Hubbard model. *Journal of Physics: Condensed Matter*, 4(13):3589, 1992. 56

[147] C. Kim, Z.-X. Shen, N. Motoyama, H. Eisaki, S. Uchida, T. Tohyama, and S. Maekawa. Separation of spin and charge excitations in one-dimensional $SrCuO_2$. *Phys. Rev. B*, 56:15589–15595, Dec 1997. 56

[148] J. Deisz, K.-H. Luk, M. Jarrell, and D. L. Cox. Spin and charge dynamics for the one-dimensional $t - J$ model. *Phys. Rev. B*, 46:3410–3419, Aug 1992. 60

[149] G. Simutis, S. Gvasaliya, M. Månsson, A. L. Chernyshev, A. Mohan, S. Singh, C. Hess, A. T. Savici, A. I. Kolesnikov, A. Piovano, T. Perring, I. Zaliznyak, B. Büchner, and A. Zheludev. Spin pseudogap in ni-doped $SrCuO_2$. *Phys. Rev. Lett.*, 111:067204, Aug 2013. 64, 99

[150] Umesh Kumar, Alberto Nocera, Elbio Dagotto, and Steven Johnston. Theoretical study of the spin and charge dynamics of two-leg ladders as probed by resonant inelastic x-ray scattering. *Phys. Rev. B*, 99:205130, May 2019. 65

[151] Elbio Dagotto and T. M. Rice. Surprises on the way from one- to two-dimensional quantum magnets: The ladder materials. *Science*, 271(5249):618–623, 1996. 65

[152] V. Bisogni, M. Moretti Sala, A. Bendounan, N. B. Brookes, G. Ghiringhelli, and L. Braicovich. Bimagnon studies in cuprates with resonant inelastic x-ray scattering at the o K edge. II. doping effect in $La_{2-x}Sr_xCuO_4$. *Phys. Rev. B*, 85:214528, Jun 2012. 66

[153] A Higashiya, S Imada, T Murakawa, H Fujiwara, S Kasai, A Sekiyama, S Suga, K Okada, M Yabashi, K Tamasaku, T Ishikawa, and H Eisaki. Significance of the inter-site coulomb interaction between the O 2p and Cu 3d holes revealed by resonant inelastic x-ray scattering of $Sr_{14}Cu_{24}O_{41}$. *New Journal of Physics*, 10(5):053033, 2008. 67

[154] L. Wray, D. Qian, D. Hsieh, Y. Xia, H. Eisaki, and M. Z. Hasan. Dispersive collective charge modes in an incommensurately modulated cuprate mott insulator. *Phys. Rev. B*, 76:100507, Sep 2007. 67

[155] K. Ishii, K. Tsutsui, T. Tohyama, T. Inami, J. Mizuki, Y. Murakami, Y. Endoh, S. Maekawa, K. Kudo, Y. Koike, and K. Kumagai. Momentum-dependent charge excitations of a two-leg ladder: Resonant inelastic x-ray scattering of $(La, Sr, Ca)_{14}Cu_{24}O_{41}$. *Phys. Rev. B*, 76:045124, Jul 2007. 67

[156] Steven R. White. Density matrix formulation for quantum renormalization groups. *Phys. Rev. Lett.*, 69:2863–2866, Nov 1992. 67

[157] Steven R. White. Density-matrix algorithms for quantum renormalization groups. *Phys. Rev. B*, 48:10345–10356, Oct 1993. 67

[158] John H. Gruenewald, Jungho Kim, Heung Sik Kim, Jared M. Johnson, Jinwoo Hwang, Maryam Souri, Jasminka Terzic, Seo Hyoung Chang, Ayman Said, Joseph W. Brill, Gang Cao, Hae-Young Kee, and Sung S. Ambrose Seo. Engineering 1D quantum stripes from superlattices of 2D layered materials. *Advanced Materials*, 29(1):1603798, 2017. 67

[159] A. Gozar, G. Blumberg, B. S. Dennis, B. S. Shastry, N. Motoyama, H. Eisaki, and S. Uchida. Spin dynamics of $Sr_{14}Cu_{24}O_{41}$ two-leg ladder studied by Raman spectroscopy. *Phys. Rev. Lett.*, 87:197202, Oct 2001. 69

[160] Weihong Zheng, Chris J. Hamer, Rajiv R. P. Singh, Simon Trebst, and Hartmut Monien. Linked cluster series expansions for two-particle bound states. *Phys. Rev. B*, 63:144410, Mar 2001. 73, 74, 84

[161] Kai P. Schmidt and G. S. Uhrig. Spectral properties of magnetic excitations in cuprate two-leg ladder systems. *Modern Physics Letters B*, 19(24):1179–1205, 2005. 73, 77, 79, 83, 84

[162] Kai P. Schmidt and Götz S. Uhrig. Excitations in one-dimensional $S = \frac{1}{2}$ quantum antiferromagnets. *Phys. Rev. Lett.*, 90:227204, Jun 2003. 73

[163] T. Barnes, E. Dagotto, J. Riera, and E. S. Swanson. Excitation spectrum of Heisenberg spin ladders. *Phys. Rev. B*, 47:3196–3203, Feb 1993. 73

[164] Knetter, C., Schmidt, K. P., and Uhrig, G. S. High order perturbation theory for spectral densities of multi-particle excitations: $S = 1/2$ two-leg Heisenberg ladder. *Eur. Phys. J. B*, 36(4):525–544, 2003. 73

[165] O. P. Sushkov and V. N. Kotov. Bound states of magnons in the $S = 1/2$ quantum spin ladder. *Phys. Rev. Lett.*, 81:1941–1944, Aug 1998. 73

[166] M. Greven, R. J. Birgeneau, and U. J. Wiese. Monte carlo study of correlations in quantum spin ladders. *Phys. Rev. Lett.*, 77:1865–1868, Aug 1996. 74

[167] D. G. Shelton, A. A. Nersesyan, and A. M. Tsvelik. Antiferromagnetic spin ladders: Crossover between spin $S = 1/2$ and $S = 1$ chains. *Phys. Rev. B*, 53:8521–8532, Apr 1996. 75

[168] Matthias Troyer, Hirokazu Tsunetsugu, and T. M. Rice. Properties of lightly doped $t - J$ two-leg ladders. *Phys. Rev. B*, 53:251–267, Jan 1996. 75, 81, 85

[169] Shenxiu Liu, Hong-Chen Jiang, and Thomas P. Devereaux. Nature of a single doped hole in two-leg Hubbard and $t - J$ ladders. *Phys. Rev. B*, 94:155149, Oct 2016. 75, 76, 79

[170] S. R. White, D. J. Scalapino, and S. A. Kivelson. One hole in the two-leg $t{-}J$ ladder and adiabatic continuity to the noninteracting limit. *Phys. Rev. Lett.*, 115:056401, Jul 2015. 75

[171] N. J. Robinson, F. H. L. Essler, E. Jeckelmann, and A. M. Tsvelik. Finite wave vector pairing in doped two-leg ladders. *Phys. Rev. B*, 85:195103, May 2012. 75

[172] A. Nocera, N. D. Patel, E. Dagotto, and G. Alvarez. Signatures of pairing in the magnetic excitation spectrum of strongly correlated two-leg ladders. *Phys. Rev. B*, 96:205120, Nov 2017. 75, 81

[173] T. F. A. Müller and T. M. Rice. Phase diagram of coupled ladders. *Phys. Rev. B*, 58:3425–3437, Aug 1998. 81

[174] Takami Tohyama, Michiyasu Mori, and Shigetoshi Sota. Dynamical density matrix renormalization group study of spin and charge excitations in the four-leg $t-t^{'}-J$ ladder. *Phys. Rev. B*, 97:235137, Jun 2018. 81, 100

[175] J. M. Tranquada, H. Woo, T. G. Perring, H. Goka, G. D. Gu, G. Xu, M. Fujita, and K. Yamada. Quantum magnetic excitations from stripes in copper oxide superconductors. *Nature*, 429:534, Jun 2004. 81

[176] Guangyong Xu, G. D. Gu, M. Hücker, B. Fauqué, T. G. Perring, L. P. Regnault, and J. M. Tranquada. Testing the itinerancy of spin dynamics in superconducting $\mathrm{Bi_2Sr_2CaCu_2O_{8+d}}$. *Nature Physics*, 5:642, Aug 2009. 81

[177] J. van den Brink and M. van Veenendaal. Correlation functions measured by indirect resonant inelastic x-ray scattering. *EPL (Europhysics Letters)*, 73(1):121, 2006. 89

[178] Luuk J. P. Ament, Filomena Forte, and Jeroen van den Brink. Ultrashort lifetime expansion for indirect resonant inelastic x-ray scattering. *Phys. Rev. B*, 75:115118, Mar 2007. 89

[179] Andrei Catuneanu, Erik S. Sørensen, and Hae-Young Kee. Nonlocal string order parameter in the $S = \frac{1}{2}$ Kitaev-Heisenberg ladder. *Phys. Rev. B*, 99:195112, May 2019. 100

[180] Cliò Efthimia Agrapidis, Jeroen van den Brink, and Satoshi Nishimoto. Ground state and low-energy excitations of the Kitaev-Heisenberg two-leg ladder. *Phys. Rev. B*, 99:224418, Jun 2019. 100

[181] Yao Wang, Martin Claassen, Chaitanya Das Pemmaraju, Chunjing Jia, Brian Moritz, and Thomas P. Devereaux. Theoretical understanding of photon spectroscopies in correlated materials in and out of equilibrium. *Nature Reviews Materials*, 3(9):312–323, 2018. 100

[182] D. Fausti, R. I. Tobey, N. Dean, S. Kaiser, A. Dienst, M. C. Hoffmann, S. Pyon, T. Takayama, H. Takagi, and A. Cavalleri. Light-induced superconductivity in a stripe-ordered cuprate. *Science*, 331(6014):189–191, 2011. 100

Appendices

Appendix A

Dipole Matrix Elements for L-edge

We consider the transition of a hole (electron) in transition metal (TM) from $d \rightarrow p$ ($p \rightarrow d$) orbitals caused by an incoming photon. No spin-orbit splitting is considered in the d orbitals, whereas it is considered in core p-orbitals, which is usually the case for $3d$ TM atoms. The total angular momentum $|J, J_z\rangle$ is used as the basis for the p-orbitals, whereas, the d-orbitals can be written in terms of the spherical harmonics Y_2^m. The table is evaluated using spherical harmonics integration

$$\langle J, J_z|\boldsymbol{\varepsilon}\cdot\mathbf{r}|3d\rangle \propto \int Y_1^{m_1*}Y_1^{m}Y_2^{m_2}d\Omega. \tag{A.1}$$

The position vector of the electron is $\mathbf{r} = r_x\hat{e}_x + r_y\hat{e}_y + r_z\hat{e}_z$. The coefficients r_α for **linear polarization** in terms of spherical harmonics are given by
a) x-polarization, $r_x = \frac{1}{\sqrt{2}}\sqrt{\frac{4\pi}{3}}(Y_1^{\bar{1}} - Y_1^{1})$
b) y-polarization, $r_y = \frac{i}{\sqrt{2}}\sqrt{\frac{4\pi}{3}}(Y_1^{\bar{1}} + Y_1^{1})$
c) z-polarization, $r_z = \sqrt{\frac{4\pi}{3}}Y_1^{0}$.

Table A.1 shows the L-edge transition matrix elements corresponding excitation to core-hole excitation from $3d \rightarrow 2p$.

Table A.1: Dipole matrix elements for linearly polarized photon transitioning a hole ($3d \rightarrow 2p$) in L-edge RIXS.

	Pol.	$\lvert\frac{3}{2},\frac{3}{2}\rangle$	$\lvert\frac{3}{2},\frac{1}{2}\rangle$	$\lvert\frac{3}{2},\text{-}\frac{1}{2}\rangle$	$\lvert\frac{3}{2},\text{-}\frac{3}{2}\rangle$	$\lvert\frac{1}{2},\frac{1}{2}\rangle$	$\lvert\frac{1}{2},\text{-}\frac{1}{2}\rangle$
$d_{x^2-y^2}(\uparrow)$	x	$-\frac{\sqrt{6}}{2}$		$\frac{1}{\sqrt{2}}$			-1
	y	$-i\frac{\sqrt{6}}{2}$		$-i\frac{1}{\sqrt{2}}$			$-i$
	z						
$d_{x^2-y^2}(\downarrow)$	x		$-\frac{1}{\sqrt{2}}$		$\frac{\sqrt{6}}{2}$		
	y		$-\frac{i}{\sqrt{2}}$		$-i\frac{\sqrt{6}}{2}$	$-i$	
	z						
$d_{3z^2-r^2}(\uparrow)$	x	$\frac{1}{\sqrt{2}}$		$-\frac{1}{\sqrt{6}}$			$\frac{1}{\sqrt{3}}$
	y	$-\frac{i}{\sqrt{2}}$		$-\frac{i}{\sqrt{6}}$			$-\frac{i}{\sqrt{3}}$
	z		$\frac{4}{\sqrt{6}}$			$-\frac{2}{\sqrt{3}}$	
$d_{3z^2-r^2}(\downarrow)$	x		$\frac{1}{\sqrt{6}}$		$-\frac{1}{\sqrt{2}}$	$-\frac{1}{\sqrt{3}}$	
	y		$-\frac{i}{\sqrt{6}}$		$-\frac{i}{\sqrt{2}}$	$-\frac{i}{\sqrt{3}}$	
	z			$\frac{4}{\sqrt{6}}$			$-\frac{2}{\sqrt{3}}$
$d_{xy}(\uparrow)$	x	$i\frac{\sqrt{6}}{2}$		$\frac{i}{\sqrt{2}}$			
	y	$-\frac{\sqrt{6}}{2}$		$\frac{1}{\sqrt{2}}$			
	z						
$d_{xy}(\downarrow)$	x		$\frac{i}{\sqrt{2}}$		$i\frac{\sqrt{6}}{2}$		
	y		$-\frac{1}{\sqrt{2}}$		$\frac{\sqrt{6}}{2}$		
	z						
$d_{yz}(\uparrow)$	x						
	y		$-\sqrt{2}$				
	z	$-i\frac{\sqrt{6}}{2}$		$-\frac{i}{\sqrt{2}}$			
$d_{yz}(\downarrow)$	x						
	y			$-\sqrt{2}$			
	z		$-\frac{i}{\sqrt{2}}$		$-i\frac{\sqrt{6}}{2}$		
$d_{zx}(\uparrow)$	x		$-\sqrt{2}$				
	y						
	z	$\frac{\sqrt{6}}{2}$		$-\frac{1}{\sqrt{2}}$			
$d_{zx}(\downarrow)$	x			$-\sqrt{2}$			
	y						
	z		$\frac{1}{\sqrt{2}}$		$-\frac{\sqrt{6}}{2}$		

Appendix B

Ultrashort Core-hole Lifetime expansion

The complicated Kramers-Heisenberg formalism under ultrashort core-hole lifetime (UCL) expansion can be written in terms of simpler correlation functions, which further aid understanding of the RIXS spectra.

The RIXS scattering amplitude in terms of the Green's function is given by

$$\mathcal{F}_{fg} = \langle f|D^{\dagger}G(z_k)D|g\rangle. \tag{B.1}$$

Here $|g\rangle$ and $|f\rangle$ are the ground and final states of the system, D is the dipole transition operator, and $G(z_k)$ is a Green's function, which accounts for the intermediate-state propagator in the Kramers-Heisenberg formalism and is given by

$$G(z_k) = \frac{1}{z_k - \mathcal{H}} = \sum_N \frac{|N\rangle\langle N|}{z_k - E_N}. \tag{B.2}$$

Here, $|N\rangle$ are the eigenstates of intermediate state Hamiltonian $\mathcal{H}$ with energy E_N and $z_k = E_g + \hbar\omega_k + i\Gamma$.

Under the assumption that the bandwidth of the energies of the intermediate-state manifold are much smaller than the inverse core-hole lifetime Γ, the Green's function can be treated using UCL expansion. This is indeed true for the magnetic excitations at Cu L-edge of cuprates, where $\frac{J}{\Gamma} < 1$, which allows one to simplify Kramers-Heisenberg formalism into simpler correlation functions [75, 113, 124]. In this work, our model is motivated by the t-J model as introduced in various chapters in this thesis and we focus on spectra for the Cu L-edge as introduced in Chapter 5.

We start by investigating the spectral decomposed states of the intermediate Hamiltonian operator the RIXS formalism.

$$\frac{1}{\omega_{\text{in}} - \mathcal{H} + i\Gamma} = \sum_{|N\rangle} \frac{|N\rangle\langle N|}{\omega_{\text{in}} - E_N + i\Gamma} \tag{B.3}$$

We know that due to large U_c on the core-hole site, the hopping on that d-orbital is suppressed. This allows one to decompose the intermediate states- $|N\rangle$ into its valence band $|n\rangle$ and core-hole, $|n_c\rangle$ states as

$$|N\rangle = |n\rangle|n_c\rangle, \qquad E_N = E_n + E_c. \tag{B.4}$$

Then one can rewrite the Greens function as

$$\frac{1}{\omega_{\text{in}} - \mathcal{H} + i\Gamma} = \sum_{|n,n_c\rangle} \frac{|n\rangle|n_c\rangle\langle n_c|\langle n|}{\omega_{\text{in}} - E_n - E_c + i\Gamma} \tag{B.5}$$

Using the characteristic value of E_c, one can select the L_2 or L_3 edge. We will discuss our derivation in the context of the L_3 edge, though the discussion can be easily extented to L_2-edge by replacing L_2 by L_3 and considering the relevant approximations.

$$\frac{1}{\omega_{\text{in}} - \mathcal{H} + i\Gamma} = \sum_{|n\rangle} \frac{|n\rangle|L_3\rangle\langle L_3|\langle n|}{\omega_{\text{in}} - E_n - E_{L_3} + i\Gamma} \tag{B.6}$$

It is important to note that $|L_3\rangle$ can both flip or conserve the spin in core-hole and hence produce $\Delta S = 1$ (NSC) and $\Delta S = 0$ (SC) excitations respectively. Lets us define $\Delta = \omega_{\text{in}} - E_{L_3} \to 0$. Since E_c and E_{L_3} are eigenstates of independent states and $|n\rangle$ forms a complete set, one can write

$$\sum_{|n\rangle} \frac{|n\rangle|L_3\rangle\langle L_3|\langle n|}{\omega_{\text{in}} - E_n - E_{L_3} + i\Gamma} = |L_3\rangle\langle L_3| \frac{1}{\Delta - \tilde{H} + i\Gamma} \tag{B.7}$$

Here, $\tilde{H} = H_0 + V_c \sum_{i,\sigma,\sigma'} n^d_{i,\sigma} n^p_{i,\sigma}$ is Hamiltonian with the excited core hole in the valence band.

Resonance condition and the UCL approximation: In the limit of incident energy resonant with the L_3-edge, $\Delta \to 0$, the propagator in above expression can be written in terms of a series expansion as

$$\begin{aligned} \sum_{n} \frac{|n\rangle\langle n|}{\Delta - E_n + i\Gamma} &= \frac{1}{\Delta - \tilde{H} + i\Gamma} \\ &= \frac{1}{\Delta + i\Gamma} \sum_{l=0}^{\infty} \left(\frac{\tilde{H}}{\Delta + i\Gamma} \right)^l \end{aligned} \tag{B.8}$$

The first term in the Green function expansion contributes for the elastic scattering ($\sigma = \sigma'$) and dominant NSC ($\sigma \neq \sigma'$) part of spectra. The above series is convergent only in the limit $\frac{\tilde{H}}{\Delta + i\Gamma} < 1$.

One can see that it is always convergent in the off-resonance condition as $E_n < \Delta + i\Gamma \ \forall \ n$ as has been discussed in [134]. One can evaluate RIXS intensity using the first few terms of the expansion. Also, the overall intensity goes down as one moves away from resonance.

It gets trickier in the case of the resonance condition. It is important to remember that the intermediate Hamiltonian has a finite bandwidth (W_n). If the $W_n < \Gamma$, the expression is convergent.

As explained App. A of [113], all the terms that act on site-i vanishes since the vector $D_i|g\rangle$ has annihilation operator projects out all the particles on this site. Therefore, only the term $(\tilde{H} - \tilde{H}_i)D_{i,\sigma}|g\rangle = (H_0 - H_i)D_{i,\sigma}|g\rangle$ survives. It is also important to note that the terms $H - H_i$ also commute with operator D_i and hence one can reorganize the operators as

$$\begin{aligned}\sum_{l=0}^{\infty} \frac{\tilde{H}^l}{(i\Gamma)^{l+1}} D_i|g\rangle &= \sum_{l=0}^{\infty} D_i \frac{(H-H_i)^l}{(i\Gamma)^{l+1}}|g\rangle \\ &= D_i\left(\frac{1}{i\Gamma} + \frac{H_i}{(i\Gamma)^2} + ...\right)|g\rangle\end{aligned} \tag{B.9}$$

Now, one can see that the RIXS cross-section can be written in terms of correlation functions as the terms H_i can be written as a generic operator in real space. For practical reasons, we restrict our expansion to second order. The first term in the expansion can be written as,

$$\langle f|D^{\dagger}_{i,\sigma'}|L_3\rangle\langle L_3|D_{i,\sigma}\ 1|g\rangle = \begin{cases} \langle f|\sum_i e^{i\mathbf{q}\cdot\mathbf{R}_i} n_{i,\sigma}|g\rangle & \text{if } \sigma' = \sigma, \\ \langle f|\sum_i e^{i\mathbf{q}\cdot\mathbf{R}_i} S_{i,\sigma}|g\rangle & \text{if } \sigma' \neq \bar{\sigma}. \end{cases} \tag{B.10}$$

Here, the n_i $(= \sum_{i,\sigma} d^{\dagger}_{i,\sigma} d_{i,\sigma})$ conserves the spin and S_i $(= \sum_{i,\sigma} d^{\dagger}_{i,\bar{\sigma}} d_{i,\sigma})$ flips spin on the local site-i.

To the second order, RIXS cross-sections for the $\Delta S = 0$ channel can be written as

$$\begin{aligned}\mathcal{I}^{UCL}_{\pi-\pi}(\mathbf{q},\omega) = |W_{\pi-\pi}|^2 \Big\{ &\frac{1}{\Gamma^2}\sum_f \Big|\langle f|\sum_i e^{i\mathbf{q}\cdot\mathbf{R}_i} n_{i,\sigma}|g\rangle\Big|^2 \\ &+ \frac{J^2}{4\Gamma^4}\sum_f \Big|\langle f|\sum_i e^{i\mathbf{q}\cdot\mathbf{R}_i}\mathbf{S}_i\cdot(\mathbf{S}_{i+1}+\mathbf{S}_{i-1})|g\rangle\Big|^2 \\ &+ O\Big(\frac{J^4}{\Gamma^6}\Big)\Big\}\delta(\Omega + E_g - E_f).\end{aligned} \tag{B.11}$$

Simlarly for the $\Delta S = 1$ channels, the RIXS cross-section can be written as

$$\begin{aligned}\mathcal{I}^{UCL}_{\pi-\sigma}(\mathbf{q},\omega) = |W_{\pi-\sigma}|^2 \Big\{ &\frac{1}{\Gamma^2}\sum_f \Big|\langle f|\sum_i e^{i\mathbf{q}\cdot\mathbf{R}_i} S^z_i|g\rangle\Big|^2 \\ &+ \frac{J^2}{4\Gamma^4}\sum_f \Big|\langle f|\sum_i e^{i\mathbf{q}\cdot\mathbf{R}_i} S^z_i\mathbf{S}_i\cdot(\mathbf{S}_{i+1}+\mathbf{S}_{i-1})|g\rangle\Big|^2 \\ &+ O\Big(\frac{J^4}{\Gamma^6}\Big)\Big\}\delta(\Omega + E_g - E_f).\end{aligned} \tag{B.12}$$

These derived effective correlation function can be an important tool to understand the RIXS correlation as has been used in Chapter 5.

Vita

Umesh Kumar was born in Uttar Pradesh, India, to parents Moolchandra Rajput and Sharda Devi. As an undergraduate student, he attended the Indian Institute of Technology Delhi (IITD) from 2009 to 2013, where he earned a Bachelors of Technology in Engineering Physics. After graduation, Umesh joined the Doctoral program at the University of Tennessee in Knoxville, Tennessee. In graduate school, Umesh worked as a Graduate Research Assistant for Prof. Steven Johnston. During this time, he focused on developing theory of resonant inelastic x-ray scattering (RIXS) spectroscopy, which can be used for understanding oxygen K-edge and Cu L-edge RIXS spectra of one-dimensional cuprates using numerical methods. His work contributed towards establishing RIXS as an important tool for revealing the signatures of spin and charge fractionalization in strongly correlated materials. The results of his graduate research led to a total of four publications, and four APS march meeting presentations. He defended his Ph.D. in July 2019, and is scheduled to move to Los Alamos National Laboratory in Fall 2019 to continue his scientific career as Postdoctoral Research Associate.